

CZECH TECHNICAL UNIVERSITY IN PRAGUE

Faculty of Nuclear Sciences and Physical Engineering
Department of Nuclear Chemistry

DISSERTATION

Synthesis of scintillating metamaterials based on
cesium lead halide nanoparticles

Prague 2022

Ing. Kateřina Děcká

Bibliografický záznam

Autorka	Ing. Kateřina Děcká České vysoké učení technické v Praze, Fakulta jaderná a fyzikálně inženýrská, Katedra jaderné chemie
Název práce	Příprava scintilačních metamateriálů s využitím nanočástic cesno-olovnatých halogenidů
Studijní program	Aplikace přírodních věd
Studijní obor	Jaderná chemie
Školitel	doc. Ing. Václav Čuba, Ph.D. České vysoké učení technické v Praze, Fakulta jaderná a fyzikálně inženýrská, Katedra jaderné chemie
Školitelka specialista	doc. RNDr. Eva Mihóková, CSc. Fyzikální ústav Akademie věd České republiky, Oddělení optických materiálů
Akademický rok	2021/2022
Počet stran	116
Klíčová slova	Nanokrystaly, kvantové omezení, luminiscence, CsPbBr ₃ , polystyren, tenké vrstvy, metamateriály, scintilační detektory, rychlé časování

Bibliographic Entry

Author	Ing. Kateřina Děcká Czech Technical University in Prague, Faculty of Nuclear Sciences and Physical Engineering, Department of Nuclear Chemistry
Title of Dissertation	Synthesis of scintillating metamaterials based on cesium lead halide nanoparticles
Degree Program	Applications of natural sciences
Field of Study	Nuclear Chemistry
Supervisor	doc. Ing. Václav Čuba, Ph.D. Czech Technical University in Prague, Faculty of Nuclear Sciences and Physical Engineering, Department of Nuclear Chemistry
Supervisor Specialist	doc. RNDr. Eva Mihóková, CSc. Institute of Physics of the Czech Academy of Sciences, department of Optical Materials
Academic Year	2021/2022
Number of Pages	116
Keywords	Nanocrystals, quantum confinement, luminescence, CsPbBr ₃ , polystyrene, thin films, metamaterials, scintillation detectors, fast timing

Abstrakt

Cílem této dizertační práce byla syntéza a charakterizace nanokrystalů cesno-olovnatých perovskitů (CsPbBr_3) a zkoumání jejich možné aplikace jako detektorů s vysokým časovým rozlišením v pozitronové emisní tomografii a počítačové tomografii s detekcí doby průletu fotonů. V rámci dosažení tohoto cíle jsem na naší katedře nejdříve zavedla dvě metody syntézy nanokrystalů CsPbBr_3 . Poté jsem porovnávala výsledky těchto dvou metod a zjistila jsem, že pro zamýšlené aplikace je vhodnější metoda *hot injection*. Vzorky jsem charakterizovala s ohledem na jejich strukturální a morfologické vlastnosti (rentgenová difrakce, elektronová mikroskopie), optické vlastnosti (absorpční/transmisní spektroskopie) a luminiscenční vlastnosti (foto- a radioluminiscenční spektra a dosvity) se silným důrazem na radioluminiscenci a časové charakteristiky.

Ve druhé řadě byly s ohledem na zamýšlené aplikace připravovány a důkladně charakterizovány tenké vrstvy na scintilačních i nescintilačních substrátech. Pro budoucí využití v detektorech s vysokým časovým rozlišením byla identifikována nejlepší kombinace nanokrystalů CsPbBr_3 a objemového scintilátoru. Za účelem překonání zjištěných nedostatků jsem navrhla a vyzkoušela zabudovat CsPbBr_3 do polystyrenové matrice, tyto vzorky jsem následně charakterizovala a ověřila tak tento koncept nanokompozitu. Všechny připravené kompozity (tenké vrstvy i nanokrystal zabudované v polystyrenové matici) jsem charakterizovala jako scintilační detektory se zaměřením na jejich časové rozlišení při buzení jak měkkým rentgenovým zářením, tak gama fotony o energii 511 keV.

Z předkládané práce vyplynul tento koncept možného budoucího detektoru s vysokým časovým rozlišením: nanokrystal CsPbBr_3 zabudované v polystyrenové matici prokládané objemovým monokrystalem GGAG:Ce ($\text{Gd}_3\text{Ga}_3\text{Al}_2\text{O}_{12}:\text{Ce}^{3+}$) jako vrstvený, „sendvičový“ detektor. Jeden z načrtnutých možných budoucích výzkumných směrů je optimalizace a další vývoj nanokrystalů CsPbBr_3 v polystyrenové matici; na konci této práce jsem popsala konkrétní návrhy.

Abstract

The focus of this dissertation was to synthesize and characterize lead halide perovskite nanocrystals (CsPbBr_3) and to explore their possible application as fast timing detectors for the time-of-flight positron emission tomography or computed tomography. In order to pursue this goal, I started by establishing two synthesis methods of CsPbBr_3 nanocrystals at our department. Then, the results of those methods were compared, and the hot injection method was identified as the better suited for the proposed applications. The sample characterization spanned from the structural and morphological (X-ray diffraction, electron microscopy) to optical (absorption/transmission spectroscopy) and luminescent properties (photo- and radioluminescence spectra and decays), with strong accent on radioluminescence and timing.

Secondly, to pursue the applications, thin films on both scintillating and non-scintillating wafers were produced and thoroughly characterized as well. The best combination of CsPbBr_3 nanocrystals and bulk scintillator was assessed for possible use in future ultrafast detectors. To overcome some identified drawbacks, the nanocomposite with CsPbBr_3 embedded in polystyrene matrix was proposed, synthesized and characterized as a proof-of-concept. All the prepared composites (thin films and nanocrystals embedded in polystyrene) were characterized as scintillation detectors with special regard to their time resolution, both under soft X-ray and 511 keV gamma irradiation.

The presented work proposed the following concept for the prospective future detector in fast timing applications: CsPbBr_3 nanocrystals embedded in the polystyrene matrix interleaved with the bulk GGAG:Ce ($\text{Gd}_3\text{Ga}_3\text{Al}_2\text{O}_{12}:\text{Ce}^{3+}$) single crystal, as a layered “sandwich” detector. One of the outlined possible future research directions was the optimization and further development of CsPbBr_3 nanocrystals in the polystyrene matrix nanocomposites; ideas to pursue were described in detail at the end of this dissertation.

Poděkování

Ráda bych na tomto místě v první řadě poděkovala svým školitelům Václavovi Čubovi (KJCH FJFI) a Evě Mihókové (FZU) za odborné vedení a podporu v průběhu celého doktorátu. Evě bych zvlášť poděkovala za její velké nasazení a ochotu kdykoliv rychle a důkladně zodpovědět mé dotazy. Hodně jsem se toho od ní naučila a těším se na další spolupráci. Děkuji také Martinovi Niklovi (FZU) za toto výzkumné téma, za podporu při jeho zpracovávání a za vždy přínosné postřehy a diskuse.

Dále si veliké díky za příjemné pracovní prostředí a všestrannou podporu (vědeckou i psychickou) zaslouží pracovníci skupiny radiační chemie na KJCH FJFI, především Jan Bárta, Lenka Prouzová Procházková a Xenie Popovič.

Zvláštní poděkování chci také věnovat svým studentům Adéle Suché a Janu Králi. Dosáhli pod mým vedením velmi zajímavých a důležitých výsledků a díky nim jsem mohla upravit úhel pohledu na svoji práci. Diskuse s Janem byly obzvlášť obohacující, těším se na další společný výzkum.

Tato práce by ovšem nikdy nevznikla bez zázemí mé rodiny. Děkuji tedy hlavně svým rodičům za jejich nekonečnou podporu a ochotu se mnou prožívat úspěchy i neúspěchy. Toto břemeno pak statečně převzal můj manžel, a to zrovna v době, kdy jsem pocítovala více těch neúspěchů; o to větší uznání mu náleží. Díky i za to, že se všichni nepřestávají zajímat o to, čím se zabývám, hodně to pro mě znamená.

Acknowledgement

Let me also thank to my collaborators and friends abroad. My biggest thanks go to Etienne Auffray for the opportunity to work with her group. Every visit in her lab at CERN was a pleasure and a huge boost to my research. I have met amazing people there who have been a great inspiration to me. The first one was Rosana; I have learnt a lot about physics from her and she quickly became my dear friend. I thank her and also Stefan, Nicolaus and Fiammetta, among others. I hope we will continue to collaborate in the future and that our friendship will flourish regardless.

Another big thank goes to Benoit Mahler. During my stay in his lab at Lyon university, he taught me the hot injection technique, which was a major breakthrough in my research. He also helped me by advice to set up the Schlenk line in our lab. I am not exaggerating by saying that it is thanks to him that I was able to finish my dissertation on time.

Glossary & list of abbreviations

BGO	bismuth germanate ($\text{Bi}_4\text{Ge}_3\text{O}_{12}$)
CERN	European Council for Nuclear Research (<i>Conseil Européen pour la Recherche Nucléaire</i>)
CT	computed tomography
CTR	coincidence time resolution
DDAB	didodecyldimethylammonium bromide
DMF	<i>N,N</i> -dimethylformamide
DTR	detector time resolution
ES	excited state
FNSPE	Faculty of Nuclear Sciences and Physical Engineering
FWHM	full width at half maximum
FZU	Institute of Physics of the Czech Academy of Science
GGAG	gadolinium gallium aluminium garnet ($\text{Gd}_3\text{Ga}_3\text{Al}_2\text{O}_{12}$)
GS	ground state
HI	hot injection
HOMO	highest occupied molecular orbital
IR	infrared
IRF	instrumental response function
KJCH	Department of Nuclear Chemistry (<i>Katedra jaderné chemie</i>)
LSO	lutetium oxyorthosilicate (Lu_2SiO_5)
LUMO	lowest unoccupied molecular orbital
LYSO	lutetium-yttrium oxyorthosilicate ($\text{Lu}_x\text{Y}_{2-x}\text{SiO}_5$)
OA	oleic acid
OAm	oleylamine
PET	positron emission tomography
PL	photoluminescence
PS	polystyrene
R&D	research and development
RL	radioluminescence
RTP	room temperature precipitation
SEM	scanning electron microscopy
TEM	transmission electron microscopy
TOF	time of flight
UV	ultraviolet
VIS	visible
XRPD	X-ray powder diffraction

Table of Content

1	PREFACE.....	17
2	INTRODUCTION.....	19
2.1	LUMINESCENT MATERIALS.....	19
2.1.1	<i>Extrinsic luminescent centers.....</i>	20
2.1.2	<i>Intrinsic luminescence.....</i>	21
2.1.3	<i>Semiconductor quantum dots.....</i>	23
2.1.4	<i>Composite materials.....</i>	24
2.2	ENERGY SHARING AND ENERGY TRANSFER PROCESSES.....	25
2.2.1	<i>Energy transfer processes.....</i>	25
2.2.2	<i>Energy sharing concept for scintillating metamaterials.....</i>	26
2.3	CESIUM LEAD HALIDE NANOCRYSTALS.....	28
2.3.1	<i>Structure and luminescent properties.....</i>	28
2.3.2	<i>Synthesis methods.....</i>	30
2.3.3	<i>Composite materials involving CsPbBr₃.....</i>	32
3	LIST OF COMMENTED PUBLICATIONS.....	33
4	RESULTS AND DISCUSSION.....	35
4.1	SYNTHESIS AND CHARACTERIZATION OF FREE NANOCRYSTALS.....	35
4.2	THIN FILMS ON SCINTILLATING WAFERS.....	38
4.3	POLYSTYRENE MATRIX.....	45
5	CONCLUSIONS AND OUTLOOKS.....	49
	REFERENCES.....	53

1 Preface

History of scintillation materials begun with the discovery of X-rays at the end of 19th century. Since then, the area of their possible applications has been growing steadily and is no more limited to simple scintillation screens and detectors of X-rays. Even today, scintillators with specifically tailored properties are being extensively studied and successfully implemented in various fields, including medicine.

This dissertation is focused on their synthesis and prospective application as detectors with ultra-fast response. Call for such detectors has arisen in the field of high energy physics, where the increasing rate of particle collisions and subsequent increasing number of events needed to be detected create an urgent demand for them. In addition, fast detectors are also sought-after in medical imaging techniques. By including a precise timing information (time of flight, TOF) to conventional techniques, such as PET (positron emission tomography), or CT (computed tomography), their resolution can increase considerably by increasing signal-to-noise ratio. Moreover, by shortening the exposure of a patient to ionizing radiation, significant reduction of applied radiation doses is expected.

Such a challenging feat can be accomplished by a scintillating metamaterial, i. e. material suitably combining properties of its individual scintillating components. As will be discussed in the Introduction chapter, the state-of-the art scintillators have either sufficient stopping power and energy resolution, or ultrafast scintillation response. The key to success can be a smart combination of both in one detector.

The Introduction chapter of this dissertation deals with basic principles of luminescence processes and properties of scintillating materials and how they change in scintillating nanoparticles with quantum confinement effect. Then, the intended design of scintillating metamaterial for ultrafast detectors is introduced, followed by a brief review of cesium lead halide nanocrystals as prospective material for such detectors.

The experimental part is written as a compendium of my publications in journals with high impact factors. Some of my unpublished work is included there as well.

The concluding chapter is dedicated, except for the conclusions of the thesis, to future outlooks and challenges in this topic, opening the path to future investigation. The most prospective research direction, resulting from my presented work, is outlined.

This work was supported by the Ministry of Education, Youth and Sports (project CAAS, CZ.02.1.01/0.0/0.0/16_019/0000778), Czech Science Foundation (grants GA17-06479S, GA20-06374S) and Grant Agency of the Czech Technical University in Prague (grants SGS17/195/OHK4/3T/14, SGS20/185/OHK4/3T/14).

Some parts of this dissertation were tackled by students under my supervision; Adéla Suchá (research project and master thesis) and Jan Král (bachelor thesis, research project, and master thesis) were working on thin films of CsPbBr₃ nanocrystals on scintillating wafers; A. Suchá using the precipitation technique for CsPbBr₃ synthesis, J. Král using the hot injection technique.

Most of the characterization was done by me and my students, when the experimental setup was available in our department (i. e. absorption, transmission, and photoluminescence spectra, and X-ray powder diffraction). Radioluminescence spectra were always measured by me at the Institute of Physics of the Czech Academy of Science (FZU).

In cases the experimental setups were not at our disposal, the measurements were provided by our collaborators. In this place, I would like to give my thanks to Ing. Ivo Jakubec, CSc. with the Institute of Inorganic Chemistry of the Czech Academy of Sciences for transmission electron microscopy, Ing. František Hájek for scanning electron microscopy, Dr. Vladimír Babin and doc. Ing. Petr Průša, Ph.D. for scintillation decays. F. Hájek and V. Babin are with the FZU, F. Hájek is also with the Faculty of Nuclear Sciences and Physical Engineering (FNSPE). P. Průša is with the FNSPE and also with the FZU.

Scintillation decays were also measured together with the time resolution in CERN (Conseil Européen pour la Recherche Nucléaire) in the frame of Crystal Clear Collaboration, which brings together international experts on R&D on scintillation materials and detectors (including readout electronics and data acquisition) for particle physics and medical imaging. For those measurements and help with their interpretation, I thank to the whole team led by Dr. Etienne Auffray, in particular to Dr. Rosana Martinez Turtos, Dr. Stefan Gundacker, and doctoral students Fiammetta Pagano and Nicolaus Kratochwil.

2 Introduction

This chapter aims to familiarize the reader with basic concepts of physics of scintillating materials and how their luminescence properties change from bulk to nanomaterials. Then, by explaining energy transfer and energy sharing processes, the intended design of a scintillating metamaterial for ultrafast detectors is introduced. In the end of this chapter, cesium lead halide perovskite nanocrystals are presented both as prospective candidates for such scintillating metamaterials and as the core material studied in the presented work.

2.1 Luminescent materials

Luminescence is the emission of ultraviolet (UV), visible (VIS) or infrared (IR) light produced by the material as a result of conversion of other forms of energy, such as: non-ionizing photons, electrons, mechanical, thermal, biological, electrical, or chemical energy. Accordingly, there are various types of luminescence: photoluminescence, cathodoluminescence, triboluminescence, thermoluminescence, bioluminescence, electroluminescence, or chemiluminescence. When the production of photons results from the conversion of ionizing radiation, the process is called scintillation (or radioluminescence, those two terms are usually not strictly distinguished in the literature) and the corresponding material is called a scintillator, usually referring to a sensitive volume of a scintillation detector. Scintillation detector generally consists of a scintillator (i. e. scintillating material) and a photodetector (e. g. photomultiplier tube), which converts the UV/VIS photons emitted by the scintillator to an electrical pulse.

This dissertation deals mostly with the radioluminescence (RL), and also with the photoluminescence (PL). There is a profound difference between these two types of luminescence. In PL, the delivered energy is only enough to excite the specific luminescence center in the material. On the other hand, in RL, large amount of energy is absorbed by the material, and all the luminescence centers are excited simultaneously. The scintillation process is described in detail below, see Figure 1 in subsection 2.1.1.

The application area of luminescent materials (in general called “phosphors”) is as wide as their division. They are used as various markers, measuring samples in analytical chemistry, light collectors in solar cells, light sources in LEDs and displays or various detectors of both

ionizing and non-ionizing radiation. This dissertation focuses on scintillators and their applications as ultrafast detectors in the time-of-flight positron emission tomography (TOF-PET) and time-of-flight computed tomography (TOF-CT).

Every luminescent material has its luminescent centers which are responsible for the energy conversion process. The centers can be either intrinsic or extrinsic. Intrinsic luminescent centers are either based on excitons (bound electron-hole pairs) or simple recombination of free charge carriers in semiconductors. Extrinsic luminescent centers are defects in the crystal lattice, either doped ions or nonintentional crystal defects. This dissertation deals with both types of luminescent centers, but its main focus is put on intrinsic phosphors.

2.1.1 Extrinsic luminescent centers

Extrinsic luminescent centers are usually dopants, i. e. intentionally introduced crystal defects *via* substitution of cations in the structure. Typical doped crystal used as a fast detector in TOF-PET is LSO:Ce ($\text{Lu}_2\text{SiO}_5:\text{Ce}$, lutetium oxyorthosilicate doped with cerium). LSO serves as a matrix for a luminescent dopant Ce^{3+} which substitutes for lutetium. The scintillation mechanism is visualized in Figure 1.

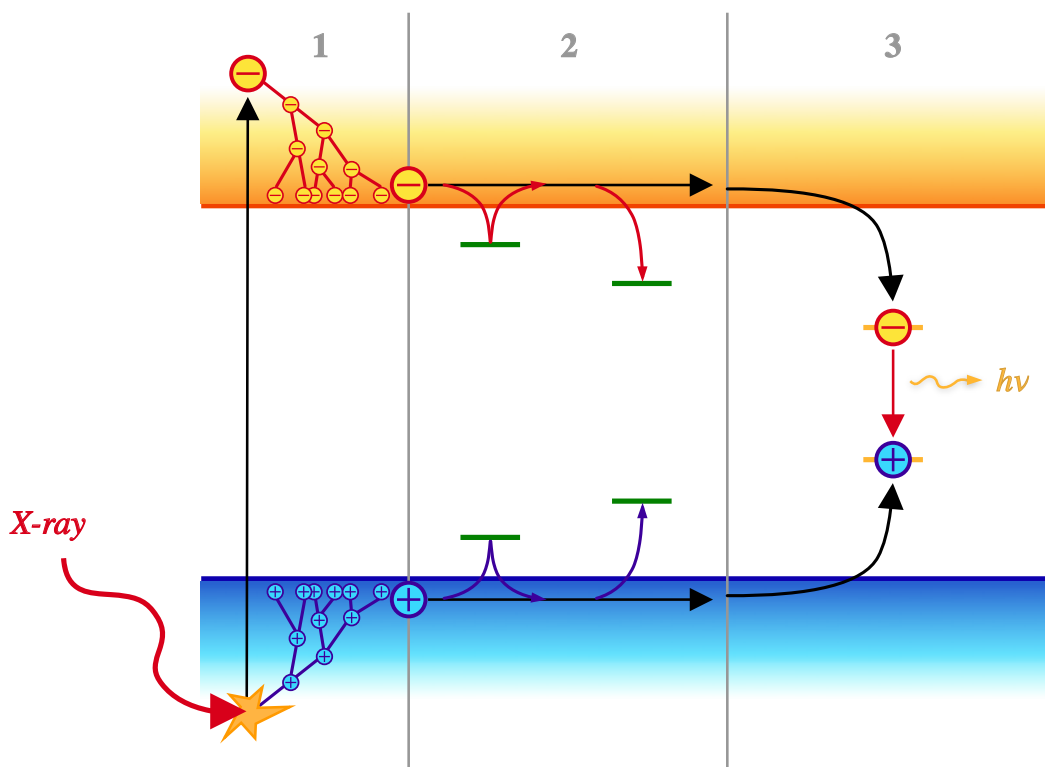


Figure 1 Schematic illustration of a scintillation mechanism. Stage 1: conversion – production of highly excited free charge carriers and their thermalization. Stage 2: transport of free charge carriers, trapping/detrapping processes, risk of losing charge carriers in deep traps. Stage 3: trapping at luminescence center, radiative recombination of electron with hole.

In the first stage, called *conversion*, the ionizing radiation impacts the crystal and starts to attenuate while producing free charge carriers: electrons and holes. Those so-called hot electrons and deep holes thermalize while producing secondary charge carriers. At the end of the first stage, electrons are thermalized at the bottom of the conduction band and holes at the top of the valence band.

The second stage of a scintillation process is *transport*. Free charge carriers migrate through the crystal lattice, electrons in the conduction band and holes in the valence band. This phase is crucial for the light yield and timing properties of a scintillator. Charge carriers can be trapped at discrete energy levels present in the forbidden gap (so-called electron/hole traps). Each trap is characterized by its depth, which is determined as an energy that the charge carrier needs to escape the trap back to the valence/conduction band. If the trap is shallow enough, so that the charge carriers can escape using only thermal energy already present in the crystal (i. e. interaction with phonons), the scintillation process is only delayed accordingly. The detrapping time is directly proportional to the trap depth. If the trap is deep, the charge carrier stays in until an external energy is delivered. This carrier is lost for the scintillation process and therefore the light yield of a scintillator is reduced.

The last stage of a scintillation process is *luminescence*. Charge carriers are trapped at a luminescence center (dopant) and recombine radiatively, i. e. emit photon in the UV/VIS/IR part of optical spectrum according to the energy difference between the ground state and the excited state of the dopant.

2.1.2 *Intrinsic luminescence*

Intrinsic luminescence is either exciton based or caused by radiative recombination of free charge carriers over the band gap. This type of luminescence occurs mostly in semiconductors. Exciton is a coulombically bound electron-hole pair. It is characterized by its binding energy (the amount of energy needed to decompose the exciton) and exciton Bohr radius (the distance between the electron and hole). Exciton with low binding energy and large exciton Bohr radius is called Mott-Wannier or free exciton and has very fast decay time (recombines radiatively very quickly). The second type of exciton is called Frenkel exciton, which has high binding energy and small radius.

Excitons can move freely through the forbidden gap on their energy levels, unless they decompose, or they are captured by a trap. If trapping is caused by local deformations of

the crystal lattice as a result of exciton migrating through the crystal, the exciton is called the self-trapped exciton.

Intrinsic scintillation process, when involving excitons, is very similar to extrinsic process with only two differences. First, charge carriers migrate through the crystal bound together in the form of excitons, and second, radiative recombination occurs either at or near a crystal defect. Energy of emitted photon is usually lower than the semiconductor band gap. This feature is quantified by the so-called Stokes shift, defined as the energy difference between the maxima of absorption and emission spectra.

This energy difference is caused by dissimilar geometry of the ground and the excited states. Absorption leads to higher vibrational state of the excited state, so the first energy loss is caused by a shift of surrounding atoms in a crystal to reach a new equilibrium. The second energy loss occurs after deexcitation that leads to higher vibrational state of the ground state for the same reasons. This process is illustrated by a configuration coordinate diagram in Figure 2.

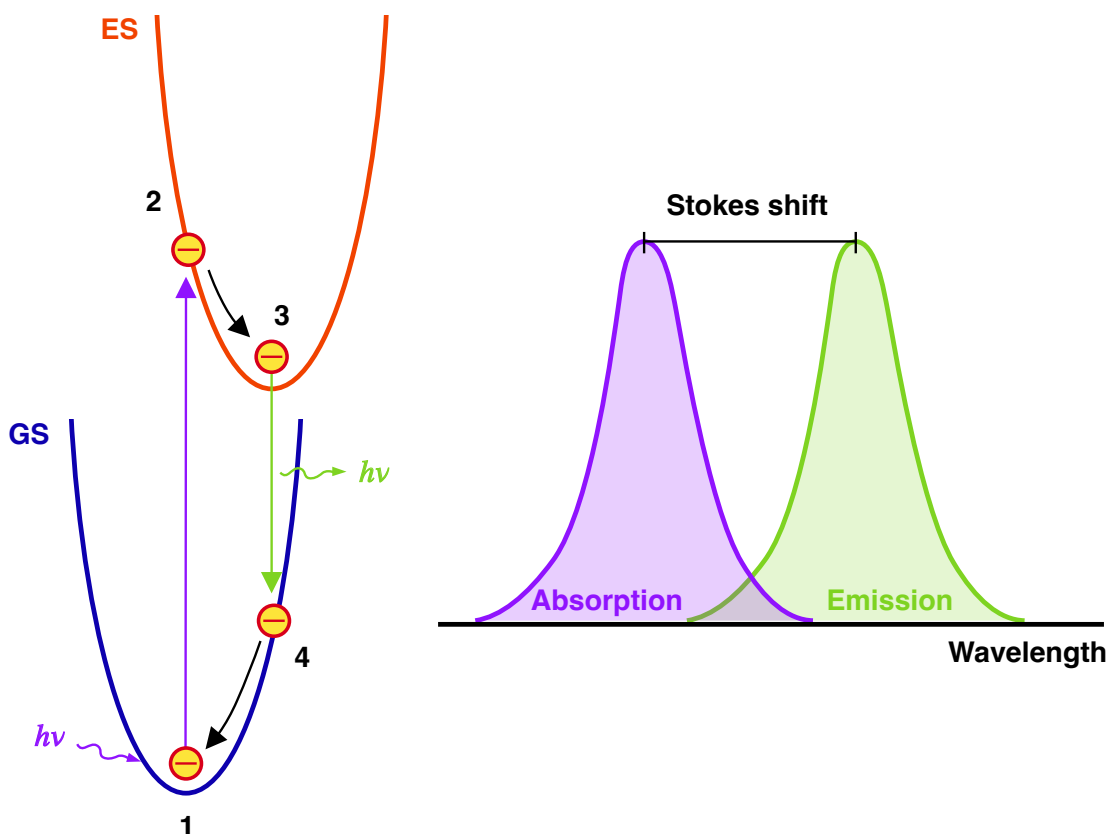


Figure 2 Schematic illustration of the Stokes shift; the y-axis representing energy was omitted for better readability. Left: Configuration coordinate diagram of the excitation–deexcitation process that leads to the Stokes shift. 1 – electron in the ground state (GS) absorbs a UV photon and is excited to a higher vibrational level of the excited state (ES); 2 – electron thermally relaxes to the lowest vibrational state of the ES; 3 – electron radiatively decays to a higher vibrational state of GS; 4 – electron thermally relaxes to the lowest vibrational level of GS. Right: Impact of the Stokes shift on the absorption and emission spectra positions.

2.1.3 Semiconductor quantum dots

Quantum dots represent a special case among the semiconductor luminescent materials. They possess some unique luminescent properties as a direct result of the quantum confinement effect. This effect occurs when any of dimensions of a semiconductor nanocrystal is comparable to or lower than the exciton Bohr radius, therefore excitons are spatially confined in the nanocrystal. This leads to more frequent exciton decays, i. e. faster decay time and higher light yield. Based on the number of “confined” dimensions in a nanocrystal we speak of quantum dots (3D confined, spheres/cubes/pyramids etc.), quantum wires (2D confined, prisms/cylinders/fibers etc.) and quantum wells (1D confined, platelets/sheets/thin films).

This effect also has an impact on the position of absorption and emission spectra. As the dimension of a nanocrystal decreases, its band structure breaks down back to molecule-like individual energy levels. In consequence, the energy of the forbidden gap is no longer dictated by the separation of the valence and the conduction bands, because they no longer exist in quantum dots. It is more proper to define the forbidden gap in such nanomaterials in a molecule-like fashion, i. e. as the energy difference between the highest occupied molecular orbital (HOMO) and the lowest unoccupied molecular orbital (LUMO). The energy separation between those levels further increases as the dimensions of such nanocrystal decrease even more, see Figure 3.

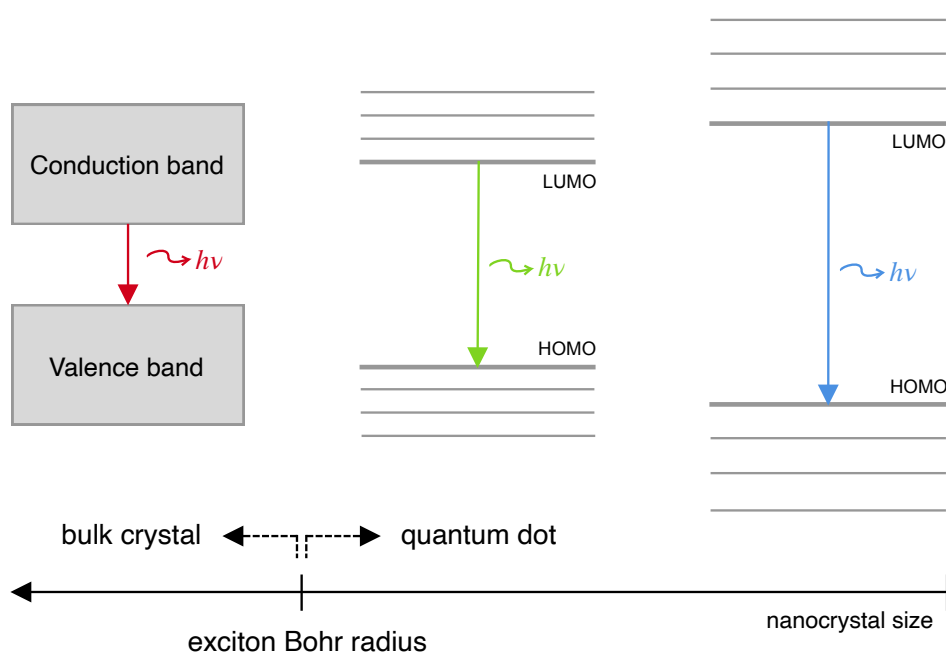


Figure 3 Schematic representation of the quantum confinement effect. As the size of the nanocrystal gradually decreases (from left to right), the energy continuum (within the band) breaks down and the emission spectrum shifts from the red to the green and the blue spectral regions.

This behavior makes quantum dots a material of choice for applications looking for a fast and bright luminescence and/or for emission spectra tunability.

2.1.4 Composite materials

Semiconductor quantum dots (e. g. zinc/cadmium sulphides/selenides, cesium lead halides) are usually prepared in the form of colloidal solution that is not directly usable for most applications. Moreover, these nanocrystals usually cannot be separated in a powder form from the solution without risking serious damage to its luminescent properties and/or its integrity (Bekenstein et al., 2015). It is therefore imperative to fabricate a composite material using those quantum dots.

The most important thing to consider is the choice of the host matrix. The choice mostly depends on the final application, but also on the nature of nanocrystals. This dissertation deals with ultrafast scintillation detectors and air/moisture sensitive nanocrystals, therefore subsequent considerations will be focused on this particular set of problems.

If nanocrystals are sensitive to the ambient conditions, the main purpose of the host matrix will be to protect them from the air, i. e. oxygen and moisture. This can be done either on a single particle level by growing a protective shell around each nanocrystal (this type of a composite is called the core-shell material) or on a macroscopic level by dispersing the nanocrystals in a solid block of a matrix material. However, the matrix can provide much more than simple protection of the nanocrystal. By wise choice of material one can enhance luminescence properties of the encapsulated material by annealing various surface defects (Procházková et al., 2019) and/or by providing an additional volume to interact with the incident radiation and thus enhancing the overall scintillator response by the energy transfer (Burešová et al., 2016) or energy sharing (Turtos, Gundacker, Omelkov, et al., 2019).

This is particularly important for the application of nanocrystals as scintillators, because by themselves, they typically lack the volume to efficiently stop the incident radiation. Moreover, quantum dots usually have a very small Stokes shift which means that in thick enough films to provide sufficient stopping power, a significant amount of the emitted light will be lost due to the self-absorption.

Either way, the protective material must also have specific properties with regards to the future detector. First, the matrix must have high transmittance for the nanocrystal emission wavelength. Depending on the type of incident radiation to detect, the matrix material should be permeable for this as well, or at least it should be able to transport

the absorbed energy to the encapsulated nanocrystal. Considering the latter for the ultrafast scintillation detectors, the energy transport is mostly undesirable because it will slow down the overall scintillating response. Last but not least, if the final application falls in the field of high energy physics, the matrix material also must exhibit sufficiently high radiation hardness.

Matrix that is tested in this dissertation is polystyrene that serve as a monolith. Polystyrene is a scintillator itself which is already used as a detector in combination with various dyes which serve as activators enhancing its response, and wavelength shifters that tune the position of the emission spectrum (J. Zhu et al., 2016). Its radiation hardness is long known to be poor (Britvich et al., 1993), but for the target application in PET/CT it does not pose a significant problem as the radiation doses will not be too high. It protects nanoparticles well (Cai et al., 2018), but for additional protection the dispersed nanocrystals can be coated individually (e. g. by a silica shell).

The biggest challenge is to fabricate a composite with high filling factor of nanocrystals while maintaining its translucence. If the filling factor is too low, the composite is not able to stop the incident radiation and the detector overall efficiency will be too poor, or it may not be able to detect the radiation at all. The highest achieved filling factor of translucent scintillation nanocomposite to date is 60 wt.% (C. Liu et al., 2017).

Silica core-shell composites are easy to fabricate in water environment but challenging in water-free organics with moisture sensitive nanocrystals. Some research groups achieved well protected silica core-shell colloidal nanocrystals (Guan et al., 2020; Shao et al., 2018; Zhong et al., 2018) but such protocols were hard to reproduce. Alternative way is to embed the nanocrystals in a mesoporous silica (H. C. Wang et al., 2016). The resulting material can be easily separated as a scintillating dry powder of well protected nanocrystals, but with questionable applicability as a scintillator in a detection system.

2.2 Energy sharing and energy transfer processes

2.2.1 Energy transfer processes

Energy transfer can occur either radiatively or nonradiatively between donor and acceptor luminescent centers when the condition of spectral overlap between the absorption spectrum of the acceptor and emission spectrum of the donor is fulfilled. When the acceptor center is excited by photons emitted by the donor center, the energy transfer is radiative. On the other

hand, in the nonradiative energy transfer the excitation energy is directly transferred between the two centers.

Nonradiative energy transfer (usually called Förster-Dexter) can occur only if the distance between donor and acceptor is short enough, usually not more than 30 Å, so that the two centers have a nonvanishing interaction with each other (Blasse et al., 1994). This interaction can be either an exchange interaction thanks to the wavelength function overlap, or electric or magnetic multipolar interaction. The energy transfer rate is dependent on the distance between the centers, the type of interaction, and the amount of resonance (the extent of the spectral overlap).

To detect nonradiative energy transfer, careful measurements of excitation spectra and decays are required. First, absorption bands of the donor will be detected in the excitation spectrum of the acceptor. This means that if we excite the donor exclusively (if it is possible for the two centers), the emission of the acceptor will be present in the measured spectrum. If we measure the decay of the donor, it should be shortened, because the nonradiative energy transfer gives another deexcitation path to the excited state of donor, which shortens its effective lifetime. On the other hand, if the decay of the donor center is longer than that of the acceptor, the decay of the acceptor will be prolonged accordingly.

2.2.2 Energy sharing concept for scintillating metamaterials

The R&D in scintillators came to a point where we have very bright scintillators that are unfortunately not fast enough on one hand, and ultrafast scintillators that are not bright enough (under the excitation by ionizing radiation) on the other hand. Currently, the only viable way seems to be to develop a scintillating metamaterial combining the best of both groups. To achieve this, we need to produce as many photons as possible, as fast as possible. This is a direct consequence of the fact that we need to minimize so called coincidence time resolution (CTR) which is in principle the characteristic value representing how fast is a scintillating detector for the TOF-PET application. CTR decreases with increasing light yield and shorter rise and decay times, the target value being 10 ps, because this would significantly improve the spatial resolution of this method and would in consequence reduce the required doses applied to patients (Lecoq et al., 2020). The CTR can be represented by the following formula (Gundacker et al., 2019):

$$\text{CTR} \propto \sqrt{\frac{\tau_r \cdot \tau_d}{n'}}$$

where τ_r and τ_d are scintillation rise and decay times, respectively, and n' is the number of detected photons.

For TOF-CT, the demand on time resolution is not that strict. The key point in this method is to reduce the number of scattered photons, because they cause reduction of the contrast-to-noise ratio of the scan and can also induce artifacts in reconstructed images. To mitigate these effects, higher doses are required to be applied to patients. More than half of the scattered photons can be removed by reducing the time resolution at 100 keV X-ray excitation to 100 ps. At 10 ps, the influence of scattered photons would be almost entirely suppressed. (Rossignol et al., 2020)

Previous subsection implies that any form of energy transfer process between the metamaterial components is undesirable because it inevitably leads to longer decays or possible loss of scintillation light. But how can we develop a scintillating metamaterial when it seems that any communication between the components is forbidden? The answer is energy sharing, see Figure 4.

The metamaterial should be a composite of a bulk scintillating single crystal with high stopping power, high light yield and good energy resolution, and some material having an ultrafast scintillation response that will serve as time tagger.

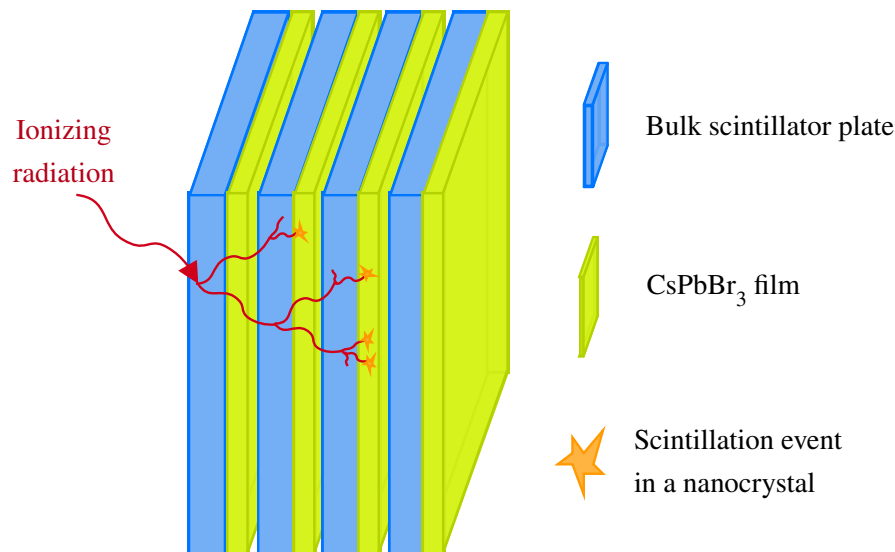


Figure 4 Schematic representation of the energy sharing concept in the model scintillating metamaterial structure (metapixel).

Among the latter, semiconductor quantum dots such as CdSe or CsPbBr₃ were proposed because of their extremely fast rise and decay times thanks to the quantum confinement effect (see subsection 2.1.3). When combined in the scintillating metamaterial, which can have for example the form of alternating layers of the bulk scintillator and quantum dots (see Figure 4), the incident radiation will be attenuated by the single crystal, but secondary charge carriers generated by this interaction can cause scintillation events in the nanocrystalline layer. In this way the energy is shared between the components without any delays or losses caused by the energy transfer.

2.3 Cesium lead halide nanocrystals

Cesium lead halide nanocrystals have been first synthesized and identified by Nikl et al. group as nanoinclusions in the CsX (X = Cl, Br, I) host single crystal doped with Pb²⁺ ions more than twenty years ago (Babin et al., 2001; Nikl et al., 1995, 1999). Even then they demonstrated their superior luminescence properties such as ultrafast (subnanosecond) decay times and narrow emission bands. However, this material came into the spotlight not sooner than in 2015, when the synthesis of colloidal (free-standing) nanocrystals was introduced (Protesescu et al., 2015). Since then, it has been in the center of attention of a large scientific community.

2.3.1 Structure and luminescent properties

Cesium lead halide nanocrystals of the formula CsPbX₃ (X = Cl, Br, or I) possess the perovskite structure consisting of PbX₆⁴⁻ octahedra. When X = Cl or Br, the octahedra are interconnected by vertices and their structure is orthorhombic, a little distorted from the ideal cubic structure, see Figure 5. The structure of CsPbI₃ differ from the other two; in this case PbI₆⁴⁻ octahedra are isolated from each other. Moreover, the local symmetry around Pb²⁺ decreases with increasing atomic number of the halide anion. (Tomanová et al., 2019) This dissertation is focused solely on cesium lead bromide perovskites.

CsPbBr₃ nanocrystals belong to a larger family of materials that are imprecisely called “low-dimensional halide perovskites”, where CsPbX₃ are “3D-perovskites”. The other two materials are Cs₄PbX₆ and Cs₂PbX₅, so-called “0D-“ and “2D-perovskites”, respectively. Between those two, I will introduce only the former, because it was also studied in this dissertation as a parasitic phase that can form during the synthesis of CsPbBr₃ nanocrystals.

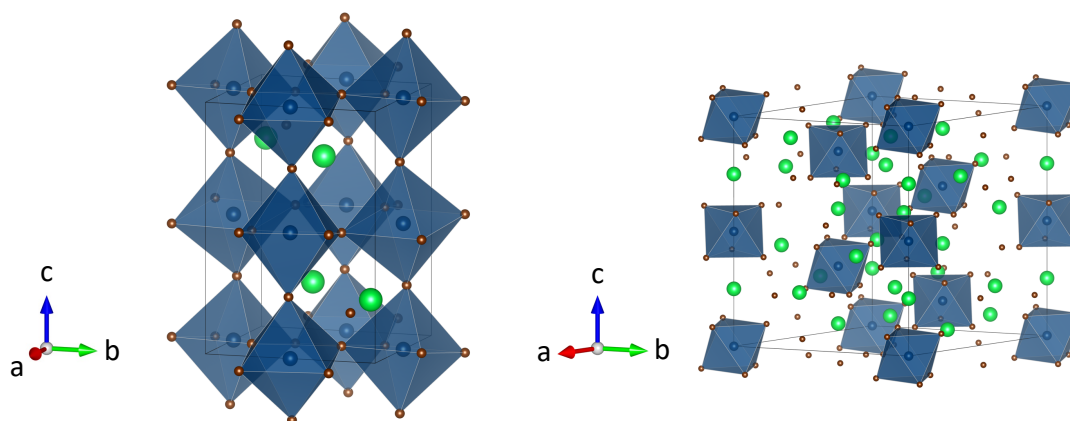


Figure 5 Structure of CsPbBr_3 (left) and Cs_4PbBr_6 (right) drawn with VESTA software (Momma et al., 2011). Green atoms are Cs, blue atoms are Pb, and brown atoms are Br. For better clarity and readability, the Cs-Br bonds were omitted in this drawing and the atom sizes were reduced to a half. This image was adapted from (Děcká, Suchá, et al., 2021).

Cs_4PbBr_6 is still somewhat controversial material. Its structure differs from that of CsPbBr_3 . It also consists of PbBr_6^- octahedra, but they are completely isolated from each other, see Figure 5. This is the reason why they are called “0D-perovskites”.

It was reported that this material possess the same luminescence characteristics as (or even superior to) CsPbBr_3 , namely narrow and bright emission bands in the green spectral region and very fast decay times (Saidaminov et al., 2016; Yuhai Zhang et al., 2017). However, these findings were immediately questioned as those early studies were lacking any attempts to explain the origin of such luminescence in the Cs_4PbBr_6 . In fact, the bandgap of Cs_4PbBr_6 was calculated to be 3.9 eV in contrast to 2.3 eV of CsPbBr_3 (Kang et al., 2018), therefore any excitonic emission in the green spectral region should be ascribed to CsPbBr_3 .

Two main branches of opinions formed: one claiming the luminescence originates in tiny CsPbBr_3 impurities within the Cs_4PbBr_6 crystal (Qin et al., 2019; J. Xu et al., 2017; Q. Xu et al., 2020) and the other attributing it to point defects in the Cs_4PbBr_6 structure (Cha et al., 2020; L. Yang et al., 2019; Yin et al., 2018). The debate seems to continue despite the fact that general consensus seems to be shifted towards the CsPbBr_3 impurity theory (Cao et al., 2021; Yang Li et al., 2022; Riesen et al., 2019). I contributed to this debate with (Děcká, Suchá, et al., 2021), defending the impurity theory.

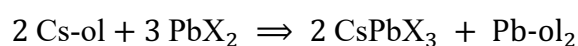
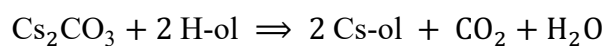
Due to their excellent luminescence properties, CsPbX_3 nanocrystals became instantly identified as highly promising for a number of applications, such as solar cells (Kulbak et al., 2016; Maning Liu et al., 2020; Swarnkar et al., 2016; R. Wang et al., 2019; J. Zhang et al., 2019), photodetectors (Asuo et al., 2019; Ying Li et al., 2017; Ramasamy et al., 2016),

LEDs (Mondal et al., 2019; Quan et al., 2018; J. Song et al., 2015; Y. H. Song et al., 2016), displays (B. Liu et al., 2020; Ming Liu et al., 2017; Swarnkar et al., 2015), and lasers (Evans et al., 2018; Y. Xu et al., 2016; Yakunin et al., 2015). Recently, a body of studies on the lead halide perovskites have also been focused on their application in scintillation detectors, see recent review papers (Moseley et al., 2021; Sarkar, 2021; L. J. Xu et al., 2020; H. Yang et al., 2021).

2.3.2 Synthesis methods

The most widely used method to synthesize colloidal CsPbBr₃ is the hot injection (see Figure 6), which was also the first method that was used to synthesize CsPbX₃ nanocrystals in 2015 (Protesescu et al., 2015). Its popularity is ensured by good reproducibility thanks to the allowed level of control of the reaction conditions. Nanocrystals are synthesized in two steps: first, cesium oleate precursor is synthesized from Cs₂CO₃ and oleic acid (OA) in 1-octadecene, and then the nanocrystals are produced by the injection of the cesium oleate solution into PbBr₂ solution in 1-octadecene, oleic acid and oleylamine (OAm) at high temperature (150 – 200 °C, depending on the desired size of nanocrystals). All the above-mentioned reactions are carried out under an inert atmosphere and all the liquids are degassed beforehand.

The formation of the cesium oleate and the nanocrystals can be described by following reactions: (Yangning Zhang et al., 2020)



The suffix -ol represents the deprotonated form of the oleic acid, CH₃(CH₂)₇CH=CH(CH₂)₇COO⁻.

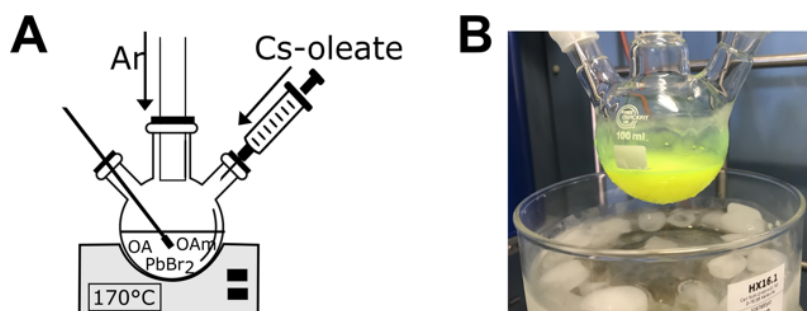
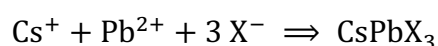


Figure 6 A: Schematic representation of the hot injection process as published in (Děcká, Král, et al., 2021), B: photograph of the as-synthesized CsPbBr₃ nanocrystals after cooling in the ice-water bath. Image taken from (Vaněček et al., 2022).

Usually, the cesium oleate precipitates from the 1-octadecene solution at room temperature because of its polarity. This results in the need of pre-heating the solution at ~ 100 °C prior to the injection. However, it was demonstrated that by adjusting the molar ratio between the oleic acid and Cs^+ to 5 : 1 prior to the synthesis of cesium oleate, the resulting cesium oleate remains in solution even at the room temperature thanks to the formation of reverse micelles composed of Cs^+ ion surrounded by the oleate molecules (Lu et al., 2019). This allowed for better reproducibility of the CsPbBr_3 synthesis.

Another popular technique, probably thanks to its potential for easy scale-up, is so-called room-temperature precipitation method (RTP), or ligand-assisted reprecipitation technique (usually abbreviated as LARP) as it was called by the time it was introduced with the CsPbX_3 predecessor, hybrid organic-inorganic perovskites (F. Zhang et al., 2015). This method was adapted to CsPbX_3 nanocrystals shortly after their introduction using the hot injection method (X. Li et al., 2016).

The principle is as simple as the name suggests. The precursors (CsBr and PbBr_2) are dissolved in a polar solvent (typically *N,N*-dimethylformamide, DMF) in the presence of organic ligands; oleic acid and oleylamine. This solution is then added to a non-polar solvent (typically toluene) and the CsPbBr_3 nanocrystals precipitate immediately. The reaction can be described as follows: (X. Li et al., 2016)



The process is shown schematically with photographs in Figure 7.

To at least mention other methods of CsPbX_3 nanocrystals synthesis, the ultrasonic irradiation (Jang et al., 2016; Rao et al., 2019; Yu Tong et al., 2016), adaptation of classical

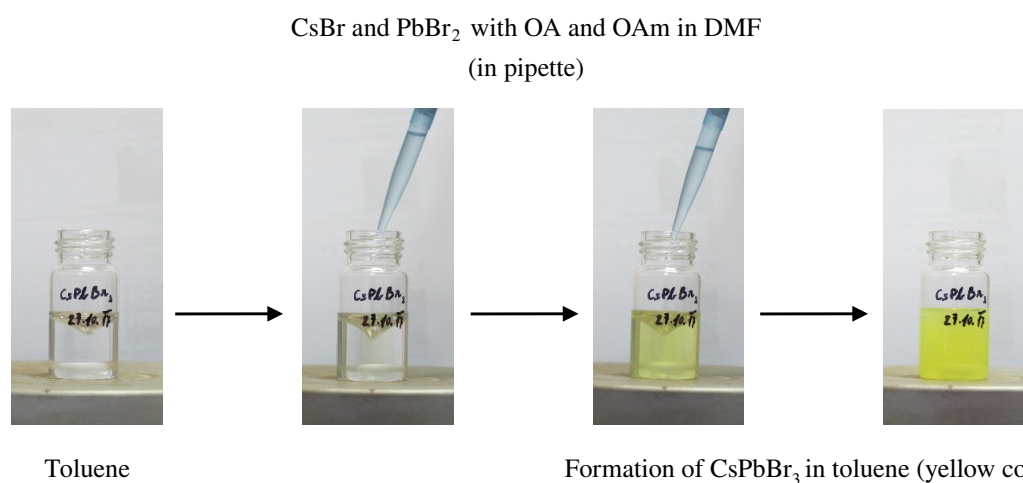


Figure 7 Process of the RTP synthesis. Solution of precursors in *N,N*-dimethylformamide (DMF) is added to toluene. Yellow CsPbBr_3 nanocrystals precipitate immediately.

heat-up method (X. Chen et al., 2016; Tsiwah et al., 2017; Ye et al., 2018), or solvothermal synthesis (D. Chen et al., 2018; M. Chen et al., 2017) have been used.

2.3.3 Composite materials involving CsPbBr₃

As indicated earlier in the subsection 2.1.4, lead halide perovskites are sensitive to air moisture and oxygen (Z. Zhu et al., 2018). Some review papers were published recently on various matrices with successfully incorporated perovskite nanocrystals (Grandhi et al., 2021; Liang et al., 2021); here, I will focus on those intended for applications as scintillation detectors.

Undoubtedly, the most stable matrix (among those currently studied) with respect to both the air and radiation damage is the glass. Several groups recently managed to produce the glass with incorporated CsPbBr₃ nanocrystals (Ma et al., 2021; Niu et al., 2021; Su et al., 2022; Yao Tong et al., 2021; C. Wang et al., 2020; H. Zhang et al., 2021), demonstrating its huge application potential. In principle, they precipitate quantum dots by annealing a precursor glass enriched with CsPbBr₃ precursors.

However, it has been demonstrated that polymer matrices are also applicable in this field if the radiation doses are not expected to be too high (Gandini et al., 2020). TOF-PET with the need to detect 511 keV photons can be considered as such, as was discussed in subsection 2.1.4 as well, not to mention TOF-CT with energies typically between 20–120 keV.

The simplest way to imbed CsPbBr₃ into a polymer matrix is to dissolve the polymer in a suitable solvent (typically toluene or chloroform), mix it with the perovskite colloidal solution and then let the solvent evaporate (Gandini et al., 2020). This was the method of choice in presented work.

Another approach is to mix the colloidal solution with a monomer and polymerize it together (Chhangani et al., 2021). This approach seems to produce nanocomposites with better transparency if handled properly, e. g. with suitable surface ligands instead of classical combination of oleic acid and oleylamine (Nie et al., 2021).

3 List of commented publications

Following publications were chosen as the basis of this dissertation. I am the first author of all of them. Please note that my maiden surname was Tomanová.

- P1 Tomanová, Kateřina**, Václav Čuba, Mikhail G. Brik, Eva Mihóková, Rosana Martinez Turtos, Paul Lecoq, Etienne Auffray, and Martin Nikl. 2019. „On the Structure, Synthesis, and Characterization of Ultrafast Blue-Emitting CsPbBr₃ Nanoplatelets.” *APL Materials* 7 (1): 011104. <https://doi.org/10.1063/1.5079300>.
- P2 Tomanová, Kateřina**, Adela Suchá, Eva Mihóková, Lenka Procházková, Ivo Jakubec, Rosana M. Turtos, Stefan Gundacker, Etienne Auffray, and Václav Čuba. 2020. “CsPbBr₃ Thin Films on LYSO:Ce Substrates.” *IEEE Transactions on Nuclear Science* 67 (6): 933–38. <https://doi.org/10.1109/TNS.2020.2978581>.
- P3 Děcká, Kateřina**, Adéla Suchá, Jan Král, Ivo Jakubec, Martin Nikl, Vítězslav Jarý, Vladimír Babin, Eva Mihóková, and Václav Čuba. 2021. “On the Role of Cs₄PbBr₆ Phase in the Luminescence Performance of Bright CsPbBr₃ Nanocrystals.” *Nanomaterials* 11 (8): 1935. <https://doi.org/10.3390/nano11081935>.
- P4 Děcká, Kateřina**, Jan Král, František Hájek, Petr Průša, Vladimír Babin, Eva Mihóková, and Václav Čuba. 2021. “Scintillation Response Enhancement in Nanocrystalline Lead Halide Perovskite Thin Films on Scintillating Wafers.” *Nanomaterials* 12 (1): 14. <https://doi.org/10.3390/nano12010014>.
- P5 Děcká, Kateřina**, Fiammetta Pagano, Isabel Frank, Nicolaus Kratochwil, Eva Mihóková, Etienne Auffray, and Václav Čuba. “Timing performance of lead halide perovskite nanoscintillators embedded in polystyrene matrix.” *Journal of Materials Chemistry C*, in press. <https://doi.org/10.1039/d2tc02060b>.

4 Results and Discussion

This chapter is divided in three sections, each concerning two of commented publications. The first deals with the synthesis and basic research of produced free nanocrystals (**P1** and **P3**). It also describes the influence of the parasitic Cs_4PbBr_6 phase. The second is focused on application of CsPbBr_3 nanocrystals as thin films on scintillating wafers (**P2** and **P4**). It explains in detail which material combination resulted as the best for the intended scintillation metapixel and what challenges remain unsolved. The last one is describing the embedding of CsPbBr_3 nanocrystals in polystyrene matrix (**P1** and **P5**), paving the way towards possible solutions to the unraveled limitations.

4.1 Synthesis and characterization of free nanocrystals

I have been using two methods for synthesis of CsPbBr_3 nanocrystals, the room temperature precipitation (RTP) and the hot injection (HI). The RTP was used to synthesize nanocrystals in **P1** and **P2**, the HI in **P4** and **P5**. Publication **P3** compares the results of both methods.

Both methods were briefly described in the Introduction chapter (subsection 2.3.2; detailed protocols can be found in the corresponding articles). Both have their advantages and limitations. The RTP method is the cheapest option allowing for easy scale-up, which is the most important feature for industrial application. However, it is quite challenging to control and the resulting nanocrystals tend to coexist with the Cs_4PbBr_6 phase, as we have demonstrated in **P3**. The HI method allows for precise control of reaction conditions, but it is more expensive (the need for heating and inert atmosphere protection) and non-scalable.

In Figure 8, the luminescence characteristics of CsPbBr_3 nanocrystals are presented. Their excitonic emission is bright and narrow, positioned at ~ 515 nm, which is shifted from the bulk emission by ~ 15 nm (Nitsch et al., 1996; Sebastian et al., 2015). This means that such nanocrystals are only in a weak quantum confinement regime. Indeed, the mean size of nanocrystals was determined to be ~ 14 nm, which is close to the CsPbBr_3 Bohr radius (~ 4 – 7 nm) (Protesescu et al., 2015; Tomanová et al., 2019), but not below. Nevertheless, as demonstrated in Figure 8b and in the following text, it is sufficient for reaching subnanosecond decay times.

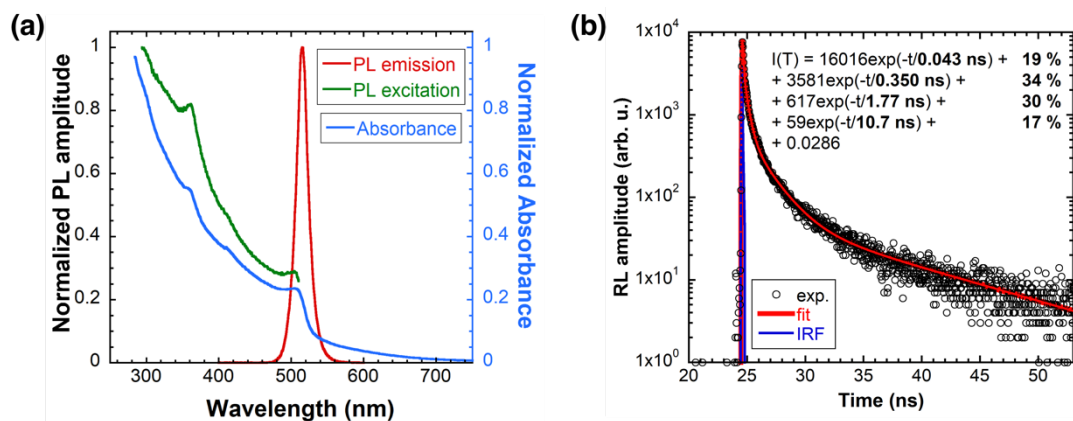


Figure 8 (a) PL emission (red line) and excitation (green line) spectra of free CsPbBr₃ nanocrystals together with absorption spectrum (blue line); (b) scintillation decay of a thin film of CsPbBr₃ nanocrystals on glass wafer (3 μm thick layer); the red line is 4-exponential fit, the blue line is the instrumental response function (IRF) and black circles are the measured data. Nanocrystals have been synthesized by the HI method. Images taken from **P4**.

The previously mentioned small Stokes shift is present, so significant self-absorption issues can be expected in thicker layers and in nanocomposite materials. The absorption spectrum copies the excitation spectrum, which means that the nanocrystals are phase pure. The presented scintillation decay features ultrafast sub-nanosecond decay components (determined as ~ 40 ps and ~ 350 ps), together representing 53 % of all emitted light. These results indicate that CsPbBr₃ nanocrystals are indeed promising candidates for fast-timing detectors.

It should be noted that the best fit was purely mathematical (without an adequate physical interpretation) to describe the data as closely as possible in order to allow observing and comparing any trends in ultrafast components, which is of our main interest. In consequence, the ~ 40 ps component is below the resolution of the used experimental setup (its instrumental response function, IRF, is about 76 ps), and therefore not determined properly. Later on, in **P5**, we started to describe this semi-prompt component using the Dirac-delta function and only state its weight, see for example Table 2 in **P5**.

For the comparison to the results obtained by using the RTP method yielding the parasitic Cs₄PbBr₆ phase, see Figure 9. We demonstrated in **P3** that the RL intensity significantly drops down when Cs₄PbBr₆ crystals are present in the sample (see Figure 3 in **P3**). The reason can be understood from the absorption and excitation spectra (Figure 9b). The Cs₄PbBr₆ phase absorbs at 310 nm, which results in a significant drop in the excitation spectrum of CsPbBr₃ nanocrystals in the same spectral region. Unfortunately, no energy transfer was observed from Cs₄PbBr₆ crystals to CsPbBr₃ nanocrystals, therefore all the incident energy absorbed by the Cs₄PbBr₆ phase is quenched.

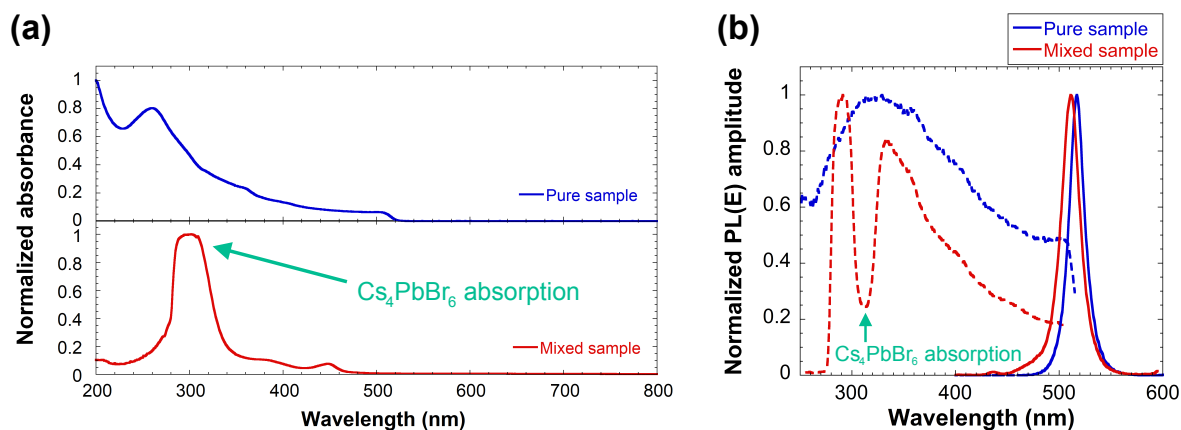


Figure 9 (a) Absorption spectra of pure CsPbBr₃ phase (blue line) and mixed CsPbBr₃ + Cs₄PbBr₆ sample (red line), (b) PL emission (solid lines) and excitation (dashed lines) spectra of pure (blue lines) and mixed (red lines) sample. Images adapted from **P3**.

By simple modification of the RTP method, CsPbBr₃ nanoplatelets can be prepared as demonstrated in **P1**. Their thicknesses were between 1.2 – 2.2 nm, resulting in blue emission (425 nm) due to the strong quantum confinement effect. In PL decay, 46 % of light was emitted within the first nanosecond; the scintillation decay was not measured.

The time resolved PL spectra under laser excitation and detected using the streak camera (the method with much higher precision than the standard setup using the time correlated single photon counting technique) revealed that the smallest nanocrystals emitting at 425 nm are the fastest, emitting with the decay time of 320 ps, see Figure 10. This is a direct consequence of the strong quantum confinement effect. Please note that in this case, the fit was not performed to accurately reproduce the fastest component to avoid the above-mentioned discrepancies, but the discussed semi-prompt component is clearly present.

Nevertheless, as Suchá demonstrated (Suchá, 2020), those nanoplatelets are synthesized with too low yield and concentration to be applicable in further experiments. Moreover, since the ultrafast decay components are present also in the nanocrystals in weaker quantum confinement regime, the modified synthesis was abandoned and Suchá adopted the original method with a few improvements to enable better reproducibility and higher yield of CsPbBr₃ nanocrystals in cubic shape but resulting in mixed samples with Cs₄PbBr₆ crystals.

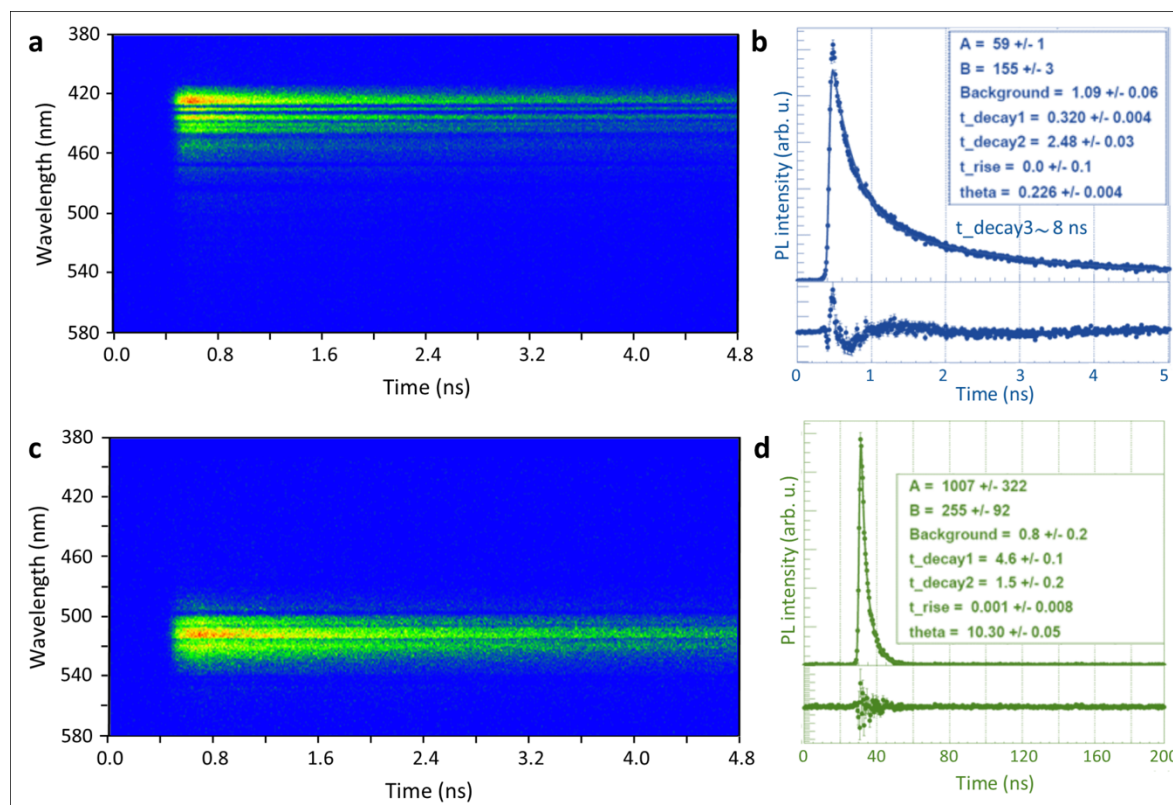


Figure 10 Time resolved PL spectrum of the blue emission from the colloidal sample with maximum at 425 nm (a) and its decay curve (b) and time resolved PL spectrum of the green emission with maximum at 512 nm (c) and its decay curve (d). Excited by laser (372 nm). Image taken from **P1**.

4.2 Thin films on scintillating wafers

Thin films of CsPbBr₃ nanocrystals have been fabricated on various scintillating wafers; namely: LYSO:Ce (**P2**), LYSO:Pr, BGO, and GGAG:Ce (**P4**). The details on the procedure can be found in the corresponding articles (**P2** for the RTP method, **P4** for the HI method). In brief, the selected procedure was the repeated spin-coating technique. To achieve the thickness of 3 μm , 40–50 layers must have been casted. More details on the spin-coating technique can be found also in works of my students; research projects (Král, 2021; Suchá, 2019) and master theses (Král, 2022; Suchá, 2020).

Thin films have been studied as the basic element of the intended metamaterial (the sandwich metapixel as described in subsection 2.2.2). The synergic effect (i. e. the overall contribution is greater than the simple sum of the individual components) of the combination of the chosen bulk scintillator and the nanocrystals must be observed also on this single element before combining them into a much more complicated metapixel.

The listed bulk scintillators were chosen for their high stopping power and good energy resolution. BGO is an established and standard scintillator that has been used in the non-TOF-PET scanners since 1980s (Conti, 2009). Its scintillation light is quite slow (~ 300 ns decay) and not very bright (4,000 – 5,000 ph/MeV), but it was sufficient at the time; its detection efficiency was superior to previously used halide-based crystals with lower density and more importantly, lower light yield (e. g. BaF₂). LYSO:Ce crystal is the representative of the next generation of crystals with faster scintillation decay (~ 40 ns) and much higher light yield ($\sim 40,000$ ph/MeV). It is the first crystal that has been used in conventional TOF-PET scanners with the time resolution of ~ 600 ps (Surti et al., 2007). Currently, the highest achieved time resolution in the laboratory conditions is ~ 100 ps for LSO:Ce,Ca crystals of “clinically relevant” sizes; meaning $2 \times 2 \times 20$ mm³ crystal elements (Gundacker et al., 2019; Lee et al., 2021).

LYSO:Pr was chosen as an alternative to the LYSO:Ce crystal. The Pr³⁺ dopant has the emission spectrum shifted towards shorter wavelengths and faster decay with respect to the Ce³⁺ dopant. Lastly, the chosen GGAG:Ce crystal is a modern scintillator with the emission spectrum overlapping with that of CsPbBr₃. It has been developed as an alternative to the L(Y)SO:Ce crystals; it has superior light yield ($\sim 60,000$ ph/MeV) at the sacrifice of slower decay (~ 170 ns) (Kamada et al., 2014). The slow rise and decay times can be improved by Mg co-doping at the expense of slightly lower light yield (Lucchini et al., 2016). The RL emission spectra of all mentioned scintillators are presented in Figure 11.

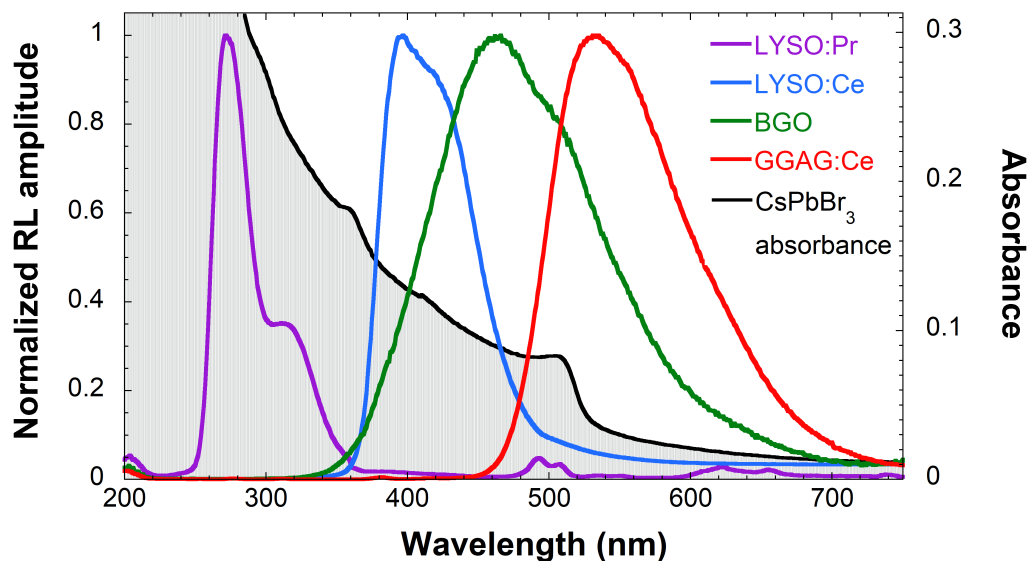


Figure 11 RL emission spectra comparison of bulk scintillators used as wafers for CsPbBr₃ thin films preparation: LYSO:Pr (purple line), LYSO:Ce (blue line), BGO (green line), and GGAG:Ce (red line). The spectra are overlapped with the CsPbBr₃ absorption spectrum (black line).

The first, preliminary study of the thin film of CsPbBr₃ on LYSO:Ce is presented in **P2**. Please, note that the spin-coating process has not yet been adopted for the preparation of thin films on scintillating wafers in this study; the film on LYSO:Ce was prepared by drop-casting of 3 μ l of concentrated suspension on 3 \times 3 \times 0.2 mm³ LYSO:Ce wafer).

Figure 6 in this publication (**P2**) presents RL spectra of CsPbBr₃ on LYSO:Ce and pure CsPbBr₃. The overall intensity of the LYSO:Ce composite is quite poor, as evidenced by the dynamic range of the time measurement in the Figure 7b of that article, despite the excellent light yield of the LYSO:Ce crystal. Moreover, it was observed that LYSO:Ce luminescence was being quenched (most probably by reabsorption within the CsPbBr₃ layer, which was also contaminated by the Cs₄PbBr₆ phase), and this quenching was unfortunately not sufficiently balanced by the enhanced CsPbBr₃ emission. However, the sub-nanosecond components of CsPbBr₃ were preserved in the LYSO:Ce composite despite all the limitations, so the application potential of the CsPbBr₃ layer on scintillating wafers was demonstrated even in those pilot experiments. The outlook of this study (**P2**) was expected improvement of both the quality and scintillation yield of the thin films.

The improvements were achieved when the HI method was adopted and when the spin-coating technique was optimized for those samples. The HI method, yielding pure CsPbBr₃ nanocrystals, improved the scintillation yield as demonstrated in **P3**, and the optimized spin-coating technique improved the quality of films, as demonstrated in the research project (Král, 2021). Then, the new set of composites was fabricated, see Figure 12 (LYSO:Pr, LYSO:Ce and BGO, unpublished results (Král, 2021, 2022)) and **P4** (GGAG:Ce).

However, despite the improvements, the overall intensity of LYSO:Ce and LYSO:Pr composites remained poor, as evidenced by the comparison with pure crystals in Figure 12. Looking at Figure 11, the emission of LYSO:Pr and LYSO:Ce is overlapping with

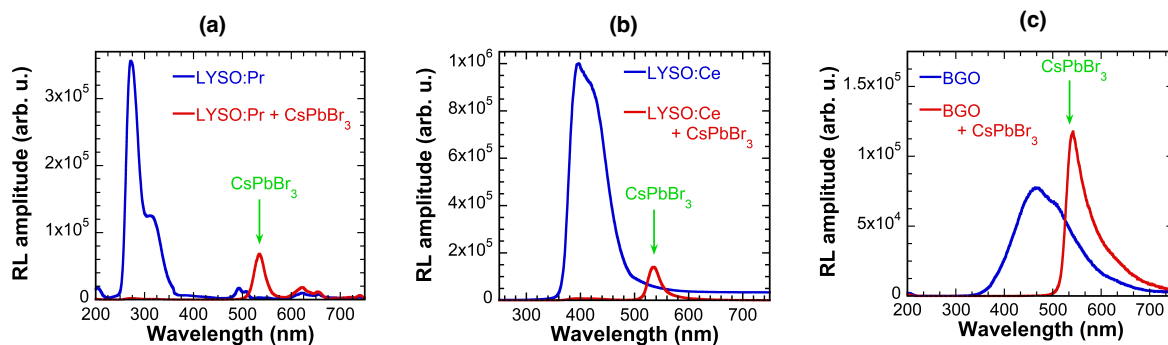


Figure 12 Comparison of RL spectra of pure scintillating wafer (blue line), namely: (a) LYSO:Pr, (b) LYSO:Ce, and (c) BGO, and CsPbBr₃ thin film on the corresponding scintillating wafer (red line). The emission maximum position of pure CsPbBr₃ thin film is indicated by the green arrow. Unpublished data.

the absorption of CsPbBr₃ nanocrystals completely, resulting in severe reabsorption of their emission within the CsPbBr₃ layer. This leads to a conclusion that the overlap between the absorption spectrum of CsPbBr₃ and emission spectrum of the bulk scintillator is highly undesirable and should be minimized while designing the scintillating metamaterial for fast-timing applications. Indeed, when the spectral overlap is lower (as in the case of the BGO emission, cf. Figure 11), the luminescence properties of the composite begin to improve rapidly (cf. Figure 12c). Moreover, when it is only small, the synergic effect of the RL intensity enhancement takes place, as demonstrated in **P4** and Figure 13 in this dissertation (the GGAG:Ce composite).

As presented in Figure 13b (taken from **P4**), the RL intensity enhancement of GGAG:Ce takes place even in the short time window. The reason for this enhancement is that the layer is cracked due to the high strain in such thick film, and the cracks serve as a light guide for the GGAG:Ce emission, cf. Figure 5 in **P4**. Moreover, thanks to the CsPbBr₃ layer in the composite, significantly higher number of photons is emitted within the first nanosecond. This increases the photon density at initial times, which is the main contribution to the time resolution (Gundacker et al., 2020).

In conclusion of this part, the GGAG:Ce, or a bulk scintillator with similar properties and more importantly, similar position of its emission spectrum (or even shifted to longer wavelengths) are the resulting proposed materials of choice for the metamaterial with CsPbBr₃ nanocrystals. To test other bulk scintillators, another kind of nanocrystals must be chosen, or the CsPbBr₃ nanocrystals must be engineered to better suit their emission spectra, i. e. their absorption must be shifted to shorter wavelengths. There are two options how to

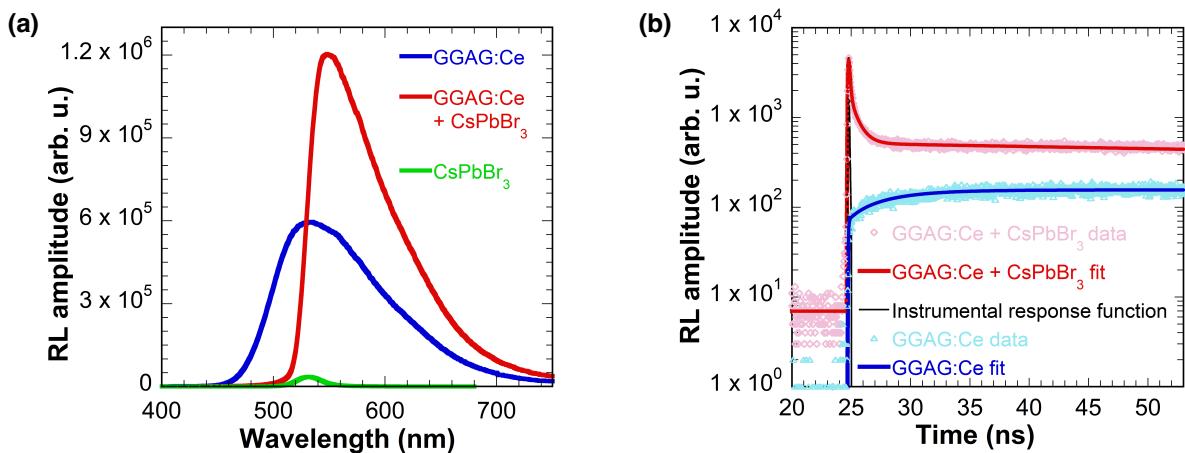


Figure 13 (a) Comparison of the pure GGAG:Ce wafer (blue line), pure CsPbBr₃ thin film (green line) and CsPbBr₃ thin film on GGAG:Ce wafer (red line), (b) comparison of the scintillation decay of pure GGAG:Ce wafer (blue line representing 2-exponential fit with rise time) and CsPbBr₃ thin film on GGAG:Ce (red line representing 3-exponential fit with rise time). Images adapted from P4.

achieve this; the easiest being to reduce the particle size (benefitting from the quantum confinement effect) or to introduce Cl^- to the structure (e. g. by anion exchange reactions) (Akkerman et al., 2015).

The combination of GGAG:Ce and CsPbBr_3 was tested in CERN by Fiammetta Pagano for the time resolution under 511 keV excitation, i. e. CTR (coincidence time resolution, see subsection 2.2.2). Those results were not yet published, see Figure 14.

The concept of CTR is described in (Gundacker et al., 2019). In principle, the ^{22}Na positron source is placed between the reference LSO:Ce,Ca (CTR = 61 ps) scintillator and the measured sample. The 511 keV γ -photons emitted from the source are measured in coincidence; for each event, the energy signal, and the time signal (the arrival time of the photons in the corresponding crystal) are digitized by an oscilloscope. To derive the CTR, only the events from the photopeak in the energy spectrum are selected and the time delay histogram (calculated time delays between the reference and measured sample for each of the selected event) is constructed. The CTR value is extracted as the full width at half maximum (FWHM) of the time delay histogram.

In Figure 14, the energy spectra of measured samples are presented. In the panel (a), thin films of CsPbBr_3 on GGAG:Ce $6 \times 6 \times 0.2 \text{ mm}^3$ wafers are presented together with the pure wafer. Two methods of film fabrication were tested: the drop casting and spin-coating. By spin-coating, thin and high-quality film can be casted (fairly homogeneous, $3 \mu\text{m}$ thick). On the other hand, by drop-casting, much more material can be deposited on the wafer ($30\text{--}50 \mu\text{m}$ thick layer, but very inhomogeneous).

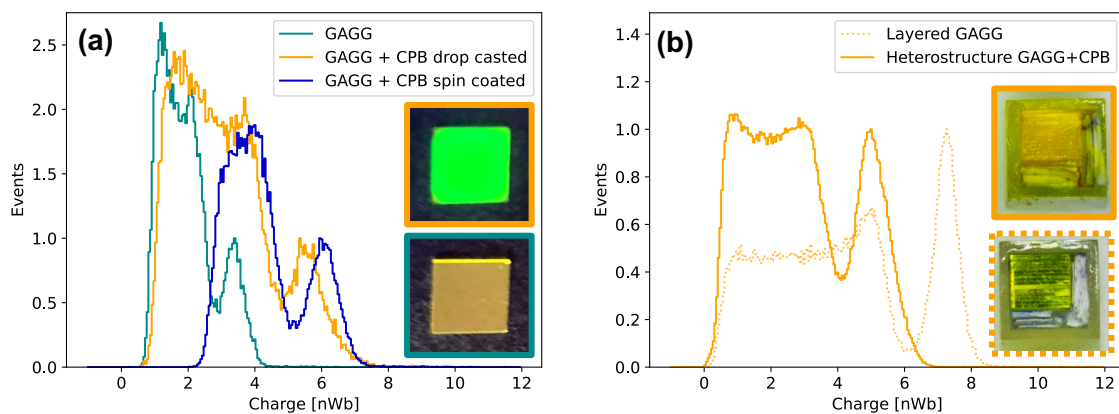


Figure 14 (a) Energy spectra of thin films of CsPbBr_3 on GGAG:Ce,Mg scintillating wafers fabricated by two methods (drop-casted, yellow line, and spin-coated, blue line) compared to the pure GGAG:Ce,Mg wafer (green line); (b) Energy spectra of 14 GGAG:Ce wafers (dimensions $3 \times 3 \times 0.2 \text{ mm}^3$, denoted as “layered GGAG”, dotted line) and a metamaterial of 14 composites of CsPbBr_3 films on GGAG:Ce,Mg wafers (drop-casted, denoted as “heterostructure GGAG+CPB”, solid line), inset: photographs of the pixels. Unpublished data.

By looking at the position of the photopeaks on the charge axes in Figure 14, we can make a comparison of the light outputs of the measured samples. The higher is the photopeak charge, the more photoelectrons were produced by the 511 keV events and thus the corresponding sample has higher light output. Indeed, when casting a CsPbBr₃ layer on top of the GGAG:Ce wafer, the increase in the light output is clearly achieved for both methods.

Interestingly, the spin-coating process resulted in higher light output than the drop-casting process, despite the fact that the amount of CsPbBr₃ nanocrystals is one order of magnitude lower in this sample. Because this sample was measured in different geometry than the RL spectra and decays in **P4**, the light-guiding effect of the cracks should not apply. The RL spectra and decays were measured in the reflection mode, the CsPbBr₃ layer facing the excitation source and detector, while the CTR was in the transmission mode, i. e. the CsPbBr₃ layer facing the excitation source, but the detector was behind the sample (the side of GGAG:Ce facing it). Therefore, the explanation on the enhancement due to the cracks no longer apply and further investigation is needed. Because the effect is not that pronounced, the first step would be to repeat the whole experiment with a new set of samples to confirm this observation.

In contrast, the CTR value is slightly better for the drop-casted sample, see Table 1. This could have been caused by the larger amount of CsPbBr₃ nanocrystals. More energy is deposited in the CsPbBr₃ layer, emitting more photons within the first nanosecond. It is a direct consequence of the fact that CTR does not only depend on the light output (if that was true, the spin-coated sample should have performed better), but also on the timing.

By both methods, the composite sample performed better than the pure GGAG:Ce, resulting in ~100 ps faster CTR. It is not clear yet, whether this is caused purely by the time stamp of

Table 1 Measured CTR values of the prepared thin films and metamaterial based on GGAG:Ce, in comparison with the pure material.

	Sample	CTR (ps)
Thin films ($6 \times 6 \times 0.2 \text{ mm}^3$)	GGAG:Ce	370
	GGAG:Ce + CsPbBr ₃ spin-coated	285
	GGAG:Ce + CsPbBr ₃ drop-casted	265
Metamaterial (15 plates of $3 \times 3 \times 0.2 \text{ mm}^3$)	GGAG:Ce	240
	GGAG:Ce + CsPbBr ₃	325

the CsPbBr₃ nanocrystals, or by the scattering of GGAG:Ce photons on CsPbBr₃ nanocrystals. Future experiments are already designed to confirm this; first, the same samples with “deactivated” nanocrystals (no longer scintillating after their degradation) will be measured to evaluate the scattering effect and then, the effect of the CsPbBr₃ amount will be tested by measuring the drop-casted samples with different thicknesses (i. e. different amounts of casted CsPbBr₃).

Unfortunately, those encouraging results were not transferred to the assembled metamaterial. We observed the degradation of both light output (Figure 14b) and CTR (Table 1). This is most probably a direct consequence of high reabsorption rate of the CsPbBr₃ emission caused by the small Stokes shift (not observable in thin, < 50 μm films, but significant in 3 mm layer, see Figure 15) and also low transparency of such layer caused by light scattering.

Fortunately, both effects can, in principle, be overcome in future experiments. First, the scattering can be suppressed by the encapsulation of nanocrystals into a polymer matrix as evenly as possible. Indeed, high filling factors (60 wt%) in such matrix while maintaining good transparency have already been achieved in the literature for Cd(Zn)S/ZnS core-shell nanocrystals (C. Liu et al., 2017). Moreover, this matrix will also provide the desired stability, since CsPbBr₃ nanocrystals are air sensitive.

After the embedding, the Stokes shift can be addressed by introducing a wavelength shifter to the polymer matrix. By ensuring the chemical bond between the matrix with the shifters and the nanocrystals (achievable by the selection of surface ligands that can polymerize with the matrix during the encapsulation process), the energy transfer from the nanocrystal to the shifter can occur, provided that the absorption spectrum of the shifter overlaps with the emission spectrum of nanocrystals. This approach was also implemented in the above-mentioned article.

Since the wavelength shifter is usually an organic dye (i. e. a molecule), its decay should also be very fast, and it should not slow down the overall scintillation response too much. This fact could be demonstrated by the success of fast polymer scintillators based solely on a polymer with those organic dyes attached (e. g. the well-known BC422 commercial plastic scintillator with the decay time of ~1.3 ns and CTR = 35 ps, despite its low density, 1.03 g·cm⁻³) (Turtos, Gundacker, Auffray, et al., 2019).

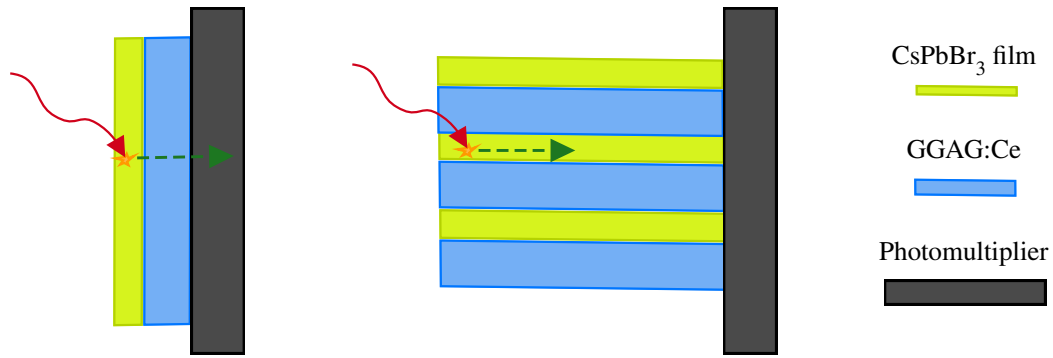


Figure 15 Schematic representation of measurement geometry of single thin film on GGAG:Ce wafer compared to the geometry of the metapixel. Green arrow indicates the CsPbBr₃ emission, which is reabsorbed along its way through thicker layer in the metapixel.

4.3 Polystyrene matrix

As mentioned in the previous section and in the Introduction chapter of this dissertation, the embedding of CsPbBr₃ nanocrystals into a polymer matrix seems to be a viable way to solve various challenges associated with this material, from its instability against air moisture and oxygen, to its applicability as an effective scintillator in a detector system. This is why a preliminary study of such composite was also a part of our first publication on this material (**P1**) and why we explored this concept in more detail in **P5**. However, since the proper embedding is a complex task, the obtained results serve only as a proof-of-concept for future rigorous research of this type of nanocomposites, well beyond the scope of this dissertation.

In Figure 5 of **P1**, we present RL spectra and photographs of CsPbBr₃ nanoplatelets embedded in a polystyrene matrix. The chosen embedding method was simple, dissolving

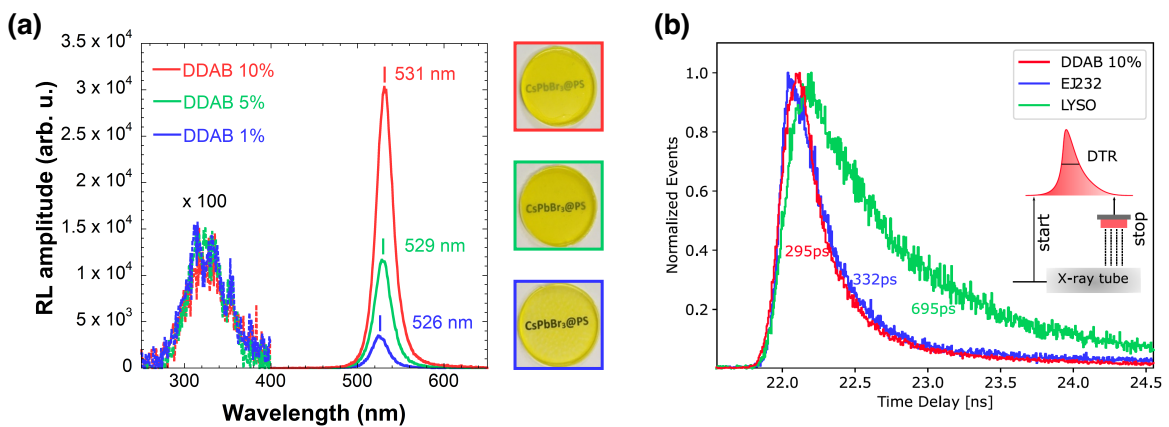


Figure 16 (a) RL spectra of the DDAB set with corresponding photographs; (b) DTR time delay histograms of the DDAB 10% sample (red line) in comparison with EJ232 fast plastic scintillator (blue line) and LYSO:Ce standard scintillator (green line). The inset shows schematically the DTR experimental setup. Images taken from **P5**.

the polystyrene pellets in toluene and mixing the resulting solution with the toluene CsPbBr₃ colloid. Due to the previously discussed fact that the nanoplatelets could have been synthesized only with a small yield, the achieved weight filling factor was only ~0.1 %. However, even with such low loading, we demonstrated that the nanocrystals could migrate within the matrix during its aging, resulting in a green shift of their emission while storing at ambient conditions (daylight, 30 °C), most probably caused by aggregation.

In **P5**, we aimed for significantly larger filling factors (as high as 10 %, i. e. two orders of magnitude higher) while testing two different ligands. The oleic acid + oleylamine (OA + OAm) are standard ligands used in the basic hot injection synthesis of CsPbBr₃ nanocrystals. The DDAB ligand was introduced later (Imran et al., 2018), demonstrating the positive effect on CsPbBr₃ light yield, colloidal, and thermal stability (resulting from weaker solvent-ligand interaction of secondary amines compared to the oleates) shortly after (Imran et al., 2019). This is a result of its better capability of CsPbBr₃ surface passivation, as demonstrated in (L. Zhang et al., 2021). Moreover, as it was shown by Král in his research project (Král, 2021), the DDAB ligand enabled the repeated spin-coating process to achieve higher film thicknesses.

We demonstrated that for both ligands, the RL intensity rises with increasing filling factor, despite the fact that at the same time, the transparency of the samples decreases, see Figure 1 of **P5** or Figure 16a in this dissertation for the RL spectra of the DDAB set. It was also observed that due to its better surface passivation capability, the DDAB ligand enabled the 10 % filling factor, which could not have been achieved by the standard OA+OAm combination, while effectively suppressing the aggregation.

All samples were also tested for their time resolution. Since their geometry (thickness of 100 μm) and low stopping power did not allow for the precise CTR characterization at 511 keV excitation, a novel approach was implemented by the CERN group (Pagano et al., 2022). The excitation source was exchanged for pulsed X-rays (mean energy ~10 keV) and the time delay histogram was constructed as time difference between the start (pulsed laser trigger of the X-ray tube) and the stop signal (the arrival time of the photons in the measured scintillator), see the inset of Figure 16b. Similarly, as for CTR, the FWHM value of this histogram is called DTR, referring to *detector time resolution*.

We found out that irrespective of the filling factor, DTR of all the samples within one set was roughly the same, the DDAB set performing slightly better. For example, DTR of the 10 % OA+OAm sample was (319 ± 9) ps, while the corresponding sample from

the DDAB set had $DTR = (295 \pm 8)$ ps. This value was compared to reference scintillators in similar geometry, as presented in Figure 16b. Compared to the LYSO:Ce DTR, the two-fold better time resolution was achieved, demonstrating the application potential of such nanocomposite for the fast-timing applications. The reason why our sample performed better was most probably due to CsPbBr₃ superior timing characteristics.

The comparison was also made with EJ232 fast plastic scintillator with similar timing properties as the previously mentioned BC422. Since the CsPbBr₃ nanocrystals are even faster than those plastic scintillators, it was expected that the improvement in time resolution would be achieved in this comparison as well. Indeed, almost all of the prepared nanocomposites performed at least slightly better than EJ232 with $DTR = (332 \pm 10)$ ps. However, the improvement was not as significant as expected; this could have been caused by still too low filling factors. As was mentioned at the end of the previous section, future research efforts will be dedicated to maximizing the filling factor while maintaining as good transparency as possible.

5 Conclusions and Outlooks

The first part of my work presented in this dissertation was to implement the synthesis technique of CsPbBr₃ nanocrystals at our department. This goal was clearly achieved; the initial RTP method has proven to be too difficult to control in order to yield significant amounts of pure CsPbBr₃ nanocrystals, therefore the second, more complicated HI method was introduced, yielding the pure CsPbBr₃ phase under well controllable reaction conditions.

It was also demonstrated that the parasitic phase Cs₄PbBr₆ that tend to occur during the RTP synthesis has a negative effect on CsPbBr₃ scintillation properties, which is otherwise bright and ultrafast scintillator suitable for the fast-timing applications as a time tagger in a metamaterial detector. The most important conclusion of this part was that the presence of this phase should be controlled and avoided.

The second part of my work was to produce and characterize scintillating metamaterials for the fast-timing applications. The first step to achieve this goal was to check the compatibility of bulk scintillators with the CsPbBr₃ nanocrystals. This was done by preparation and characterization of CsPbBr₃ thin films on various scintillating wafers as the most basic component of the future metamaterial. Interestingly, it was found that when the nanocrystalline layer is cracked, those cracks can serve as a light guide for the wafer emission, resulting in synergistic effect enhancing the overall scintillation response of such composite.

It was shown that the best candidate for the future metamaterial detector was the GGAG:Ce crystal, because the resulting composite had superior scintillating properties including timing characteristics. Moreover, the CsPbBr₃ thin film improved the CTR value of pure GGAG:Ce,Mg crystals by ~100 ps (from 370 to 265 ps). However, in contrast to those encouraging results, by testing the actual metamaterial assembled of 14 such films, the deterioration of CTR compared to the pure GGAG:Ce,Mg was observed.

The reason why we observed such deterioration was most probably due to the poor light collection of the CsPbBr₃ emission. The nanocrystalline films are not sufficiently transparent in such thicknesses (3 mm in the metapixel); unfortunately, they cannot be in principle. In addition to this, the small Stokes shift (high reabsorption) in nanocrystals have manifested

fully in those samples; since the CsPbBr₃ emitted photons must have travelled through that thick layer of nanocrystals, only insignificant number of them reached the photomultiplier.

In the last part of this dissertation, I demonstrated the transparency and applicability of nanocomposites composed of CsPbBr₃ in a polystyrene matrix for the fast-timing applications. Concentrations as high as 10 wt.% were reached and it was shown that such nanocomposites exhibited time resolutions similar or even slightly better than the state-of-the-art fast plastic scintillator.

In the light of the presented results, I propose the following approach to future efforts in this research area. First, the overlap between the emission spectra of chosen bulk scintillators and CsPbBr₃ absorption must be addressed. In this dissertation, the GGAG:Ce resulted to be the material of choice mostly due to favorable position of its emission spectrum and not because of its superior scintillating properties. To be able to test and compare the performance of various bulk scintillators in future metamaterial fairly, the CsPbBr₃ nanocrystals absorption spectrum needs to be tailored for each tested bulk crystal.

This could be achieved quite easily by reducing the particle size (the quantum confinement effect would shift the absorption to shorter wavelengths and also speed-up the decay), but this could mean sacrificing the stopping power; smaller crystals would have lower density and even less volume to stop the incident radiation. Another approach could be to produce mixed CsPb(Br,Cl)₃ halides, because the chloride anions were demonstrated to shift the absorption spectrum in the same way ([Protesescu et al., 2015](#)). Chlorides are even faster scintillators than bromides, which could compensate the loss in density and probably also the stopping power due to their presence. Most probably, an optimum between the particle size and in particular anion composition can be expected to be found for each desired position of absorption spectra to achieve reasonably high light output.

Next, the Stokes shift presents one of the biggest challenges in applicability of nanocrystalline semiconductors in general across many applications. This could be addressed by linking the nanocrystals to wavelength shifters, i. e. organic molecules with absorption spectra overlapping with nanocrystals emission and with emission spectra at longer wavelengths. Provided they are in close vicinity to the nanocrystals, ideally chemically bonded to them, fast non-radiative energy transfer can occur, effectively shifting their emission. For the fast-timing application, the shifter must be chosen also to have as fast decay as possible itself, not to slow down the overall scintillation response too much.

The easiest way how to incorporate wavelength shifters with nanocrystals is through polymer matrices, where the wavelength shifter usage is already well established to enhance and shift the matrix emission. This concept was already demonstrated also for scintillating nanocrystals while achieving 60 % filling factor with good transparency (C. Liu et al., 2017). This is probably the most promising approach towards the applicability of nanocrystals as time taggers in metamaterials for the fast-timing applications.

References

- Akkerman, Q. A., D’Innocenzo, V., Accornero, S., Scarpellini, A., Petrozza, A., Prato, M., & Manna, L. (2015). Tuning the optical properties of cesium lead halide perovskite nanocrystals by anion exchange reactions. *Journal of the American Chemical Society*, *137*(32), 10276–10281. doi: 10.1021/jacs.5b05602
- Asuo, I. M., Fourmont, P., Ka, I., Gedamu, D., Bouzidi, S., Pignolet, A., Nechache, R., & Cloutier, S. G. (2019). Highly Efficient and Ultrasensitive Large-Area Flexible Photodetector Based on Perovskite Nanowires. *Small*, *15*(1), 1804150. doi: 10.1002/sml.201804150
- Babin, V., Fabeni, P., Nikl, M., Nitsch, K., Pazzi, G. P., & Zazubovich, S. (2001). Luminescent CsPbI₃ and Cs₄PbI₆ Aggregates in Annealed CsI:Pb Crystals. *Physica Status Solidi (B)*, *226*(2), 419–428. doi: 10.1002/1521-3951(200108)226:2<419::AID-PSSB419>3.0.CO;2-C
- Bekenstein, Y., Koscher, B. A., Eaton, S. W., Yang, P., & Alivisatos, A. P. (2015). Highly Luminescent Colloidal Nanoplates of Perovskite Cesium Lead Halide and Their Oriented Assemblies. *Journal of the American Chemical Society*, *137*(51), 16008–16011. doi: 10.1021/jacs.5b11199
- Blasse, G., & Grabmaier, B. C. (1994). Luminescent materials. *Berlin Heidelberg New York: Springer-Verlag*.
- Britvich, G. I., Peresypkin, A. I., Rykalin, V. I., Vasil’chenko, V. G., Korniylovskaya, L. D., Malinovskaya, S. A., Skripkina, V. T., Shershukov, V. M., Yushko, E. G., Kulichenko, A. V., & Pyshchev, A. I. (1993). Radiation damage studies on polystyrene-based scintillators. *Nuclear Inst. and Methods in Physics Research, A*, *326*(3), 483–488. doi: 10.1016/0168-9002(93)90849-D
- Burešová, H., Procházková, L., Turtos, R. M., Jarý, V., Mihóková, E., Beitlerová, A., Pjatkan, R., Gundacker, S., Auffray, E., Lecoq, P., Nikl, M., & Čuba, V. (2016). Preparation and luminescence properties of ZnO:Ga – polystyrene composite scintillator. *Optics Express*, *24*(14), 15289. doi: 10.1364/oe.24.015289
- Cai, Y., Wang, L., Zhou, T., Zheng, P., Li, Y., & Xie, R. J. (2018). Improved stability of CsPbBr₃ perovskite quantum dots achieved by suppressing interligand proton transfer and applying a polystyrene coating. *Nanoscale*, *10*(45), 21441–21450. doi: 10.1039/c8nr06607h
- Cao, F., Yu, D., Xu, X., Han, Z., & Zeng, H. (2021). CsPbBr₃@Cs₄PbBr₆ Emitter-in-Host Composite: Fluorescence Origin and Interphase Energy Transfer. *The Journal of Physical Chemistry C*, *125*(1), 3–19. doi: 10.1021/acs.jpcc.0c08100
- Cha, J. H., Lee, H. J., Kim, S. H., Ko, K. C., Suh, B. J., Han, O. H., & Jung, D. Y. (2020). Superparamagnetism of Green Emissive Cs₄PbBr₆ Zero-Dimensional Perovskite Crystals. *ACS Energy Letters*, *5*(7), 2208–2216. doi: 10.1021/acsenenergylett.0c00964
- Chen, D., Chen, X., Li, J., Li, X., & Zhong, J. (2018). Ultrathin CsPbX₃ (X = Cl, Br, I) nanoplatelets: Solvothermal synthesis and optical spectroscopic properties. *Dalton Transactions*, *47*(29), 9845–9849. doi: 10.1039/c8dt01720d

- Chen, M., Zou, Y., Wu, L., Pan, Q., Yang, D., Hu, H., Tan, Y., Zhong, Q., Xu, Y., Liu, H., Sun, B., & Zhang, Q. (2017). Solvothermal Synthesis of High-Quality All-Inorganic Cesium Lead Halide Perovskite Nanocrystals: From Nanocube to Ultrathin Nanowire. *Advanced Functional Materials*, 27(23). doi: 10.1002/adfm.201701121
- Chen, X., Peng, L., Huang, K., Shi, Z., Xie, R., & Yang, W. (2016). Non-injection gram-scale synthesis of cesium lead halide perovskite quantum dots with controllable size and composition. *Nano Research*, 9(7), 1994–2006. doi: 10.1007/s12274-016-1090-1
- Chhangani, S., Kumar, M., Sahani, R. M., Bera, A., & Pandya, A. (2021). Radiation polymerized CsPbBr₃-PMMA nanocomposite for alpha particle detection. *Materials Today: Proceedings*, 48, 1028-1031. doi: 10.1016/j.matpr.2021.06.432
- Conti, M. (2009). State of the art and challenges of time-of-flight PET. *Physica Medica*, 25(1), 1–11. doi: 10.1016/j.ejmp.2008.10.001
- Děcká, K., Král, J., Hájek, F., Průša, P., Babin, V., Mihóková, E., & Čuba, V. (2021). Scintillation Response Enhancement in Nanocrystalline Lead Halide Perovskite Thin Films on Scintillating Wafers. *Nanomaterials*, 12(1), 14. doi: 10.3390/nano12010014
- Děcká, K., Suchá, A., Král, J., Jakubec, I., Nikl, M., Jarý, V., Babin, V., Mihóková, E., & Čuba, V. (2021). On the Role of Cs₄PbBr₆ Phase in the Luminescence Performance of Bright CsPbBr₃ Nanocrystals. *Nanomaterials*, 11(8), 1935. doi: 10.3390/nano11081935
- Evans, T. J. S., Schlaus, A., Fu, Y., Zhong, X., Atallah, T. L., Spencer, M. S., Brus, L. E., Jin, S., & Zhu, X. Y. (2018). Continuous-Wave Lasing in Cesium Lead Bromide Perovskite Nanowires. *Advanced Optical Materials*, 6(2), 1–7. doi: 10.1002/adom.201700982
- Gandini, M., Villa, I., Beretta, M., Gotti, C., Imran, M., Carulli, F., Fantuzzi, E., Sassi, M., Zaffalon, M., Brofferio, C., Manna, L., Beverina, L., Vedda, A., Fasoli, M., Gironi, L., & Brovelli, S. (2020). Efficient, fast and reabsorption-free perovskite nanocrystal-based sensitized plastic scintillators. *Nature Nanotechnology*, 15(6), 462–468. doi: 10.1038/s41565-020-0683-8
- Grandhi, G. K., Mokurala, K., Han, J. H., Bin Cho, H., Han, J. Y., & Im, W. Bin. (2021). Recent Advances and Challenges in Obtaining Stable CsPbX₃ (X = Cl, Br, and I) Nanocrystals Toward White Light-Emitting Applications. *ECS Journal of Solid State Science and Technology*, 10(10), 106001. doi: 10.1149/2162-8777/ac28e4
- Guan, H., Zhao, S., Wang, H., Yan, D., Wang, M., & Zang, Z. (2020). Room temperature synthesis of stable single silica-coated CsPbBr₃ quantum dots combining tunable red emission of Ag–In–Zn–S for High-CRI white light-emitting diodes. *Nano Energy*, 67(September), 104279. doi: 10.1016/j.nanoen.2019.104279
- Gundacker, S., Martinez Turtos, R., Kratochwil, N., Pots, R. H., Paganoni, M., Lecoq, P., & Auffray, E. (2020). Experimental time resolution limits of modern SiPMs and TOF-PET detectors exploring different scintillators and Cherenkov emission. *Physics in Medicine and Biology*, 65(2). doi: 10.1088/1361-6560/ab63b4
- Gundacker, S., Turtos, R. M., Auffray, E., Paganoni, M., & Lecoq, P. (2019). High-frequency SiPM readout advances measured coincidence time resolution limits in TOF-PET. *Physics in Medicine & Biology*, 64(5), 055012. doi: 10.1088/1361-6560/aafd52
- Imran, M., Ijaz, P., Baranov, D., Goldoni, L., Petralanda, U., Akkerman, Q., Abdelhady, A. L., Prato, M., Bianchini, P., Infante, I., & Manna, L. (2018). Shape-Pure, Nearly

- Monodispersed CsPbBr₃ Nanocubes Prepared Using Secondary Aliphatic Amines [Rapid-communication]. *Nano Letters*, 18(12), 7822–7831. doi: 10.1021/acs.nanolett.8b03598
- Imran, M., Ijaz, P., Goldoni, L., Maggioni, D., Petralanda, U., Prato, M., Almeida, G., Infante, I., & Manna, L. (2019). Simultaneous cationic and anionic ligand exchange for colloidally stable CsPbBr₃ nanocrystals [Rapid-communication]. *ACS Energy Letters*, 4(4), 819–824. doi: 10.1021/acsenerylett.9b00140
- Jang, D. M., Kim, D. H., Park, K., Park, J., Lee, J. W., & Song, J. K. (2016). Ultrasound synthesis of lead halide perovskite nanocrystals. *Journal of Materials Chemistry C*, 4(45), 10625–10629. doi: 10.1039/C6TC04213A
- Kamada, K., Kurosawa, S., Prusa, P., Nikl, M., Kochurikhin, V. V., Endo, T., Tsutumi, K., Sato, H., Yokota, Y., Sugiyama, K., & Yoshikawa, A. (2014). Cz grown 2-in. size Ce:Gd₃(Al,Ga)₅O₁₂ single crystal; Relationship between Al, Ga site occupancy and scintillation properties. *Optical Materials*, 36(12), 1942–1945. doi: 10.1016/j.optmat.2014.04.001
- Kang, B., & Biswas, K. (2018). Exploring Polaronic, Excitonic Structures and Luminescence in Cs₄PbBr₆/CsPbBr₃. *Journal of Physical Chemistry Letters*, 9(4), 830–836. doi: 10.1021/acs.jpcclett.7b03333
- Král, J. (2021). Příprava tenkých vrstev CsPbBr₃ na různých substrátech [výzkumný úkol]. *Czech Technical University in Prague*.
- Král, J. (2022). Příprava a charakterizace scintilačních nanokompozitů na bázi nanokrystalů CsPbBr₃ [Master's thesis]. *Czech Technical University in Prague*.
- Kulbak, M., Gupta, S., Kedem, N., Levine, I., Bendikov, T., Hodes, G., & Cahen, D. (2016). Cesium Enhances Long-Term Stability of Lead Bromide Perovskite-Based Solar Cells. *Journal of Physical Chemistry Letters*, 7(1), 167–172. doi: 10.1021/acs.jpcclett.5b02597
- Lecoq, P., Morel, C., Prior, J. O., Visvikis, D., Gundacker, S., Auffray, E., Križan, P., Turtos, R. M., Thers, D., Charbon, E., Varela, J., de La Taille, C., Rivetti, A., Breton, D., Pratte, J.-F., Nuyts, J., Surti, S., Vandenberghe, S., Marsden, P., ... Benoit, M. (2020). Roadmap toward the 10 ps time-of-flight PET challenge. *Physics in Medicine & Biology*, 65(21), 21RM01. doi: 10.1088/1361-6560/ab9500
- Lee, M. S., Cates, J. W., Gonzalez-Montoro, A., & Levin, C. S. (2021). High-resolution time-of-flight PET detector with 100 ps coincidence time resolution using a side-coupled phoswich configuration. *Physics in Medicine and Biology*, 66(12). doi: 10.1088/1361-6560/ac01b5
- Li, X., Wu, Y., Zhang, S., Cai, B., Gu, Y., Song, J., & Zeng, H. (2016). CsPbX₃ Quantum Dots for Lighting and Displays: Room-Temperature Synthesis, Photoluminescence Superiorities, Underlying Origins and White Light-Emitting Diodes. *Advanced Functional Materials*, 26(15), 2435–2445. doi: 10.1002/adfm.201600109
- Li, Yang, Chen, L., Liu, B., Ruan, J., Liu, J., Ouyang, X., & Xu, Q. (2022). The phosphorescence emission in undoped lead-halide Cs₄PbBr₆ single crystals at low temperature. *Ceramics International*, 48(12), 16730–16736. doi: 10.1016/j.ceramint.2022.02.222
- Li, Ying, Shi, Z. F., Li, S., Lei, L. Z., Ji, H. F., Wu, D., Xu, T. T., Tian, Y. T., & Li, X. J. (2017). High-performance perovskite photodetectors based on solution-processed all-inorganic CsPbBr₃ thin films. *Journal of Materials Chemistry C*, 5(33), 8355–8360.

doi: 10.1039/c7tc02137b

- Liang, S., Zhang, M., Biesold, G. M., Choi, W., He, Y., Li, Z., Shen, D., & Lin, Z. (2021). Recent Advances in Synthesis, Properties, and Applications of Metal Halide Perovskite Nanocrystals/Polymer Nanocomposites. *Advanced Materials*, 33(50), 2005888. doi: 10.1002/adma.202005888
- Liu, B., Li, J., Duan, G., Ji, M., Lu, Y., Yan, T., Cao, B., & Liu, Z. (2020). Study on organic-inorganic hybrid perovskite nanocrystals with regular morphologies and their effect on photoluminescence properties. *Optics Express*, 28(8), 10714. doi: 10.1364/OE.378203
- Liu, C., Li, Z., Hajagos, T. J., Kishpaugh, D., Chen, D. Y., & Pei, Q. (2017). Transparent Ultra-High-Loading Quantum Dot/Polymer Nanocomposite Monolith for Gamma Scintillation. *ACS Nano*, 11(6), 6422–6430. doi: 10.1021/acsnano.7b02923
- Liu, Maning, Pasanen, H., Ali-Löytty, H., Hiltunen, A., Lahtonen, K., Qudsia, S., Smått, J., Valden, M., Tkachenko, N. V., & Vivo, P. (2020). B-Site Co-Alloying with Germanium Improves the Efficiency and Stability of All-Inorganic Tin-Based Perovskite Nanocrystal Solar Cells. *Angewandte Chemie International Edition*, 59(49), 22117–22125. doi: 10.1002/anie.202008724
- Liu, Ming, Zhong, G., Yin, Y., Miao, J., Li, K., Wang, C., Xu, X., Shen, C., & Meng, H. (2017). Aluminum-Doped Cesium Lead Bromide Perovskite Nanocrystals with Stable Blue Photoluminescence Used for Display Backlight. *Advanced Science*, 4(11), 1700335. doi: 10.1002/advs.201700335
- Lu, C., Wright, M. W., Ma, X., Li, H., Itanze, D. S., Carter, J. A., Hewitt, C. A., Donati, G. L., Carroll, D. L., Lundin, P. M., & Geyer, S. M. (2019). Cesium Oleate Precursor Preparation for Lead Halide Perovskite Nanocrystal Synthesis: The Influence of Excess Oleic Acid on Achieving Solubility, Conversion, and Reproducibility. *Chemistry of Materials*, 31(1), 62–67. doi: 10.1021/acs.chemmater.8b04876
- Lucchini, M. T., Babin, V., Bohacek, P., Gundacker, S., Kamada, K., Nikl, M., Petrosyan, A., Yoshikawa, A., & Auffray, E. (2016). Effect of Mg²⁺ ions co-doping on timing performance and radiation tolerance of Cerium doped Gd₃Al₂Ga₃O₁₂ crystals. *Nuclear Instruments and Methods in Physics Research, Section A: Accelerators, Spectrometers, Detectors and Associated Equipment*, 816, 176–183. doi: 10.1016/j.nima.2016.02.004
- Ma, W., Jiang, T., Yang, Z., Zhang, H., Su, Y., Chen, Z., Chen, X., Ma, Y., Zhu, W., Yu, X., Zhu, H., Qiu, J., Liu, X., Xu, X., & Yang, Y. (2021). Highly Resolved and Robust Dynamic X-Ray Imaging Using Perovskite Glass-Ceramic Scintillator with Reduced Light Scattering. *Advanced Science*, 8(15), 1–8. doi: 10.1002/advs.202003728
- Momma, K., & Izumi, F. (2011). VESTA3 for three-dimensional visualization of crystal, volumetric and morphology data. *Journal of Applied Crystallography*, 44(6), 1272–1276. doi: 10.1107/S0021889811038970
- Mondal, N., De, A., & Samanta, A. (2019). Achieving Near-Unity Photoluminescence Efficiency for Blue-Violet-Emitting Perovskite Nanocrystals. *ACS Energy Letters*, 4(1), 32–39. doi: 10.1021/acsenenergylett.8b01909
- Moseley, O. D. I., Doherty, T. A. S., Parmee, R., Anaya, M., & Stranks, S. D. (2021). Halide perovskites scintillators: unique promise and current limitations. *Journal of Materials Chemistry C*, 9(35), 11588–11604. doi: 10.1039/D1TC01595H
- Nie, J., Li, C., Zhou, S., Huang, J., Ouyang, X., & Xu, Q. (2021). High Photoluminescence Quantum Yield Perovskite/Polymer Nanocomposites for High Contrast X-ray Imaging.

- ACS Applied Materials & Interfaces*, 13(45), 54348–54353. doi: 10.1021/acsami.1c15613
- Nikl, M., Nitsch, K., Mihóková, E., Polák, K., Fabeni, P., Pazzi, G. P., Gurioli, M., Santucci, S., Phani, R., Scacco, A., & Somma, F. (1999). Luminescence of CsPbBr₃-like quantum dots in CsBr single crystals. *Physica E: Low-Dimensional Systems and Nanostructures*, 4(4), 323–331. doi: 10.1016/S1386-9477(99)00016-8
- Nikl, M., Nitsch, K., Polak, K., Pazzi, G. P., Fabeni, P., Citrin, D. S., & Gurioli, M. (1995). Optical properties of the Pb²⁺-based aggregated phase in a CsCl host crystal: Quantum-confinement effects. *Physical Review B*, 51(8), 5192–5199. doi: 10.1103/PhysRevB.51.5192
- Nitsch, K., Hamplová, V., Nikl, M., Polák, K., & Rodová, M. (1996). Lead bromide and ternary alkali lead bromide single crystals - Growth and emission properties. *Chemical Physics Letters*, 258(3–4), 518–522. doi: 10.1016/0009-2614(96)00665-3
- Niu, L., Wang, S., Sui, Z., Song, Y., Zhao, L., Liu, L., Ren, J., & Zhang, J. (2021). Highly stable CsPbBr₃ perovskite quantum dot-doped tellurite glass nanocomposite scintillator. *Optics Letters*, 46(14), 3448. doi: 10.1364/ol.430990
- Pagano, F., Kratochwil, N., Salomoni, M., Frank, I., Gundacker, S., Pizzichemi, M., Paganoni, M., & Auffray, E. (2022). A new method to characterize low-stopping power and ultra-fast scintillators using pulsed X-ray. Unpublished work, to be submitted to *Frontiers in Physics*.
- Procházková, L., Vaněček, V., Čuba, V., Pjatkan, R., Martinez-Turtos, R., Jakubec, I., Buryi, M., Omelkov, S., Auffray, E., Lecoq, P., Mihóková, E., & Nikl, M. (2019). Core-shell ZnO:Ga-SiO₂ nanocrystals: Limiting particle agglomeration and increasing luminescence: Via surface defect passivation. *RSC Advances*, 9(50), 28946–28952. doi: 10.1039/c9ra04421c
- Protesescu, L., Yakunin, S., Bodnarchuk, M. I., Krieg, F., Caputo, R., Hendon, C. H., Yang, R. X., Walsh, A., & Kovalenko, M. V. (2015). Nanocrystals of Cesium Lead Halide Perovskites (CsPbX₃, X = Cl, Br, and I): Novel Optoelectronic Materials Showing Bright Emission with Wide Color Gamut. *Nano Letters*, 15(6), 3692–3696. doi: 10.1021/nl5048779
- Qin, Z., Dai, S., Hadjiev, V. G., Wang, C., Xie, L., Ni, Y., Wu, C., Yang, G., Chen, S., Deng, L., Yu, Q., Feng, G., Wang, Z. M., & Bao, J. (2019). Revealing the Origin of Luminescence Center in 0D Cs₄PbBr₆ Perovskite. *Chemistry of Materials*, 31(21), 9098–9104. doi: 10.1021/acs.chemmater.9b03426
- Quan, L. N., García de Arquer, F. P., Sabatini, R. P., & Sargent, E. H. (2018). Perovskites for Light Emission. *Advanced Materials*, 30(45), 1–19. doi: 10.1002/adma.201801996
- Ramasamy, P., Lim, D.-H., Kim, B., Lee, S.-H., Lee, M.-S., & Lee, J.-S. (2016). All-inorganic cesium lead halide perovskite nanocrystals for photodetector applications. *Chemical Communications*, 52(10), 2067–2070. doi: 10.1039/C5CC08643D
- Rao, L., Ding, X., Du, X., Liang, G., Tang, Y., Tang, K., & Zhang, J. Z. (2019). Ultrasonication-assisted synthesis of CsPbBr₃ and Cs₄PbBr₆ perovskite nanocrystals and their reversible transformation. *Beilstein Journal of Nanotechnology*, 10, 666–676. doi: 10.3762/bjnano.10.66
- Riesen, N., Lockrey, M., Badek, K., & Riesen, H. (2019). On the origins of the green luminescence in the “zero-dimensional perovskite” Cs₄PbBr₆: Conclusive results from

- cathodoluminescence imaging. *Nanoscale*, 11(9), 4001–4007. doi: 10.1039/c8nr09255a
- Rossignol, J., Turtos, R. M., Gundacker, S., Gaudreault, D., Auffray, E., Lecoq, P., Bérubé-Lauzière, Y., & Fontaine, R. (2020). Time-of-flight computed tomography - proof of principle. *Physics in Medicine and Biology*, 65(8). doi: 10.1088/1361-6560/ab78bf
- Saidaminov, M. I., Almutlaq, J., Sarmah, S., Dursun, I., Zhumekenov, A. A., Begum, R., Pan, J., Cho, N., Mohammed, O. F., & Bakr, O. M. (2016). Pure Cs₄PbBr₆: Highly Luminescent Zero-Dimensional Perovskite Solids. *ACS Energy Letters*, 1(4), 840–845. doi: 10.1021/acscenergylett.6b00396
- Sarkar, S. (2021). All-Inorganic Halide Perovskite Nanocrystals: Future Prospects and Challenges to Go Lead Free. *Physica Status Solidi (A)*, 218(14), 2100185. doi: 10.1002/pssa.202100185
- Sebastian, M., Peters, J. A., Stoumpos, C. C., Im, J., Kostina, S. S., Liu, Z., Kanatzidis, M. G., Freeman, A. J., & Wessels, B. W. (2015). Excitonic emissions and above-band-gap luminescence in the single-crystal perovskite semiconductors CsPbBr₃ and CsPbCl₃. *Physical Review B - Condensed Matter and Materials Physics*, 92(23), 1–9. doi: 10.1103/PhysRevB.92.235210
- Shao, H., Bai, X., Pan, G., Cui, H., Zhu, J., Zhai, Y., Liu, J., Dong, B., Xu, L., & Song, H. (2018). Highly efficient and stable blue-emitting CsPbBr₃@SiO₂ nanospheres through low temperature synthesis for nanoprinting and WLED. *Nanotechnology*, 29(28), 285706. doi: 10.1088/1361-6528/aac00b
- Song, J., Li, J., Li, X., Xu, L., Dong, Y., & Zeng, H. (2015). Quantum Dot Light-Emitting Diodes Based on Inorganic Perovskite Cesium Lead Halides (CsPbX₃). *Advanced Materials*, 27(44), 7162–7167. doi: 10.1002/adma.201502567
- Song, Y. H., Yoo, J. S., Kang, B. K., Choi, S. H., Ji, E. K., Jung, H. S., & Yoon, D. H. (2016). Long-term stable stacked CsPbBr₃ quantum dot films for highly efficient white light generation in LEDs. *Nanoscale*, 8(47), 19523–19526. doi: 10.1039/c6nr07410c
- Su, M. L., Zhang, Q., Gao, Y. J., Wang, D. X., Chen, C., & Wei, W. (2022). Enhanced luminescence of CsPbBr₃ nanocrystals-glass composite scintillators based on Ce³⁺-doped borosilicate glass. *Journal of Luminescence*, 242, 118553. doi: 10.1016/j.jlumin.2021.118553
- Suchá, A. (2019). Nevodná příprava anorganických scintilátorů a tenkých vrstev [výzkumný úkol]. *Czech Technical University in Prague*.
- Suchá, A. (2020). Příprava a charakterizace luminiscenčních tenkých vrstev pro pokročilé aplikace [Master's thesis]. *Czech Technical University in Prague*.
- Surti, S., Kuhn, A., Werner, M. E., Perkins, A. E., Kolthammer, J., & Karp, J. S. (2007). Performance of Philips Gemini TF PET/CT scanner with special consideration for its time-of-flight imaging capabilities. *Journal of Nuclear Medicine : Official Publication, Society of Nuclear Medicine*, 48(3), 471–480. Retrieved from <http://www.ncbi.nlm.nih.gov/pubmed/17332626>
- Swarnkar, A., Chulliyil, R., Ravi, V. K., Irfanullah, M., Chowdhury, A., & Nag, A. (2015). Colloidal CsPbBr₃ Perovskite Nanocrystals: Luminescence beyond Traditional Quantum Dots. *Angewandte Chemie International Edition*, 54(51), 15424–15428. doi: 10.1002/anie.201508276
- Swarnkar, A., Marshall, A. R., Sanehira, E. M., Chernomordik, B. D., Moore, D. T.,

- Christians, J. A., Chakrabarti, T., & Luther, J. M. (2016). Quantum dot–induced phase stabilization of α -CsPbI₃ perovskite for high-efficiency photovoltaics. *Science*, 354(6308), 92–95. doi: 10.1126/science.aag2700
- Tomanová, K., Čuba, V., Brik, M. G., Mihóková, E., Martinez Turtos, R., Lecoq, P., Auffray, E., & Nikl, M. (2019). On the structure, synthesis, and characterization of ultrafast blue-emitting CsPbBr₃ nanoplatelets. *APL Materials*, 7(1), 011104. doi: 10.1063/1.5079300
- Tong, Yao, Wang, Q., Yang, H., Liu, X., Mei, E., Liang, X., Zhang, Z., & Xiang, W. (2021). Enhanced multimodal luminescence and ultrahigh stability Eu³⁺-doped CsPbBr₃ glasses for X-ray detection and imaging. *Photonics Research*, 9(12), 2369. doi: 10.1364/prj.439744
- Tong, Yu, Bladt, E., Aygüler, M. F., Manzi, A., Milowska, K. Z., Hintermayr, V. A., Docampo, P., Bals, S., Urban, A. S., Polavarapu, L., & Feldmann, J. (2016). Highly Luminescent Cesium Lead Halide Perovskite Nanocrystals with Tunable Composition and Thickness by Ultrasonication. *Angewandte Chemie - International Edition*, 55(44), 13887–13892. doi: 10.1002/anie.201605909
- Tsiwah, E. A., Ding, Y., Li, Z., Zhao, Z., Wang, M., Hu, C., Liu, X., Sun, C., Zhao, X., & Xie, Y. (2017). One-pot scalable synthesis of all-inorganic perovskite nanocrystals with tunable morphology, composition and photoluminescence. *CrystEngComm*, 19(46), 7041–7049. doi: 10.1039/C7CE01749A
- Turtos, R. M., Gundacker, S., Auffray, E., & Lecoq, P. (2019). Towards a metamaterial approach for fast timing in PET: experimental proof-of-concept. *Physics in Medicine & Biology*, 64(18), 185018. doi: 10.1088/1361-6560/ab18b3
- Turtos, R. M., Gundacker, S., Omelkov, S., Mahler, B., Khan, A. H., Saaring, J., Meng, Z., Vasil'ev, A., Dujardin, C., Kirm, M., Moreels, I., Auffray, E., & Lecoq, P. (2019). On the use of CdSe scintillating nanoplatelets as time taggers for high-energy gamma detection. *Npj 2D Materials and Applications*, 3(1), 1–10. doi: 10.1038/s41699-019-0120-8
- Vaněček, V., Děcká, K., Mihóková, E., Čuba, V., Král, R., & Nikl, M. (2022). Advanced Halide Scintillators: From the Bulk to Nano. *Advanced Photonics Research*, 2200011, in press. doi: 10.1002/adpr.202200011
- Wang, C., Lin, H., Zhang, Z., Qiu, Z., Yang, H., Cheng, Y., Xu, J., Xiang, X., Zhang, L., & Wang, Y. (2020). X-ray excited CsPb(Cl,Br)₃ perovskite quantum dots-glass composite with long-lifetime. *Journal of the European Ceramic Society*, 40(5), 2234–2238. doi: 10.1016/j.jeurceramsoc.2020.01.016
- Wang, H. C., Lin, S. Y., Tang, A. C., Singh, B. P., Tong, H. C., Chen, C. Y., Lee, Y. C., Tsai, T. L., & Liu, R. S. (2016). Mesoporous Silica Particles Integrated with All-Inorganic CsPbBr₃ Perovskite Quantum-Dot Nanocomposites (MP-PQDs) with High Stability and Wide Color Gamut Used for Backlight Display. *Angewandte Chemie - International Edition*, 55(28), 7924–7929. doi: 10.1002/anie.201603698
- Wang, R., Mujahid, M., Duan, Y., Wang, Z., Xue, J., & Yang, Y. (2019). A Review of Perovskites Solar Cell Stability. *Advanced Functional Materials*, 29(47), 1808843. doi: 10.1002/adfm.201808843
- Xu, J., Huang, W., Li, P., Onken, D. R., Dun, C., Guo, Y., Ucer, K. B., Lu, C., Wang, H., Geyer, S. M., Williams, R. T., & Carroll, D. L. (2017). Imbedded Nanocrystals of CsPbBr₃ in Cs₄PbBr₆: Kinetics, Enhanced Oscillator Strength, and Application in

- Light-Emitting Diodes. *Advanced Materials*, 29(43), 1–10. doi: 10.1002/adma.201703703
- Xu, L. J., Worku, M., He, Q., & Ma, B. (2020). Advances in light-emitting metal-halide perovskite nanocrystals. *MRS Bulletin*, 45(6), 458–466. doi: 10.1557/mrs.2020.143
- Xu, Q., Wang, J., Shao, W., Ouyang, X., Wang, X., Zhang, X., Guo, Y., & Ouyang, X. (2020). A solution-processed zero-dimensional all-inorganic perovskite scintillator for high resolution gamma-ray spectroscopy detection. *Nanoscale*, 12(17), 9727–9732. doi: 10.1039/d0nr00772b
- Xu, Y., Chen, Q., Zhang, C., Wang, R., Wu, H., Zhang, X., Xing, G., Yu, W. W., Wang, X., Zhang, Y., & Xiao, M. (2016). Two-Photon-Pumped Perovskite Semiconductor Nanocrystal Lasers. *Journal of the American Chemical Society*, 138(11), 3761–3768. doi: 10.1021/jacs.5b12662
- Yakunin, S., Protesescu, L., Krieg, F., Bodnarchuk, M. I., Nedelcu, G., Humer, M., De Luca, G., Fiebig, M., Heiss, W., & Kovalenko, M. V. (2015). Low-threshold amplified spontaneous emission and lasing from colloidal nanocrystals of caesium lead halide perovskites. *Nature Communications*, 6, 1–8. doi: 10.1038/ncomms9056
- Yang, H., Li, H., Yuan, R., Chen, J., Zhao, J., Wang, S., Liu, Y., Li, Q., & Zhang, Z. (2021). A novel scintillation screen for achieving high-energy ray detection with fast and full-color emission. *Journal of Materials Chemistry C*, 9(25), 7905–7909. doi: 10.1039/D1TC01318A
- Yang, L., Wang, T., Yang, X., Zhang, M., Pi, C., Yu, J., Zhou, D., Yu, X., Qiu, J., & Xu, X. (2019). Extrinsic photoluminescence properties of individual micro-particle of Cs₄PbBr₆ perovskite with “defect” structure. *Optics Express*, 27(22), 31207. doi: 10.1364/oe.27.031207
- Ye, S., Yu, M., Zhao, M., Song, J., & Qu, J. (2018). Low temperature synthesis of high-quality all-inorganic cesium lead halide perovskite nanocrystals in open air and their upconversion luminescence. *Journal of Alloys and Compounds*, 730, 62–70. doi: 10.1016/j.jallcom.2017.09.284
- Yin, J., Yang, H., Song, K., El-Zohry, A. M., Han, Y., Bakr, O. M., Brédas, J. L., & Mohammed, O. F. (2018). Point Defects and Green Emission in Zero-Dimensional Perovskites. *Journal of Physical Chemistry Letters*, 9(18), 5490–5495. doi: 10.1021/acs.jpcclett.8b02477
- Zhang, F., Zhong, H., Chen, C., Wu, X. G., Hu, X., Huang, H., Han, J., Zou, B., & Dong, Y. (2015). Brightly luminescent and color-tunable colloidal CH₃NH₃PbX₃ (X = Br, I, Cl) quantum dots: Potential alternatives for display technology. *ACS Nano*, 9(4), 4533–4542. doi: 10.1021/acsnano.5b01154
- Zhang, H., Yang, Z., Zhou, M., Zhao, L., Jiang, T., Yang, H., Yu, X., Qiu, J., Yang, Y. (Michael), & Xu, X. (2021). Reproducible X-ray Imaging with a Perovskite Nanocrystal Scintillator Embedded in a Transparent Amorphous Network Structure. *Advanced Materials*, 33(40), 2102529. doi: 10.1002/adma.202102529
- Zhang, J., Hodes, G., Jin, Z., & Liu, S. (Frank). (2019). All-Inorganic CsPbX₃ Perovskite Solar Cells: Progress and Prospects. *Angewandte Chemie International Edition*, 58(44), 15596–15618. doi: 10.1002/anie.201901081
- Zhang, L., Liang, W., Xu, L., Zhu, M., Wang, X., Su, J., Li, L., Liu, N., Zhang, Z., & Gao, Y. (2021). Room-temperature quaternary alkylammonium passivation toward

- morphology-controllable CsPbBr₃ nanocrystals with excellent luminescence and stability for white LEDs. *Chemical Engineering Journal*, 417, 129349. doi: 10.1016/j.cej.2021.129349
- Zhang, Yangning, Siegler, T. D., Thomas, C. J., Abney, M. K., Shah, T., De Gorostiza, A., Greene, R. M., & Korgel, B. A. (2020). A “tips and Tricks” Practical Guide to the Synthesis of Metal Halide Perovskite Nanocrystals. *Chemistry of Materials*, 32(13), 5410–5423. doi: 10.1021/acs.chemmater.0c01735
- Zhang, Yuhai, Saidaminov, M. I., Dursun, I., Yang, H., Murali, B., Alarousu, E., Yengel, E., Alshankiti, B. A., Bakr, O. M., & Mohammed, O. F. (2017). Zero-Dimensional Cs₄PbBr₆ Perovskite Nanocrystals. *Journal of Physical Chemistry Letters*, 8(5), 961–965. doi: 10.1021/acs.jpcclett.7b00105
- Zhong, Q., Cao, M., Hu, H., Yang, D., Chen, M., Li, P., Wu, L., & Zhang, Q. (2018). One-Pot Synthesis of Highly Stable CsPbBr₃@SiO₂ Core–Shell Nanoparticles. *ACS Nano*, 12(8), 8579–8587. doi: 10.1021/acsnano.8b04209
- Zhu, J., Deng, C., Jiang, H., Zheng, Z., Gong, R., Bi, Y., Zhang, L., & Lin, R. (2016). The impact of fluorescent dyes on the performances of polystyrene-based plastic scintillators. *Nuclear Instruments and Methods in Physics Research, Section A: Accelerators, Spectrometers, Detectors and Associated Equipment*, 835, 136–141. doi: 10.1016/j.nima.2016.08.018
- Zhu, Z., Sun, Q., Zhang, Z., Dai, J., Xing, G., Li, S., Huang, X., & Huang, W. (2018). Metal halide perovskites: stability and sensing-ability. *Journal of Materials Chemistry C*, 6(38), 10121–10137. doi: 10.1039/C8TC03164A

On the structure, synthesis, and characterization of ultrafast blue-emitting CsPbBr₃ nanoplatelets

Cite as: APL Mater. 7, 011104 (2019); <https://doi.org/10.1063/1.5079300>

Submitted: 30 October 2018 . Accepted: 04 January 2019 . Published Online: 23 January 2019

Kateřina Tomanová, Václav Čuba, Mikhail G. Brik , Eva Mihóková , Rosana Martinez Turtos , Paul Lecoq , Etienne Auffray, and Martin Nikl 




Measure Ready
M91 FastHall™ Controller

A revolutionary new instrument for complete Hall analysis

Lake Shore
CRYOTRONICS



APL Mater. 7, 011104 (2019); <https://doi.org/10.1063/1.5079300>

7, 011104

© 2019 Author(s).

On the structure, synthesis, and characterization of ultrafast blue-emitting CsPbBr₃ nanoplatelets

Cite as: *APL Mater.* **7**, 011104 (2019); doi: [10.1063/1.5079300](https://doi.org/10.1063/1.5079300)
 Submitted: 30 October 2018 • Accepted: 4 January 2019 •
 Published Online: 23 January 2019



Kateřina Tomanová,^{1,a)} Václav Čuba,¹ Mikhail G. Brik,^{2,3,4,5} Eva Mihóková,⁵ Rosana Martinez Turtos,⁶ Paul Lecoq,⁶ Etienne Auffray,⁶ and Martin Nikl⁵

AFFILIATIONS

¹Department of Nuclear Chemistry, Faculty of Nuclear Sciences and Physical Engineering, Czech Technical University in Prague, Břehová 7, Prague 115 19, Czech Republic

²College of Sciences, Chongqing University of Posts and Telecommunications, Chongqing 400065, People's Republic of China

³Institute of Physics, University of Tartu, W. Ostwald Str. 1, Tartu 50411, Estonia

⁴Institute of Physics, Jan Dlugosz University, Armii Krajowej 13/15, PL-42200 Czestochowa, Poland

⁵Department of Optical Materials, Institute of Physics of the Czech Academy of Sciences, Cukrovarnická 10, Prague 162 53, Czech Republic

⁶CERN, 1211 Geneva 23, Switzerland

Note: This paper is part of the special topic on Perovskite Semiconductors for Next Generation Optoelectronic Applications.

a) Author to whom correspondence should be addressed: Katerina.Tomanova@fjfi.cvut.cz

ABSTRACT

Recent developments in medical imaging techniques, in particular, those in time-of-flight positron emission tomography put new challenges on scintillating material performance that cannot be fulfilled by conventional scintillators. Bright and ultrafast nanoparticles represent promising candidates to build up an advanced detection system needed. We synthesize colloidal CsPbBr₃ nanoplatelets emitting blue light with fast sub-nanosecond decay. We also prepare a nanocomposite material by embedding the nanoplatelets in the polystyrene matrix. We show that blue emission is preserved provided the composite is not exposed to UV/vis light and/or elevated temperatures. Motivated by conflicting information from the literature about the room temperature structure of colloidal CsPbX₃ (X = Cl, Br, I) particles, that results being orthorhombic, rather than cubic, we perform *ab initio* electronic structure calculations of bulk crystals with an orthorhombic structure. We calculate optical properties, as well as exciton diameters and binding energies and compare them to those previously obtained for cubic CsPbX₃ crystals.

© 2019 Author(s). All article content, except where otherwise noted, is licensed under a Creative Commons Attribution (CC BY) license (<http://creativecommons.org/licenses/by/4.0/>). <https://doi.org/10.1063/1.5079300>

Inorganic scintillators are commonly used for detection of ionizing radiation in a variety of applications. A forefront field of interest focuses on medical applications, such as imaging systems for medical diagnosis.¹⁻⁵ For positron emission tomography (PET) imaging, the key performance parameters are the quality of the reconstructed image together with the possibility to detect small tumors and to access dynamically different molecular pathways with the minimum radioactive dose injected to the patient.⁶ This put specific requirements on the scintillating material characteristics. In recent years, the fast timing capability received particular attention driven

by the time-of-flight PET.⁷⁻¹⁰ Desired coincidence time resolution (CTR) in the range of 100 ps FWHM can be achieved via high light yield and very short rise and decay times of the scintillation light.^{11,12} In lately developed efforts to push CTR even further down to 10 ps,¹³ one needs to consider mechanisms involving a production of prompt photons. One option is to create heterostructures combining standard dense scintillators like LSO and nanocrystals. The latter, due to quantum confinement, can feature enhanced optical properties, in particular, high quantum efficiency and ultrafast decay time, with respect to their bulk counterparts. Colloidal semiconductors,

such as colloidal CdSe nanosheets¹⁴ or cesium lead halide perovskites, seem to be promising candidates to pursue.

Cesium lead halide perovskites CsPbX_3 ($X = \text{Cl, Br, I}$) are under intense investigation due to their potential applications in various fields, such as photovoltaics,^{15,16} optoelectronic devices,¹⁷⁻¹⁹ or X-ray and gamma-ray detectors.^{20,21}

The bulk CsPbX_3 crystals have been reported already in 1950s.²² Their perovskite structure undergoes phase transitions induced by temperature.²³⁻²⁵ The cubic phase with the space group $\text{Pm}\bar{3}\text{m}$ is stable only at higher temperatures.²⁶⁻²⁸ At room temperature, the bulk CsPbCl_3 ,²⁹ CsPbBr_3 ,²⁸ and CsPbI_3 ²¹ possess a thermodynamically preferred orthorhombic structure with the space group Pnma .

Earlier photoluminescence studies have shown the presence of the 2.98 eV and 2.32 eV peaks in CsPbCl_3 and CsPbBr_3 , respectively, that were attributed to recombination of Mott-Wannier excitons.³⁰⁻³² Formation of CsPbX_3 quantum dots (QDs) was observed in CsX:Pb host matrices.³³⁻³⁵ Thanks to quantum confinement effect the excitonic luminescence of QDs featured subnanosecond decay times, namely, 90 ps at 10 K in CsPbBr_3 ³⁴ and 30 ps at 10 K in CsPbCl_3 .³³ More recently, colloidal nanocrystal QDs of CsPbX_3 or mixed halide systems Cl/Br and Br/I have been synthesized.¹⁷ Based on X-ray diffraction (XRD) patterns, the authors claimed that their structure was cubic. These QDs provide high quantum yields, narrow emission bands, and room temperature decay times within 1-29 ns. The emission is tunable within the entire visible spectral range by changing halide composition or the particle size. The latter is directly linked to quantum confinement effects that can be observed for the particle diameter comparable or smaller with respect to the delocalization length of an exciton in the corresponding bulk material. This quantity, Bohr diameter, together with exciton binding energies were calculated by density functional theory (DFT) methods and effective mass approximation for cubic structures of CsPbX_3 .¹⁷ However, other studies of bright colloidal CsPbX_3 nanocrystals bring conflicting information about their structure. Similar to the study by Protesescu *et al.*,¹⁷ the colloidal CsPbBr_3 nanoplatelets¹⁹ were also reported as cubic, while CsPbBr_3 QDs³⁶ and CsPbX_3 nanowires^{37,38} as orthorhombic. To resolve the problem, the structure of colloidal CsPbBr_3 QDs was thoroughly investigated using Rietveld refinements and PDF analysis of synchrotron X-ray total scattering data.³⁹ Based on the results, the authors concluded that the structure was orthorhombic Pnma rather than cubic $\text{Pm}\bar{3}\text{m}$. They also pointed out that deviation in the structure may have a nontrivial impact on the electronic band structure and related quantities determined in the study by Protesescu *et al.*¹⁷ that were based on the cubic crystal structure of the material.

Ab initio calculations of the CsPbX_3 electronic band structure were performed in a number of studies. Besides all halides studied by Protesescu *et al.*,¹⁷ the cubic structure of CsPbCl_3 was recently also studied by Ghebouli *et al.*,⁴⁰ that of CsPbBr_3 in Refs. 41-43, and that of CsPbI_3 in Refs. 41, 42, 44, and 45. The calculations associated with the orthorhombic structure of CsPbBr_3 are reported in Refs. 46 and 47 and that of CsPbI_3 in Refs. 41, 42, 44, and 45. Nevertheless, to our knowledge, no systematic *ab initio* calculations of the electronic structure

of all three cesium lead halides with orthorhombic structure Pnma have been reported. In particular, possible impact of the orthorhombic crystal structure on appearance of quantum confinement effects has not been addressed.

In this paper, we synthesize colloidal CsPbBr_3 nanoplatelets exhibiting strong quantum confinement effects leading to their fast subnanosecond decay. X-ray powder diffraction (XRPD) measurements of prepared material confirm its orthorhombic structure. To demonstrate the practical applicability of the material for development of the detector system, we incorporate the nanoplatelets into the polystyrene host matrix. In the light of previous conclusions³⁹ (confirmed as well in the present work) about the structure of CsPbBr_3 colloidal nanoparticles being orthorhombic, we also consider in detail the structure of CsPbX_3 ($X = \text{Cl, Br, I}$) and perform *ab initio* electronic structure calculations of CsPbX_3 crystals with the orthorhombic structure. In addition, we calculate physical quantities linked to quantum confinement effects that help to assess boundaries for obtaining nanoparticles with enhanced optical properties compared to the corresponding bulk material.

Following chemicals were used for preparation of CsPbBr_3 nanoplatelets, and CsPbBr_3 polystyrene nanocomposite materials: CsBr (99.999%, Sigma-Aldrich), PbBr_2 (99.999%, Sigma-Aldrich), N,N-dimethylformamide (DMF, anhydrous, 99.8%, Sigma-Aldrich), oleic acid (OA, 99%, Sigma-Aldrich), oleylamine (OAm, 70%, Sigma-Aldrich), toluene (anhydrous, 99.8%, Sigma-Aldrich), and polystyrene (PS, no additives, Nuvia). All chemicals were used as received without further purification.

X-ray powder diffraction (XRPD) was measured using a Rigaku Miniflex 600 diffractometer equipped with the Cu X-ray tube (average wavelength $K_{\alpha 1,2}$ 0.15418 nm, voltage 40 kV, current 15 mA). Data were collected with a speed of $2^\circ/\text{min}$ and compared with the ICDD PDF-2 database, version 2013. The transmission electron microscopy (TEM) was obtained using an EM201 microscope (Philips). The radioluminescence (RL) and photoluminescence (PL) spectra were collected using the spectrofluorimeter 5000M (Horiba Jobin Yvon) with the monochromator and photodetector TBX-04. The excitation

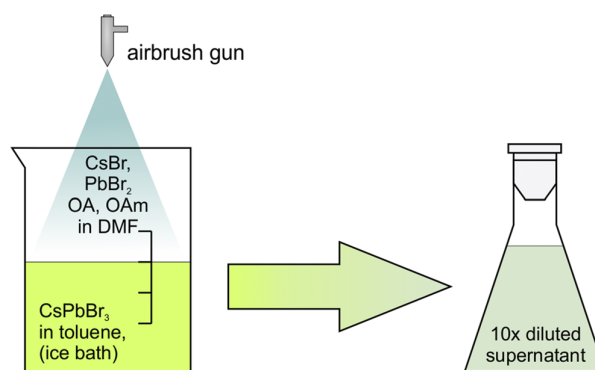


FIG. 1. Synthesis procedure of CsPbBr_3 using airbrush gun and ice bath.

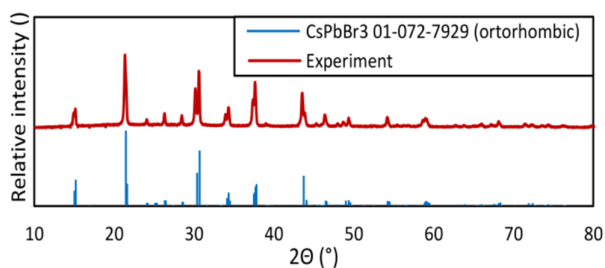


FIG. 2. XRPD pattern of the precipitated material after centrifugation.

sources were X-ray tube Seifert (40 kV, 15 mA) for radioluminescence (RL) measurements and deuterium lamp for photoluminescence (PL) measurements. The PL decays were measured using excitation by nanoLED with nanosecond pulses (300 nm). The time resolved PL spectra were obtained using the Hamamatsu C10910 streak camera with 18 ps time resolution and laser excitation (PiLAS, 372 nm).

For the synthesis, the modified procedure first described in the study by Li *et al.*¹⁸ was used (Fig. 1).

The resulting colloidal solution exhibited a blue emission under UV excitation (365 nm). The solution was centrifuged for 10 min (12 000 g) in order to separate the largest crystals, and the supernatant was collected and characterized using XRPD (the solution was drop-casted on a glass sample holder), PL, and TEM. After characterization, the solution was diluted 10× to enhance the stability of colloidal particles (aka nanocrystals).

Embedding procedure is described in detail in the [supplementary material](#). The resulting PS film (0.5 mm thick, 0.1 wt.% loading) also exhibited a blue emission under UV excitation (365 nm). The stability of the film evaporated at room temperature was studied at ambient conditions, and the RL spectrum was collected after 2 weeks. The second sample (see the [supplementary material](#)) was stored in the dark at 4 °C, and the RL spectrum was collected immediately after the solvent evaporation.

The XRPD pattern (Fig. 2) of the precipitated material after centrifugation (see experimental details in the [supplementary](#)

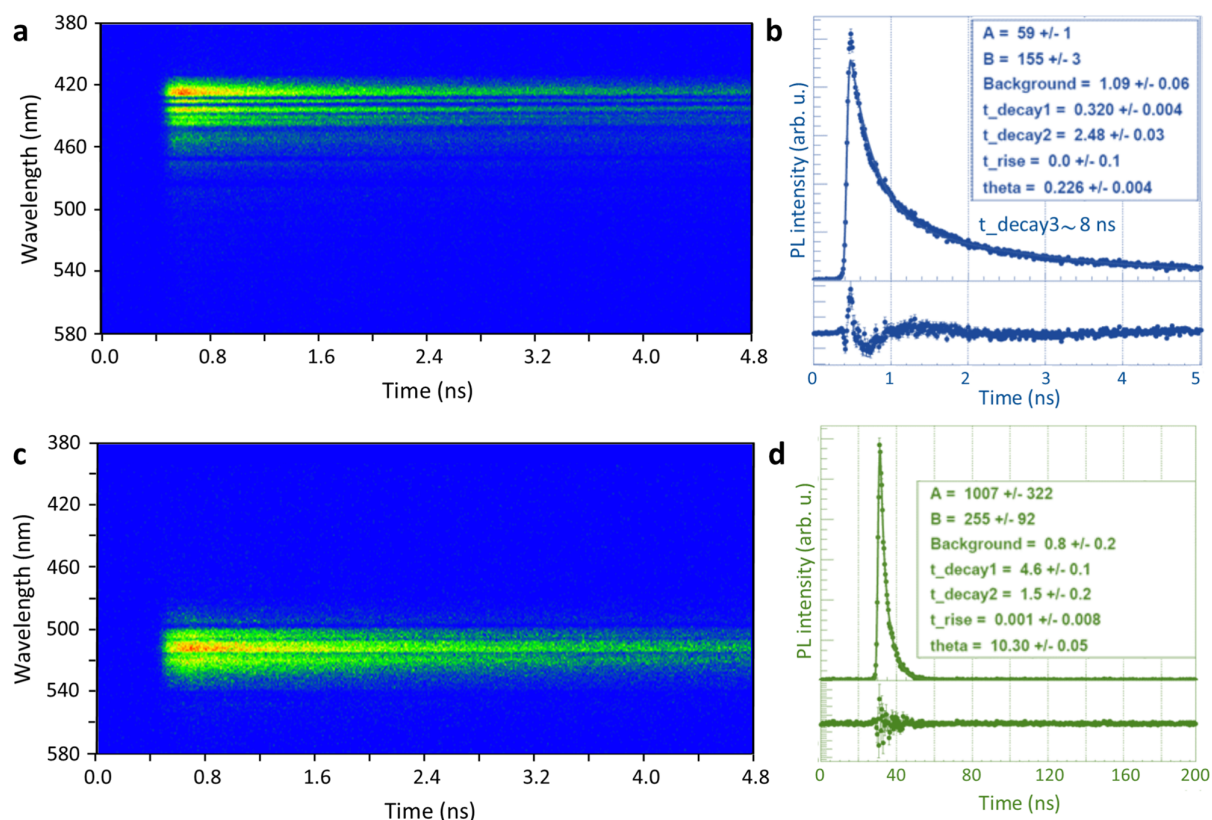


FIG. 3. Time resolved PL spectrum of the blue emission from the colloidal sample with maximum at 425 nm (a) and its decay curve (b) and time resolved PL spectrum of the green emission with maximum at 512 nm (c) and its decay curve (d). Excited by laser (372 nm).

material) compared to the ICDD PDF-2 database shows that the prepared material is orthorhombic CsPbBr₃.

Without slowing down the reaction rate (see experimental details in the [supplementary material](#)), the colloidal solution contained a mixture of blue and green emitting crystals. [Figure 3](#) shows time resolved PL spectra of the colloidal sample drop-casted on a glass substrate. The results indicate the presence of two types of nanocrystals. The first type exhibits a blue emission with maximum at 425 nm, which belongs to nanocrystals with strongly quantum confined excitons. This result is further confirmed by decay measurements that show

a three component decay with the fastest decay time of 320 ps [see [Fig. 3\(b\)](#)]. The second type of the particles exhibits green emission centered at 512 nm with slower decay longer than 1 ns.

With slowing down the reaction rate, it is possible to suppress the green emission, i.e., significantly decrease the concentration of larger nanocrystals. [Figure 4\(e\)](#) shows strong blue emission of the sample under the 365 nm excitation.

The size distribution of the obtained blue-emitting material is still quite broad, but the results in [Fig. 4](#) show that the majority of the material is in the form of colloidal

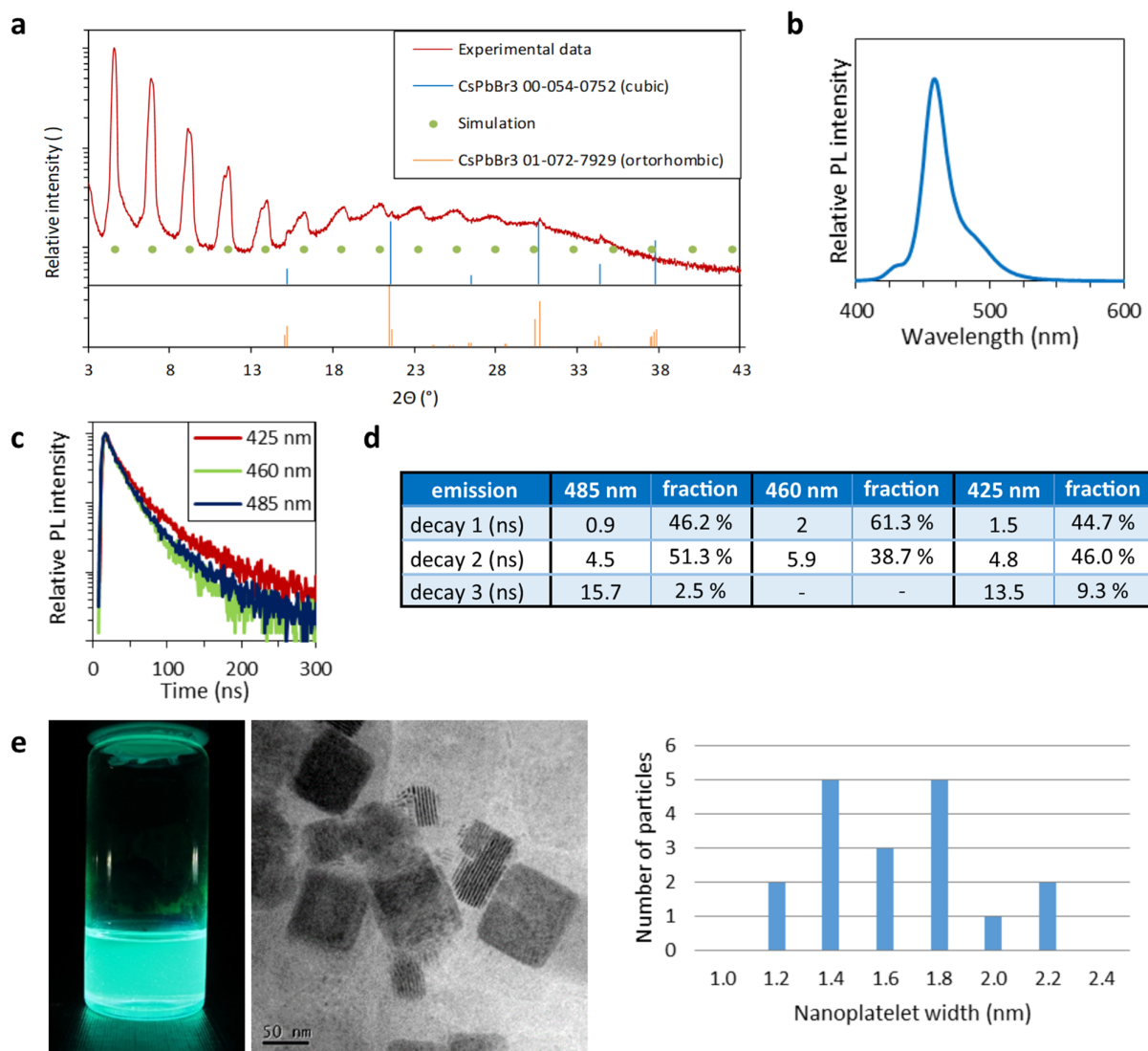


FIG. 4. XRPD pattern of drop-casted colloidal sample (a), PL spectrum of the colloidal sample excited by 300 nm (b), PL decay curves of all three maxima (c), and corresponding decay times (d), photograph under 365 nm excitation, TEM image, and size distribution of the nanoplatforms (e).

nanoplatelets. Another supporting evidence for this conclusion can be found in the [supplementary material](#) (absorption spectrum).

In [Fig. 4\(a\)](#), the XRPD pattern of a drop-casted blue-emitting film is presented. The high noise level can be explained by the presence of amorphous OA and OAm. Diffraction peaks emerging from the noise are compared to both cubic and orthorhombic phases of CsPbBr₃. However, high noise prevents the possibility to distinguish whether the phase is cubic or orthorhombic for the simple reason that diffraction maxima of the cubic phase are located at the same positions as the most intense diffraction maxima of the orthorhombic phase. Due to the confirmed orthorhombic phase of the precipitated material (cf. [Fig. 2](#)) and results reported in the study by Cottingham and Brutchey,³⁹ we believe that the present phase is orthorhombic rather than cubic. The main feature of the diffractogram is an interesting pattern of peaks with decreasing intensity. A simulation shows that it could be attributed to a repeating pattern of single lattice planes with an interplanar spacing of 38 Å. Coincidentally, based on the TEM images [[Fig. 4\(e\)](#)], it corresponds to the distance between two nanoplatelets stuck together.

The size distribution obtained from the TEM image in [Fig. 4\(e\)](#) show that based on the assumption of the orthorhombic structure (the size of the PbBr₆ octahedron 5.936 Å as calculated below, see [Fig. 8](#)), the majority of the nanoplatelets have a width corresponding to 2–3 monolayers.

The PL spectrum of the colloidal solution of nanoplatelets is presented in [Fig. 4\(b\)](#). The excitonic peak is shifted to shorter wavelengths compared to the bulk material, and its shape suggests that it is a combination of several emission bands. The emission maxima are positioned at about 430 nm, 458 nm, and 490 nm. This confirms the presence of nanoplatelets consisting of different numbers of monolayers.

The PL decay was measured for all three emission maxima; see [Fig. 4\(c\)](#). The fastest decay component has the decay time of 0.9 ns [[Fig. 4\(d\)](#)]. Compared to the result from green-emitting larger nanocrystals [1.5 ns, [Fig. 3\(d\)](#)], it is considerably accelerated due to strong quantum confinement effects.

Nanoplatelets of CsPbBr₃ were successfully embedded in a polystyrene matrix with approximately 0.1 wt. % loading. This step is crucial for a development of a detector based on this material further combined with a classical heavy scintillator with the high light yield, such as LYSO:Ce.¹³ It is also necessary to enhance the overall stability of CsPbBr₃ nanoplatelets. Resulting composites show good optical quality and sufficient transparency; see [Fig. 5](#).

[Figure 5\(a\)](#) shows a comparison of RL spectra of two samples: one stored in the dark at 4 °C and one stored at ambient conditions for 2 weeks. The emission band centered at about 320 nm belongs to a polystyrene matrix. The other band around 500 nm is attributed to CsPbBr₃ excitonic emission that is shifted with respect to the bulk material with the shift depending on a particle size (or more precisely the size of the largest particles present in the matrix). The 0.1 wt. % loading is apparently not enough to efficiently transfer the energy from the polystyrene matrix (320 nm emission) toward CsPbBr₃

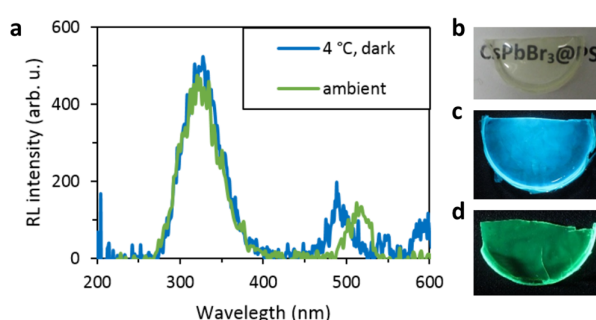


FIG. 5. RL spectrum of CsPbBr₃ embedded in a polystyrene stored in dark at 4 °C and of CsPbBr₃ embedded in a polystyrene after 2 weeks storage at ambient conditions [daylight, room temperature 30 °C (a)], photographs of samples in the daylight (b), and under 365 nm UV light [(c) for the sample kept in dark and cold, (d) for the sample kept at ambient conditions].

nanoplatelets, and further work is in progress to increase the loading at least ten times. It can be concluded that elevated temperature and the exposure to UV/vis light probably cause a diffusion of the nanoplatelets in the PS matrix. This may lead to their agglomeration into larger particles.

The local density approximation (LDA) and the general gradient approximation (GGA) methods were employed to calculate the structural, electronic, and optical properties of CsPbX₃ (X = Cl, Br, I). For further details on computation methods, please see the [supplementary material](#).

All three compounds crystallize in the Pnma space group (No. 62) with four formula units in one unit cell. The Pb ions are surrounded by six halide anions, forming slightly distorted octahedra. These octahedra are corner-sharing in CsPbCl₃, CsPbBr₃ (aligned along the b axis) and are isolated from each other in CsPbI₃. [Figures 6](#) and [7](#) show the unit cells of these materials as seen along the c and b axes.

Different characters of the PbX₆ (X = Cl, Br, I) octahedral orientation in the crystal lattices is clearly seen from these figures. Not only these octahedral units have different geometrical arrangements but their local structure also changes from one host to another. [Figure 8](#) shows the enlarged views of the PbX₆ complexes with indication of the Pb–X distances (in Å). All halide anions in these figures are labeled by the Roman numbers to analyze the angles between the chemical bonds and assess in this way degree of deviation of each of these octahedra from the ideal octahedral symmetry.

It is easy to see then that both PbCl₆ and PbBr₆ octahedral structural units have the inversion center (the opposite chemical bonds in the octahedra are equal, and the corresponding angles are 180°), whereas the PbI₆ complex does not, as confirmed by the analysis of the interatomic distances and angles between the chemical bonds ([Fig. 8](#) and [Table S1](#) in the [supplementary material](#)).

The ideal octahedron has three angles of 180° (three pairs of opposite vertices) and twelve angles of 90°. It can be noticed from [Table S1](#) (see the [supplementary material](#)) that the PbCl₆ complex has the highest symmetry among the

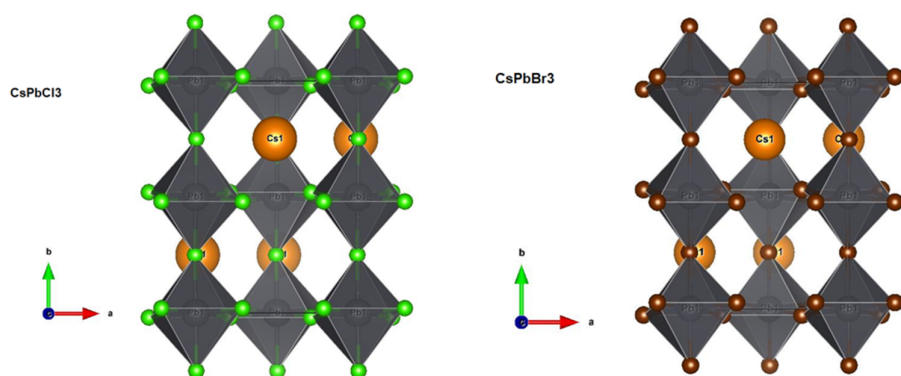


FIG. 6. One unit cell of CsPbCl_3 , CsPbBr_3 , and CsPbI_3 (a view along the c axis). Drawn with VESTA.⁴⁸

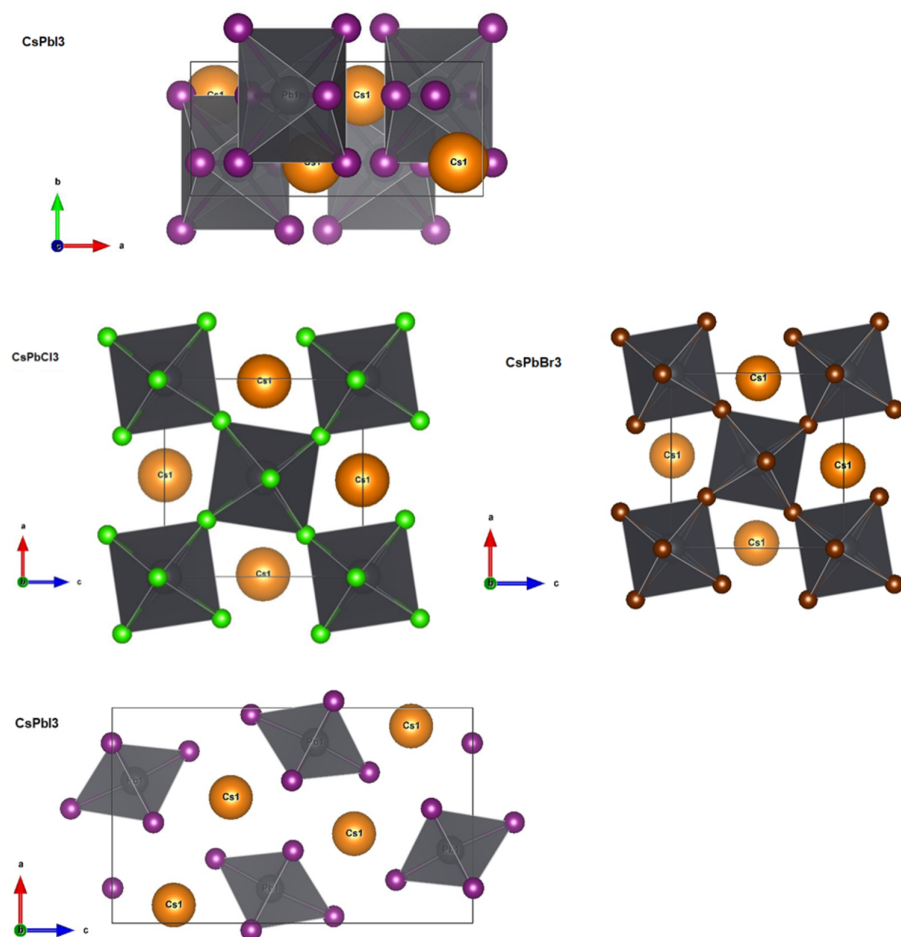


FIG. 7. One unit cell of CsPbCl_3 , CsPbBr_3 , and CsPbI_3 (a view along the b axis). Drawn with VESTA.⁴⁸

considered PbX_6 units; the differences between the ideal octahedron angles and the ones in the PbCl_6 cluster are less than one degree. Deviations of the actual symmetry from the ideal octahedral case increase with increasing the halide ion atomic

number (or its ionic radius). The PbI_6 complex loses its center of inversion and is characterized by the largest differences between its octahedral angles and an ideal octahedron among the considered three cases.

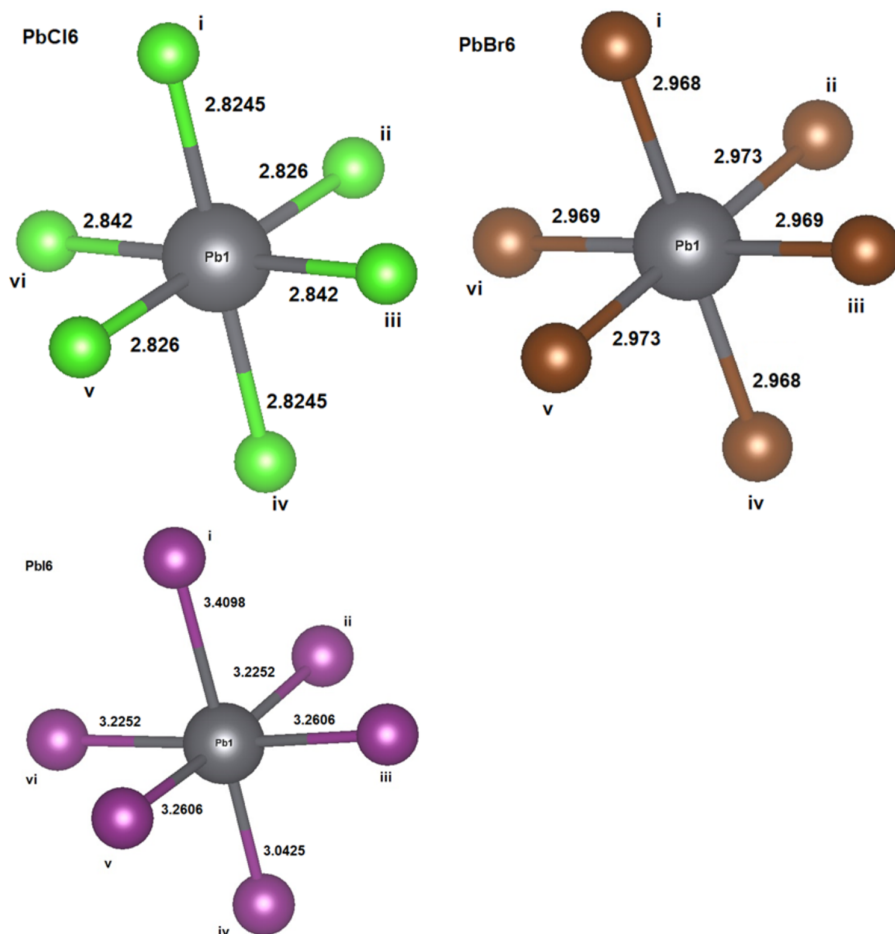


FIG. 8. Octahedral PbX_6 ($X = \text{Cl}, \text{Br}, \text{I}$) complexes in CsPbCl_3 , CsPbBr_3 , and CsPbI_3 . The Pb-X distances (in Å) are given. Drawn with VESTA.⁴⁸

The summary of the experimental and calculated structural data for CsPbX_3 is given in Table S2 in the [supplementary material](#). Good agreement between the experimental (taken as an initial input structure) and optimized lattice constants was achieved. In addition, the calculated and experimental fractional coordinates of all ions in the unit cells agree well with each other. It can be noticed that the LDA-calculated lattice constants are always somewhat smaller than the GGA-calculated ones. [Figure 9](#) shows the calculated band structures for all three studied crystals.

All three hosts appear to be the direct bandgap materials. The maximum of the valence band (VB) and minimum of the conduction band (CB) in CsPbCl_3 and CsPbBr_3 are realized at the G point (Brillouin zone center); however in CsPbI_3 , such situation takes place at the Y point. It can be, however, noted that in the case of the chloride and bromide materials, the CB minima at the G and X points are practically equal, which may imply certain ambiguity in determination of the bandgap character, both theoretically and experimentally. There is a remarkable difference in the character of the calculated bands

between CsPbCl_3 and CsPbBr_3 on the one hand and CsPbI_3 on the other hand. If for the former two compounds the VB and CB states exhibit pronounced dispersion and there are rather deep valleys away from the G point, for the latter material, the electronic states at the VB top are practically flat, which indicates very low mobility of the holes in CsPbI_3 . This may be due to the isolated PbI_6 units in the compound. Similarly, flat profiles of the VB top states were obtained in earlier publications.^{41,42,44} The CB states in CsPbI_3 are also rather flat, except for the Y-S direction, showing a low mobility of the electrons as well.

The origin of the electronic states in the calculated bands can be understood with the help of the density of states (DOS) diagrams, as shown in [Fig. 10](#).

The lower CB states in all studied halides are composed of the lead 6p orbitals; the upper CB states are made up by the Cs 6s states. The central parts of the VB are dominated by the halides p states (3p for Cl, 4p for Br, and 5p for I), but an important feature is that the topmost VB levels are due to the Pb 6s states, so the lower energy part of

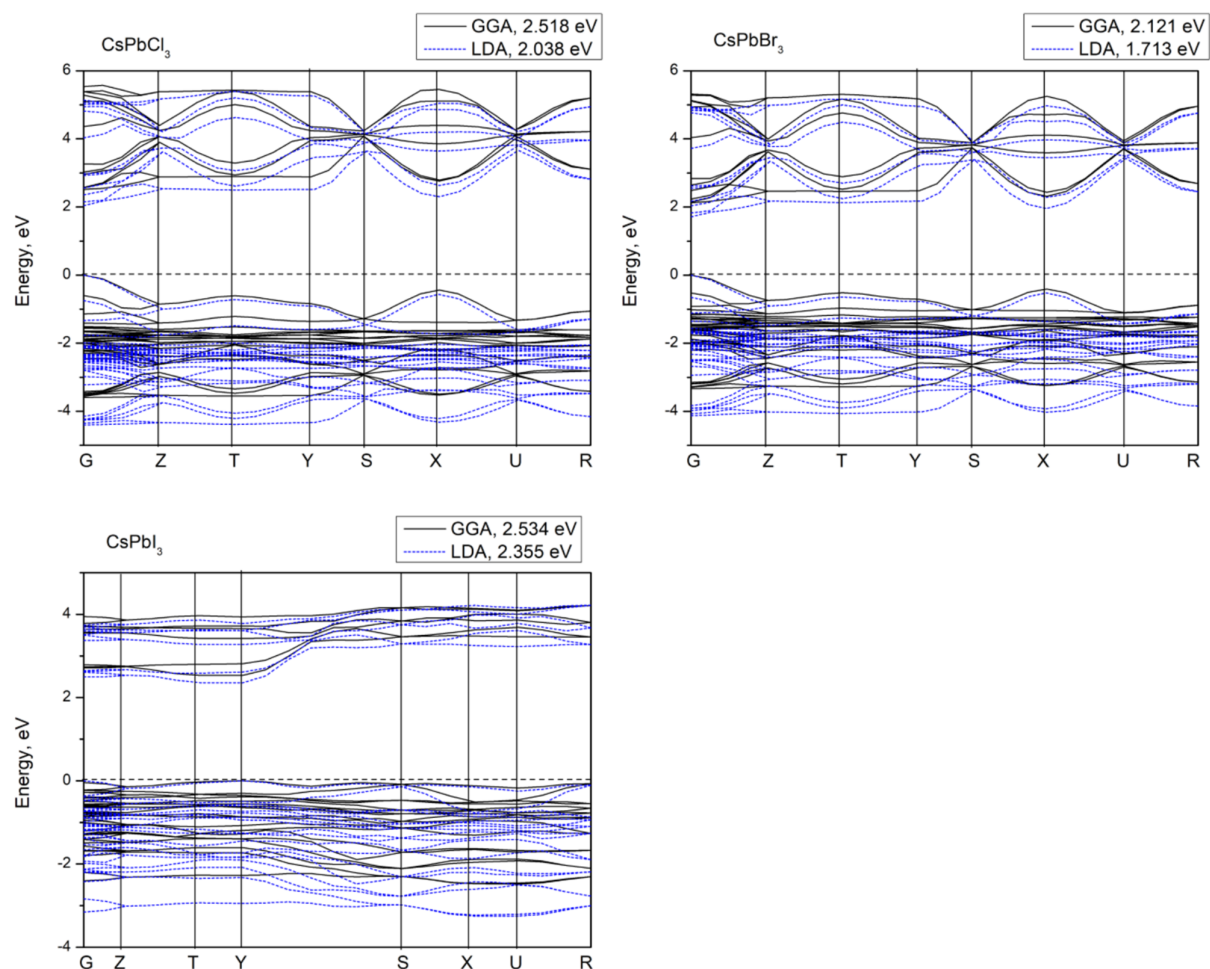


FIG. 9. Calculated band structures of CsPbCl₃, CsPbBr₃, and CsPbI₃. The GGA- and LDA-calculated results are shown by the solid and dashed lines, respectively. The calculated bandgaps are given at the top of each diagram. The coordinates of the special points of the Brillouin zone are (in the units of the reciprocal lattice unit vectors) G(0, 0, 0); Z(0, 0, 1/2); T(-1/2, 0, 1/2); Y(-1/2, 0, 0); S(-1/2, 1/2, 0); and X(0, 1/2, 0), U(0, 1/2, 1/2), R(-1/2, 1/2, 1/2).

the band-to-band absorption can be associated with the 6s-6p Pb excitation. It can also be noticed that the VB in CsPbI₃ is somewhat narrower than in two other halides. The overall pattern of the Cs and Pb states in all three crystals is practically the same. The Cs 5s states appear as a sharp maximum at around -21 eV, and the Cs 5p states produce the lower VB at about -7.5 eV. The lead 5d states are located at about -16 eV. The 3s, 4s, and 5s states of the Cl, Br, and I ions, respectively, move slightly closer to the upper VB bottom. The DOS diagrams and bands assignment for CsPbCl₃ and CsPbBr₃ agree well with the data from Ref. 49. It should be emphasized that most of the first-principles calculations for the title compounds were made for their cubic phase, e.g., Refs. 17, 40, and 43 and, therefore, cannot be compared directly with the current results. A few data available on the experimental

and calculated band structures of orthorhombic CsPbI₃ are collected in Table 1.

The calculated unpolarized dielectric functions for CsPbCl₃, CsPbBr₃, and CsPbI₃ are shown in Fig. 11 (see the supplementary material for details on how to calculate them). The values of $\text{Re}(\epsilon)$ in the limit of infinite wavelength determine the refractive index of a solid $n = \sqrt{\text{Re}(\epsilon)}$. Since the studied crystals are all orthorhombic, they should be optically anisotropic, as is evidenced by the data in Table S3 that collects the calculated in the present work $\text{Re}(\epsilon)$ values along the crystallographic axis with other data available in the literature.

For the relevant equations for the estimation of the effective masses of electrons and holes (m_e^* , m_h^*), the exciton

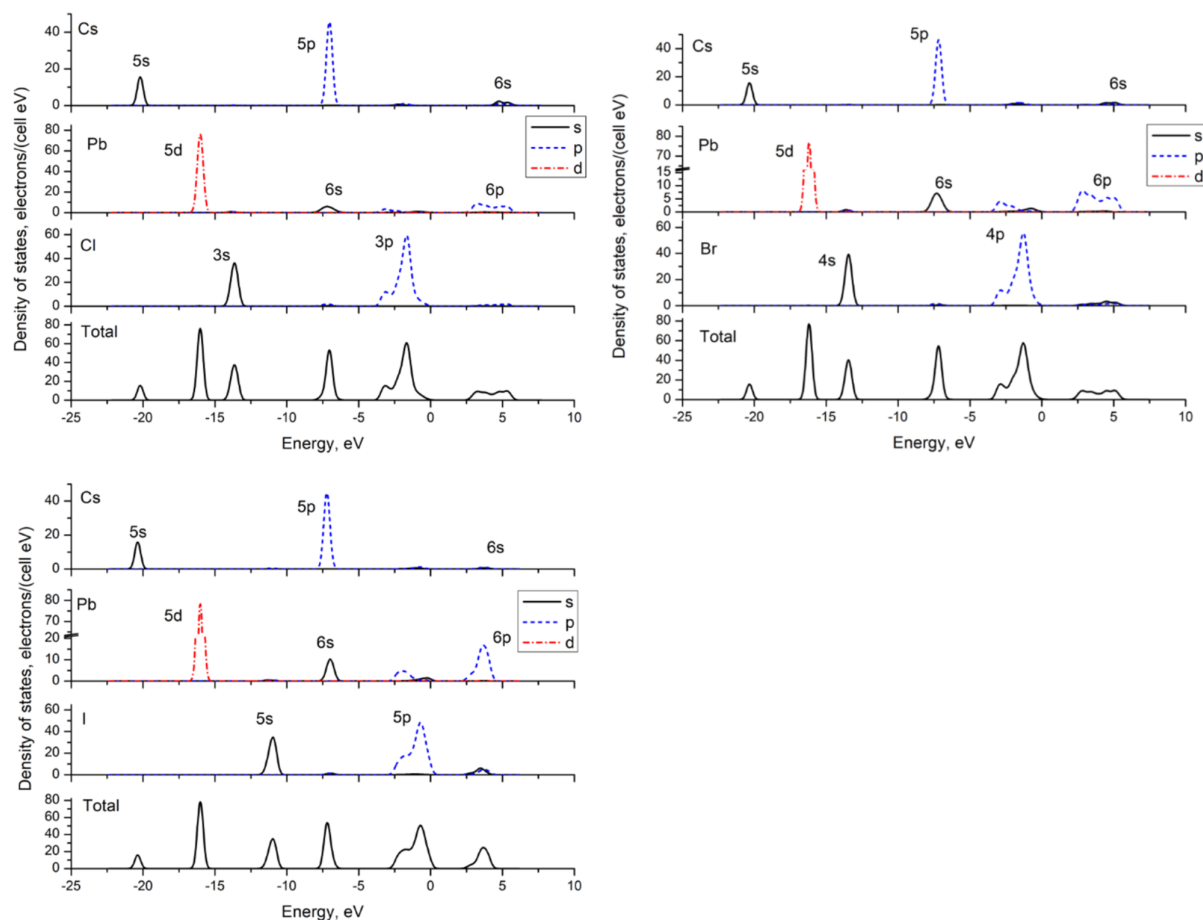


FIG. 10. Calculated density of states (DOS) diagrams for CsPbCl₃, CsPbBr₃, and CsPbI₃.

diameter a_0 and the exciton binding energy E_b see the [supplementary material](#).

The results of estimations of all these parameters for the studied halides are collected in [Table II](#). Some indirect comparison can be made with the data obtained in [Ref. 17](#), but it should be kept in mind that those results were obtained for the cubic modifications of these halides. The band structures calculated in that reference are very similar to each other and exhibit strong dispersion around the VB maxima and CB minima. This is not the case for the orthorhombic phases, especially for CsPbI₃, where the VB top is remarkably flat, which leads to very high values of the hole effective mass.

TABLE I. Calculated and experimental bandgaps for CsPbI₃.

	Expt.		Calculated	
Bandgap (eV)	3.17	2.534, 2.355	2.54	2.29
References	50	This work	45	28

A large difference between the effective masses of the electrons and holes in CsPbI₃ can be attributed to very contrast behavior of the electronic states at the VB top and the CB bottom ([Fig. 9](#)): it is easy to see that the curvatures of those states are quite different and so are the corresponding effective masses.

Synthesized colloidal nanocrystals of CsPbBr₃ were characterized by XRPD, steady state, and time resolved PL and TEM. XRPD confirms their orthorhombic structure. Under UV excitation, the nanocrystals exhibit ultrafast blue subnanosecond emission due to strong quantum confinement effects or green emission (somewhat longer than a nanosecond) depending on the particle size. The green emission of larger nanocrystals can be suppressed by slowing down the reaction and agglomeration rate. Drop-casted blue emitting film shows the presence of nanoplatelets with a width of 2-3 monolayers. Its PL spectrum composed of several bands confirms the presence of nanoplatelets consisting of different numbers of monolayers. The fastest PL decay is below

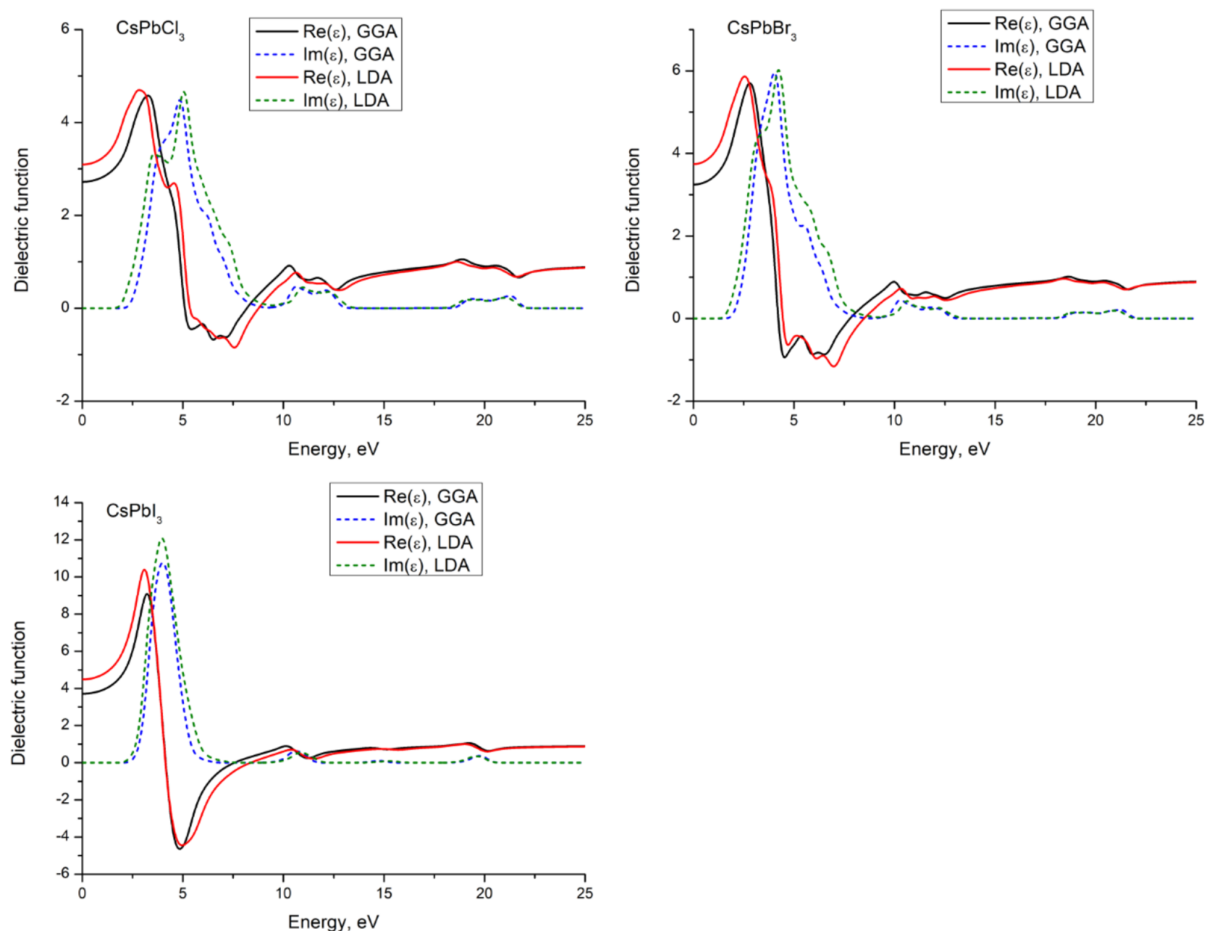


FIG. 11. Calculated dielectric function for CsPbCl₃, CsPbBr₃, and CsPbI₃.

1 ns. To test the applicability of prepared nanoplatelets, they were embedded in the polystyrene matrix. The subnanosecond blue emission in this nanocomposite can be preserved

provided the sample is not exposed to the UV/vis light and/or high temperatures. Such emission makes the CsPbBr₃ nanocomposite material further combined with a classical

TABLE II. Calculated effective masses of the holes and electrons (in the units of the electron mass) and Wannier-Mott exciton parameters for CsPbCl₃, CsPbBr₃, and CsPbI₃.

	CsPbCl ₃			CsPbBr ₃			CsPbI ₃		
	GGA	LDA	Calc. ^a	GGA	LDA	Calc. ^a	GGA	LDA	Calc. ^a
m_h^*	0.10	0.09	0.17	0.12	0.10	0.14	1.4	1.1	0.13
m_e^*	0.23	0.19	0.20	0.26	0.23	0.15	0.08 ^b	0.08 ^b	0.11
ϵ_∞^c	2.723	3.09	4.07	3.247	3.74	4.96	3.72	4.49	6.32
a_0 (Å)	41	55	50	42	55	70	48	58	120
E_b (meV)	130	85	75	106	70	40	80	55	12

^aReference 17, for the cubic phase.

^bEstimations of the m_e^* were performed for the Y-S path (Fig. 9), where dispersion of the electronic states is the strongest.

^c ϵ_∞ denotes the dielectric constant value in the limit of infinite wavelengths.

heavy scintillator with the high light yield, such as LYSO:Ce, a promising candidate for building up the time-of-flight positron emission tomography (TOF-PET) detector.

Detailed consideration of the structural properties of CsPbX₃ halides (X = Cl, Br, I) revealed an important difference among these materials: the PbCl₆ and PbBr₆ octahedra are connected by vertices, whereas the Pbl₆ octahedra are isolated from each other. In addition, the local symmetry of the halide octahedra around the Pb ions decreases with increased halide atomic number. The optimized unit cells and all their structural characteristics agreed well with the experimental XRD data. The calculated band structures show all compounds to be direct bandgap materials although an indirect bandgap transitions at the same energy can be realized in CsPbCl₃ and CsPbBr₃ since the conduction bands minima at two different points of the Brillouin zone are practically equal in these compounds. The effective masses of the electrons for the lowest states in the conduction band and holes for the highest states in the valence bands were performed. It was shown that the effective masses of holes in CsPbI₃ are very large because the top of the valence band in this halide is nearly flat. We believe that the isolated character of the Pbl₆ octahedra may be behind a low hole's mobility in CsPbI₃.

In addition to the calculations of the structural, electronic, and optical properties of these three halide materials, we estimated the effective exciton diameter and exciton binding energy. The exciton diameter increases and the binding energy decreases with increasing halide atomic number.

See [supplementary material](#) for details on synthesis, absorption spectrum of colloidal nanoplatelets, computational methods, and additional data on structural calculations.

This work was carried out in the frame of Crystal Clear Collaboration and has been supported by the Czech Science Foundation, Grant No. GA17-06479S, the Ministry of Education Youth and Sports, project "Center for advanced applied science," No. CZ.02.1.01/0.0/0.0/16_019/0000778, Cost Action TD1401, ERC advanced Grant TICAL (No. 338953), and H2020 Twinning project ASCIMAT (No. 690599). M.G.B. thanks the financial support from the project MOBILITY FZU from Operational Programme: Research, Development and Education, MEYS, No. CZ.02.2.69/0.0/0.0/16_027/0008215, Recruitment Program of High-end Foreign Experts (Grant No. GDW20145200225), the Programme for the Foreign Experts offered by Chongqing University of Posts and Telecommunications, Estonian Research Council Grant PUT PRG111, and European Regional Development Fund (No. TK141). Dr. G. A. Kumar (University of Texas at San Antonio) is thanked for allowing use Materials Studio. Dr. A. Khan and Professor Dr. I. Moreels are thanked for advising us on the embedding procedure in the polystyrene.

REFERENCES

- R. Hofstadter, *Phys. Rev.* **75**, 796 (1949).
- C. W. E. Van Eijk, *Phys. Med. Biol.* **47**, R85 (2002).
- C. W. E. Van Eijk, *Nucl. Instrum. Methods Phys. Res., Sect. A* **509**, 17 (2003).
- P. Lecoq, *Nucl. Instrum. Methods Phys. Res., Sect. A* **809**, 130 (2016).
- C. Ronda, H. Wiecek, V. Khanin, and P. Rodnyi, *ECS J. Solid State Sci. Technol.* **5**, R3121 (2016).
- M. Salomoni, R. Potts, E. Auffray, and P. Lecoq, *Crystals* **8**, 78 (2018).
- J. S. Karp, S. Surti, M. E. Daube-Witherspoon, and G. Muehllehner, *J. Nucl. Med.* **49**, 462 (2008).
- T. Jones and D. Townsend, *J. Med. Imaging* **4**, 011013 (2017).
- S. Gundacker, F. Acerbi, E. Auffray, A. Ferri, A. Gola, M. V. Nemallapudi, G. Paternoster, C. Piemonte, and P. Lecoq, *J. Instrum.* **11**, P08008 (2016).
- N. Aubry, E. Auffray, F. B. Mimoun, N. Brillouet, R. Bugalho, E. Charbon, O. Charles, D. Cortinovis, P. Courday, and A. J. Cserkaszkzy, *J. Instrum.* **8**, C04002 (2013).
- S. Gundacker, "Time resolution in scintillator based detectors for positron emission tomography," Ph.D. thesis, Vienna University of Technology, Wien, Austria, 2014.
- P. Lecoq, E. Auffray, S. Brunner, H. Hillemanns, P. Jarron, A. Knapitsch, T. Meyer, and F. Powolny, *IEEE Trans. Nucl. Sci.* **57**, 2411 (2010).
- P. Lecoq, *IEEE Trans. Radiat. Plasma Med. Sci.* **1**, 473 (2017).
- J. Q. Grim, S. Christodoulou, F. Di Stasio, R. Krahn, R. Cingolani, L. Manna, and I. Moreels, *Nat. Nanotechnol.* **9**, 891 (2014).
- M. M. Lee, J. Teuscher, T. Miyasaka, T. N. Murakami, and H. J. Snaith, *Science* **338**, 643 (2012).
- H.-S. Kim, C.-R. Lee, J.-H. Im, K.-B. Lee, T. Moehl, A. Marchioro, S.-J. Moon, R. Humphry-Baker, J.-H. Yum, J. E. Moser, M. Grätzel, and N.-G. Park, *Sci. Rep.* **2**, 591 (2012).
- L. Protesescu, S. Yakunin, M. I. Bodnarchuk, F. Krieg, R. Caputo, C. H. Hendon, R. X. Yang, A. Walsh, and M. V. Kovalenko, *Nano Lett.* **15**, 3692 (2015).
- X. Li, Y. Wu, S. Zhang, B. Cai, Y. Gu, J. Song, and H. Zeng, *Adv. Funct. Mater.* **26**, 2435 (2016).
- Y. Bekenstein, B. A. Koscher, S. W. Eaton, P. Yang, and A. P. Alivisatos, *J. Am. Chem. Soc.* **137**, 16008 (2015).
- Z. Liu, J. A. Peters, C. C. Stoumpos, M. Sebastian, B. W. Wessels, J. Im, A. J. Freeman, and M. G. Kanatzidis, *Proc. SPIE* **8852**, 88520A (2013).
- C. C. Stoumpos, C. D. Malliakas, J. A. Peters, Z. Liu, M. Sebastian, J. Im, T. C. Chasapis, A. C. Wibowo, D. Y. Chung, A. J. Freeman, B. W. Wessels, and M. G. Kanatzidis, *Cryst. Growth Des.* **13**, 2722 (2013).
- C. K. Møller, *Nature* **182**, 1436 (1958).
- M. Natarajan and B. Prakash, *Phys. Status Solidi A* **4**, K167 (1971).
- S. Hirotsu, J. Harada, M. Iizumi, and K. Gesi, *J. Phys. Soc. Jpn.* **37**, 1393 (1974).
- J. Hutton, R. J. Nelves, G. M. Meyer, and V. R. Eiriksson, *J. Phys. C: Solid State Phys.* **12**, 5393 (1979).
- S. Sharma, N. Weiden, and A. Weiss, *Z. Phys. Chem.* **175**, 63 (1992).
- D. M. Trots and S. V. Myagkota, *J. Phys. Chem. Solids* **69**, 2520 (2008).
- C. C. Stoumpos, C. D. Malliakas, and M. D. Kanatzidis, *Inorg. Chem.* **52**, 9019 (2013).
- S. Plesko, R. Kind, and J. Roos, *J. Phys. Soc. Jpn.* **45**, 553 (1978).
- I. P. Pashuk, N. S. Pidzyrailo, and M. G. Matsko, *Fiz. Tverd. Tela* **23**, 2162 (1981).
- K. Nitsch, V. Hamplová, M. Nikl, K. Polák, and M. Rodová, *Chem. Phys. Lett.* **258**, 518 (1996).
- D. Fröhlich, K. Heidrich, H. Künzel, G. Trendel, and J. Treusch, *J. Lumin.* **18-19**, 385 (1979).
- M. Nikl, K. Nitsch, K. Polak, G. P. Pazzi, P. Fabeni, D. S. Citrin, and M. Gurioli, *Phys. Rev. B* **51**, 5192 (1995).
- M. Nikl, K. Nitsch, E. Mihóková, K. Polák, P. Fabeni, G. P. Pazzi, and M. Gurioli, *Physica E* **4**, 323 (1999).
- V. Babin, P. Fabeni, M. Nikl, K. Nitsch, G. P. Pazzi, and S. Zazubovich, *Phys. Status Solidi B* **226**, 419 (2001).
- A. Swarnkar, R. Chulliyil, V. K. Ravi, M. Irfanullah, A. Chowdhury, and A. Nag, *Angew. Chem., Int. Ed.* **127**, 15644 (2015).
- D. Zhang, S. W. Eaton, Y. Yu, L. Dou, and P. Yang, *J. Am. Chem. Soc.* **137**, 9230 (2015).

- ³⁸D. Zhang, Y. Yang, Y. Bekenstein, Y. Yu, N. A. Gibson, A. B. Wong, S. W. Eaton, N. Kornienko, Q. Kong, M. Lai, A. P. Alivisatos, S. R. Leone, and P. Yang, *J. Am. Chem. Soc.* **138**, 7236 (2016).
- ³⁹P. Cottingham and R. L. Brutchey, *Chem. Commun.* **52**, 5246 (2016).
- ⁴⁰M. A. Ghebouli, B. Ghebouli, and M. Fatmi, *Physica B* **406**, 1837 (2011).
- ⁴¹J. Brgoch, A. J. Lehner, M. Chabinyk, and R. Seshadri, *J. Phys. Chem. C* **118**, 27721 (2014).
- ⁴²J. Even, L. Pedesseau, J.-M. Jancu, and C. Katan, *J. Phys. Chem. Lett.* **4**, 2999 (2013).
- ⁴³G. Moschou, A. Koliogiorgos, and I. Galanakis, *Phys. Status Solidi A* **215**, 1700941 (2018).
- ⁴⁴S. X. Tao, X. Cao, and P. A. Bobbert, *Sci. Rep.* **7**, 14386 (2017).
- ⁴⁵Y. Huang, W.-J. Yin, and Y. He, *J. Phys. Chem. C* **122**, 1345 (2018).
- ⁴⁶J. Kang and L.-W. Wang, *J. Phys. Chem. Lett.* **8**, 489 (2017).
- ⁴⁷M. Sebastian, J. A. Peters, C. C. Stoumpos, J. Im, S. S. Kostina, Z. Liu, M. G. Kanatzidis, A. J. Freeman, and B. W. Wessels, *Phys. Rev. B* **92**, 235210 (2015).
- ⁴⁸K. Momma and F. Izumi, *J. Appl. Crystallogr.* **44**, 1272 (2011).
- ⁴⁹K. Heidrich, W. Schäfer, M. Schreiber, J. Söchtig, G. Trendel, J. Treusch, T. Grandke, and H. J. Stolz, *Phys. Rev. B* **24**, 5642 (1981).
- ⁵⁰O. N. Yunakova, V. K. Miloslavskii, and E. N. Kovalenko, *Opt. Spectrosc.* **112**, 91 (2012).

CsPbBr₃ Thin Films on LYSO:Ce Substrates

Kateřina Tomanová¹, Adéla Suchá, Eva Mihóková², Lenka Procházková, Ivo Jakubec, Rosana M. Turtos, Stefan Gundacker, Etienne Auffray, and Václav Čuba

Abstract—We fabricate thin films of lead halide perovskite nanocrystals on glass substrates and cerium-doped LYSO substrates (lutetium-yttrium oxyorthosilicate, Lu_xY_{2-x}SiO₅:Ce) using spin-coating and drop-casting methods, respectively. We study their structural and optical properties. The luminescence and scintillation are monitored in both steady-state and time-resolved regimes. We focus on the possibility to exploit these structures in designing a detection system with ultrafast time resolution.

Index Terms—Fast timing, luminescence, nanocrystals, perovskites, scintillators, thin films.

I. INTRODUCTION

LEAD halide perovskite quantum dots (QDs) with chemical formula CsPbX₃ (X = Cl, Br, and I) were first reported in bulk CsX crystals doped by Pb²⁺ [1]–[3]. To the best of our knowledge, not much investigation was carried out on this material after that, until 2015, when Protesescu *et al.* [4] developed a synthetic method for obtaining colloidal CsPbX₃ nanocrystals. Consequently, an enormous increase in attention to this type of nanomaterial was initiated and it became an immediate success in the field of photovoltaics (the photovoltaic cell efficiency was increased from ~6% for CsPbBr₃ [5] to ~17% for iodides [6] in just three years).

Nevertheless, photovoltaics is not the only field of interest in these QDs. Among applications in displays as well as in LEDs [7] and lasing [8], their potential as scintillators has also been thoroughly studied [9], [10]. Thanks to their excellent luminescent properties (high light yield, narrow emission

bands, and fast response [4], [10]), CsPbX₃ nanocrystals are currently among the top candidates for future fast detector development for time-of-flight positron-emission tomography (TOF PET) or high-energy physics [11].

New concepts of the fast detector buildup [12] are, among other possibilities, considering replacing the usual bulk scintillator pixel by a hybrid structure combining the standard dense scintillator with an ultrafast nanoscintillator. In this configuration, the recoil electron from a photoelectric conversion created in the dense scintillator can eventually reach an ultrafast emitting layer composed of nanoscintillators [13]. The fast material is driving the timing improvements, and the heavy/standard scintillator provides the stopping power and energy resolution [14].

To follow this concept, the colloidal solution of nanoparticles first needs to be processed. One possibility is to cast the nanocrystals as a thin film on a standard heavy scintillator substrate. lutetium-yttrium oxyorthosilicate (LYSO):Ce is a well-established bright scintillator with general formula Lu_xY_{2-x}SiO₅:Ce³⁺ that is already in use in commercial PET scanners [15]. The CdSe-based semiconductor nanoplatelets drop-casted on LYSO:Ce have been shown to achieve 80-ps coincidence time resolution on a hybrid functional pixel [14].

In this article, we fabricated CsPbBr₃ thin films on small cerium-doped LYSO substrates using a drop-casting method. We characterized the films with main focus on their luminescent properties including the decay kinetics. To demonstrate the applicability of thin films on a larger scale as well as to provide a thin film on a nonscintillating material for at least a qualitative comparison, we demonstrated a spin-coating technique on larger glass substrates. The spin-coating technique can be upscaled to substrates up to 20 cm in diameter in our setup.

II. MATERIALS AND METHODS

A. Chemicals

The following chemicals were used for the preparation of CsPbBr₃ nanocrystals: CsBr (99.999%, Sigma-Aldrich), PbBr₂ (99.999%, Sigma-Aldrich), *N,N*-dimethylformamide (DMF, anhydrous, 99.8%, Sigma-Aldrich), oleic acid (OA, 99%, Sigma-Aldrich), oleylamine (OAm, 70%, Sigma-Aldrich), and toluene (anhydrous, 99.8%, Sigma-Aldrich). All chemicals were used as received without further purification.

B. Thin-Film Substrates

The glass substrate was a glass slide for microscopy (18 mm × 18 mm × 0.17 mm, Hirschmann). The LYSO:Ce was purchased from Crystal Photonics Inc., and the substrate had dimensions 3 mm × 3 mm × 0.2 mm.

Manuscript received January 27, 2020; accepted February 28, 2020. Date of publication March 5, 2020; date of current version June 19, 2020. This work was supported in part by the Crystal Clear Collaboration, in part by the Czech Science Foundation under Grant GA20-06374S, in part by the Ministry of Education Youth and Sports through the Project “Center for Advanced Applied Science,” under Grant CZ.02.1.01/0.0/0.0/16_019/0000778, and in part by the Grant Agency of the Czech Technical University in Prague, under Grant SGS17/195/OHK4/3T/14.

Kateřina Tomanová, Eva Mihóková, and Lenka Procházková are with the Faculty of Nuclear Sciences and Physical Engineering, Czech Technical University (CTU) in Prague, 11519 Prague, Czech Republic, and also with the Institute of Physics of the Czech Academy of Sciences, 16253 Prague, Czech Republic (e-mail: katerina.tomanova@jfifi.cvut.cz).

Adéla Suchá and Václav Čuba are with the Faculty of Nuclear Sciences and Physical Engineering, Czech Technical University (CTU) in Prague, 11519 Prague, Czech Republic.

Ivo Jakubec is with the Institute of Inorganic Chemistry of the AS CR, 25068 Husinec, Czech Republic.

Rosana M. Turtos and Etienne Auffray are with CERN, 1211 Meyrin, Switzerland.

Stefan Gundacker is with CERN, 1211 Meyring, Switzerland, and also with the Dipartimento di Fisica “Giuseppe Occhialini”, University of Milano-Bicocca (UniMiB), 20126 Milan, Italy.

Color versions of one or more of the figures in this article are available online at <http://ieeexplore.ieee.org>.

Digital Object Identifier 10.1109/TNS.2020.2978581

0018-9499 © 2020 IEEE. Personal use is permitted, but republication/redistribution requires IEEE permission. See <https://www.ieee.org/publications/rights/index.html> for more information.

C. CsPbBr₃ Preparation

The nanocrystals were synthesized by the supersaturated recrystallization method at room temperature and air atmosphere, as presented by Li *et al.* [16]. In short, 0.4 mmol of PbBr₂ and 0.4 mmol of CsBr were dissolved in 10 mL of DMF, and after the addition of 1 mL of OA and 0.5 mL of OAm, 4 mL of the solution was quickly added to 40 mL of toluene. The precipitated material was collected by centrifugation for future processing and characterization. The supernatant was characterized immediately after the synthesis as well for comparison.

D. Thin-Film Fabrication

The precipitate after centrifugation was dispersed in a small amount of toluene and was spin-coated on a glass slide using a WS-650MZ-23NPPB-UD3 spincoater (Laurell) or drop-casted on a small LYSO:Ce plate. The static spin-coating method at 4000 rpm and the volume of 100 μ L of the toluene dispersion was used to fabricate one layer of perovskite nanocrystals on the glass substrate. To fabricate more layers, the static method was repeated. The volume used for the drop-casting method on the smaller LYSO:Ce plate was 3 μ L. All the abovementioned procedures were carried out at room temperature and atmospheric pressure at air atmosphere. The resulting thin films were stored in a desiccator filled with silica gel. Over the course of one week, we did not observe either any changes in luminescence or increase in mass under these storage conditions.

E. Characterization

X-ray powder diffraction (XRPD) was measured using a Rigaku Miniflex 600 diffractometer equipped with a Cu X-ray tube (average wavelength $K_{\alpha 1,2}$ 0.15418 nm, voltage 40 kV, and current 15 mA). Data were collected with a speed of 2°/min and compared with the ICDD PDF-2 database, version 2013. The transmission electron microscopy (TEM) was obtained using an EM201 microscope (Philips). The radioluminescence (RL) and photoluminescence (PL) spectra were collected using a 5000M spectrofluorimeter (Horiba Jobin Yvon) with a monochromator and a TBX-04 photodetector. The excitation source for RL measurements was the Seifert X-ray tube (40 kV and 15 mA). The following excitation sources were used for PL measurements: deuterium lamp [results displayed in Fig. 1(a)] and laser-driven Xe pressure lamp, EQ-99XFC Laser-Driven Light Source (LDLS) (used for other PL measurements). The time-resolved PL spectra were obtained under laser excitation (PiLAS, 372 nm) using the Hamamatsu C10910 streak camera with 18-ps time resolution for detection. The RL decay measurements were performed in the time-correlated single-photon counting regime using a pulsed tungsten X-ray tube and a fast hybrid photomultiplier tube (PMT) from Becker & Hickl with a full-width at half-maximum (FWHM) of around 55 ps. Photons were integrated over the filter spectral range 514.5 nm \pm 10 nm with no further discrimination. The impulse-response function (IRF) of the whole setup (laser + X-ray tube + photodetector + electronic

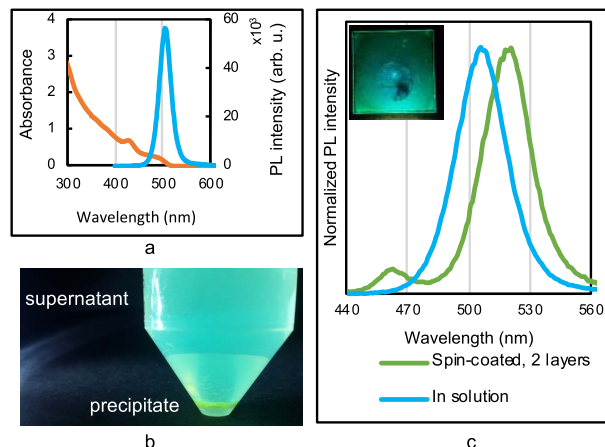


Fig. 1. (a) Absorption (orange) and PL (blue) spectra of the separated supernatant (300 nm excitation). (b) Photograph under UV excitation (365 nm) light of the supernatant and the precipitate right after the centrifugation. (c) PL spectrum (300-nm excitation) of thin film spin-coated on the glass substrate (15 mm \times 15 mm \times 0.17 mm, green line) in comparison with the PL spectrum of the supernatant (blue line). The inset in (c) is the photograph of the spin-coated thin film on the glass substrate under UV excitation (365 nm).

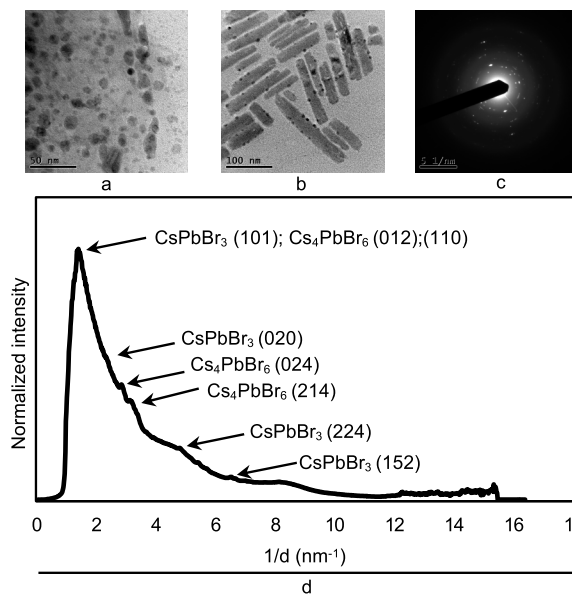


Fig. 2. TEM images of (a) supernatant and (b) precipitate [see Fig. 1(b)]. (c) SAED image of the area in (b). (d) Analysis of the SAED using the ICDD PDF-2 database (version 2013). The SAED was analyzed with the help of the ProcessDiffraction software [18].

readout) was obtained by means of intraband luminescence present in Li₂MoO₂ crystals with a final FWHM of around 130 ps. For more details, please refer to [17].

III. RESULTS AND DISCUSSION

The precipitated material in toluene was centrifuged and then the precipitate (solid phase) and the supernatant (liquid phase) were characterized separately (see Section II). Fig. 1(b) shows a photograph taken under 365-nm UV excitation of

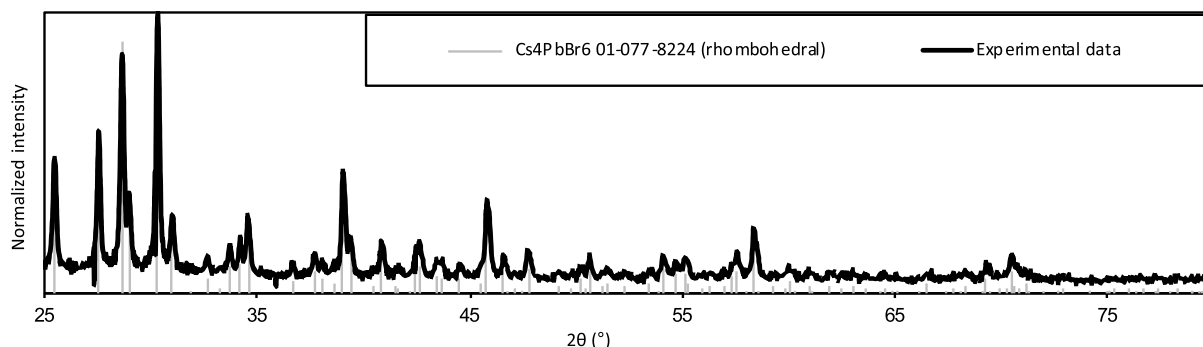


Fig. 3. XRPD pattern of the solid precipitated material separated by centrifugation. The material was compared with the rhombohedral Cs₄PbBr₆ phase from the ICDD PDF-2 database.

those two phases immediately after centrifugation. Note that the luminescence of the supernatant is turquoise, while the precipitate emits green light. The blue-shift of the supernatant emission is caused by the quantum confinement effect in the remaining nanocrystals that are significantly smaller than the precipitated ones and, therefore, could not be centrifuged completely. Unfortunately, the supernatant could not be used for the fabrication of the blue-emitting thin films as the concentration of the nanocrystals there was too low.

The concentration of the nanocrystals in the supernatant could be increased by solvent evaporation or centrifugation, but the nanocrystals tend to agglomerate fast at higher concentration, which results in a red-shift of both the absorption and luminescence spectra to the green spectral region. See [10] for more details.

Another evidence of the bimodal size distribution can be seen in the TEM images [Fig. 2(a) and (b)]. Fig. 2(a) shows the TEM image of the supernatant containing spherical QDs of the size of roughly about 10 nm, and Fig. 2(b) shows the TEM image of the precipitate containing large nanoplatelets up to 40-nm thick with various lengths up to 200 nm with some of the spherical QDs from the supernatant attached to their surface.

To investigate the crystal structure of those nanocrystals, we analyzed the selected area electron diffraction (SAED) presented in Fig. 2(c) of the area shown in Fig. 2(b) using the ProcessDiffraction software [18]. Despite the high background, the plot shows several peaks that we compared with the ICDD PDF-2 database (version 2013). They can be attributed to both CsPbBr₃ and Cs₄PbBr₆ phases [see Fig. 2(d)].

The XRPD analysis of the separated precipitated solid phase after centrifugation (Fig. 3) confirms only the presence of the Cs₄PbBr₆ nanocrystals. We assume that the reason why the CsPbBr₃ phase is not observable in this diffraction pattern is that the QDs are too small and their amount in the precipitate is too low, falling below the detection limit of the method.

The presence of CsPbBr₃ nanocrystals is further evidenced by the optical properties (see Fig. 1). The bandgap of the Cs₄PbBr₆ bulk crystal is ~3.7 eV [19], [20], and therefore, any excitonic emission in the visible spectral region must be

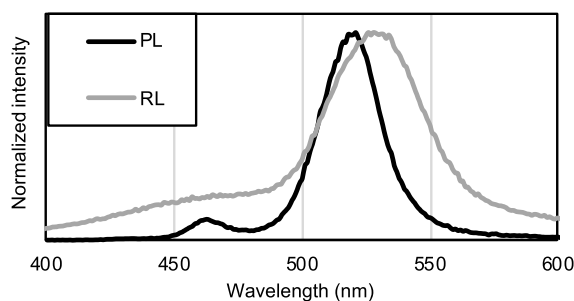


Fig. 4. Normalized RL and PL [as in Fig. 1(c)] spectra of thin film casted on the glass substrate (15 mm × 15 mm × 0.17 mm) using a spin-coating technique (five layers).

attributed to the CsPbBr₃ phase or the CsPbBr₃-like aggregates as studied in [2]. This phase can be present either as the QDs on the surface of Cs₄PbBr₆ [as in Fig. 2(b), with the corresponding SAED analysis in Fig. 2(c) and (d)], or as the nanocrystals embedded inside the Cs₄PbBr₆ crystals as in [21].

The good spectral overlap of the Cs₄PbBr₆ emission (emission band centered at 375 nm [19], [22]) and CsPbBr₃ absorption [absorption edge at around 500 nm; see Fig. 1(a)] suggests that the efficient energy transfer between the phases can be expected. Further investigation of this phenomenon is required for better understanding of the luminescent properties of this family of scintillators. However, it is not trivial to synthesize either the pure CsPbBr₃ phase or the pure Cs₄PbBr₆ by the supersaturation precipitation method used in this work to allow a thorough comparison of their decay profiles.

The PL spectrum of the supernatant in Fig. 1(a) shows a narrow excitonic emission band centered at 506 nm. It is blue-shifted compared with the bulk emission (540 nm [23]), which confirms the presence of quantum-confined CsPbBr₃ nanocrystals. The Stokes shift of this material is rather small, but we did not expect serious issues with self-absorption, as we were producing thin films in this preliminary study to test the system performance. However, the practical applications of this system would require thicker films, where the self-absorption would become more significant. To overcome this issue, future efforts may be concentrated on dispersing the nanocrystals in a suitable matrix.

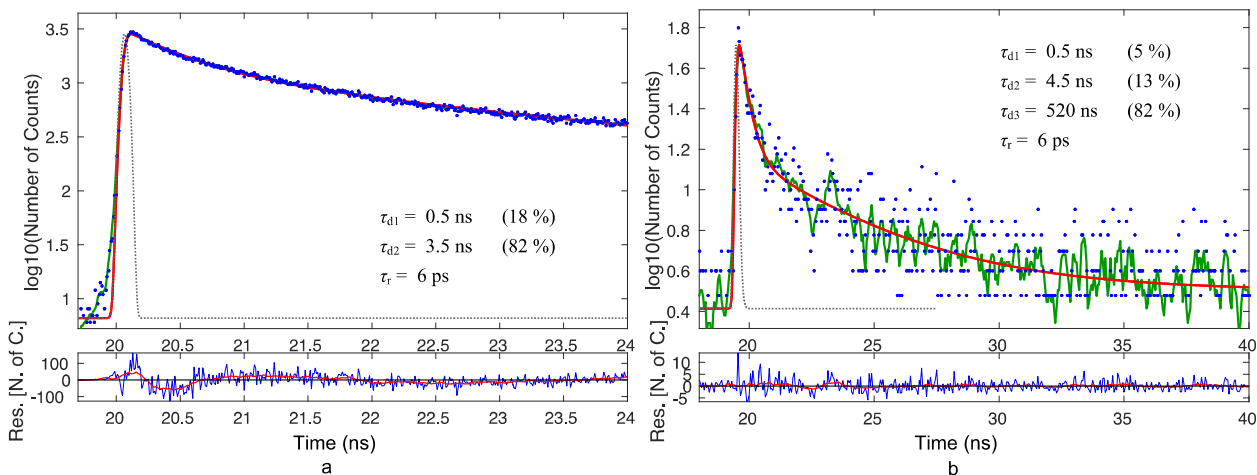


Fig. 5. (a) PL (laser excitation, 372 nm) and (b) RL decay curves of the thin film on the glass substrate consisting of five spin-coated layers. Blue dots are experimental data, the red line is the two (three)-exponential fit with the rise time τ_r and decay-time τ_d components reported in the figure, the green line is a moving average of the experimental data, and the black dotted line is representing the IRF of the whole detection system.

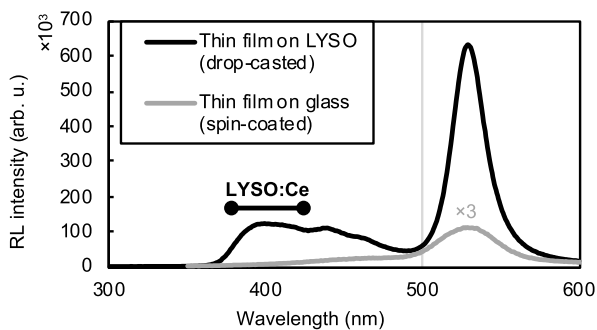


Fig. 6. RL of the thin film on the LYSO:Ce substrate (drop-casted) compared with the thin film on glass (spin-coated, five layers).

A. Thin Films on the Glass Substrate

By dispersing the precipitated solid phase separated by centrifugation in a small amount of toluene, we obtained a concentrated suspension that could be used for a thin-film fabrication. In Fig. 1(c), we present a PL spectrum of such a thin film on the glass substrate in comparison with the PL spectrum of the supernatant [as presented in Fig. 1(a)]. The emission spectrum of the supernatant (smaller nanoparticles) is blue-shifted compared with the thin film fabricated using the precipitate (larger nanoparticles). This is further evidence of the bimodal size distribution in the as-prepared samples.

The interesting feature in Fig. 1(c) is the presence of weak emission band in the spectrum of thin film in the blue spectral region that is not present in the spectrum of supernatant. We assume that, in solution, the emission originated in the fraction of the smallest nanocrystals is reabsorbed by larger nanocrystals (such a mechanism was suggested to explain the PL properties of the colloidal carbon QDs [24]). This emission is, therefore, observable only in the thin film where such reabsorption is much less likely.

Fig. 4 shows the normalized RL spectrum of the thin film consisting of five layers spin-coated on a glass substrate in comparison with the normalized PL spectrum presented in Fig. 1(c). The overall shape of the spectra, namely, the presence of two emission bands in the blue and green spectral regions, is similar, except for the red-shift of the RL spectrum with respect to the PL spectrum.

The red-shift of the RL spectrum is most likely due to a different excitation mechanism of RL with respect to that of PL. Larger particles emitting in longer wavelengths with respect to smaller ones can be more preferably excited. Furthermore, some degree of reabsorption of the light emitted by smaller particles by larger ones can also contribute to the observed red-shift. The broadening of the RL spectrum is caused by a larger slit on the emission monochromator used for the RL measurement with respect to the PL measurement.

The PL and RL decays of five spin-coated layers on the glass substrate are displayed in Fig. 5. The fast subnanosecond component is present in both cases (unfortunately it is the weakest component). The PL decay time analysis in the 100-ns window showed the presence of a long tail with the decay time value around 100 ns (not presented). The scintillation decay features a very long tail with the decay time of 520 ns. However, as the light output of the samples is still rather low (and, therefore, the dynamic range of the decay curves is poor), future experiments are required for more accurate scintillation decay profile analysis.

B. Thin Films on the Scintillating LYSO:Ce Substrate

The LYSO:Ce substrate was chosen because of its high light yield and high stopping power for ionizing radiation. The position of the emission band of LYSO:Ce does not overlap with the emission band of the CsPbBr₃ nanocrystals. This allows distinguishing the emissions from both materials in order to investigate the optical properties in more detail.

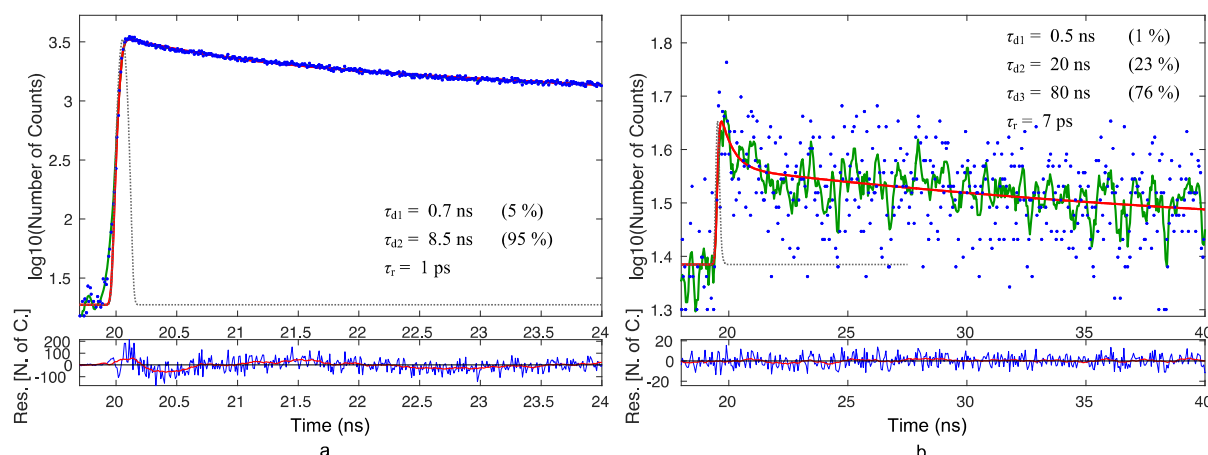


Fig. 7. (a) PL (laser excitation, 372 nm) and (b) RL decay curves of the thin film drop-casted on the LYSO:Ce substrate. Blue dots are experimental data, the red line is the two (three)-exponential fit with the rise time τ_r and decay time τ_d components reported in the figure, the green line is a moving average of the experimental data, and the black dotted line is representing the IRF of the whole detection system.

The thin films on the LYSO:Ce substrates were fabricated using a drop-casting method, because the size of the substrate (3 mm × 3 mm × 0.2 mm) did not allow the usage of the spin-coating technique.

Fig. 6 shows the qualitative comparison of the RL spectra of the drop-casted film on LYSO:Ce and the spin-coated film on glass. Quantitative comparison of the light output cannot be made due to the different size and nature of the samples (i.e., different thicknesses of the thin films that were prepared by different casting methods on the substrates of different sizes using different amounts of nanocrystals). Note that most of the light emitted from the thin film drop-casted on LYSO:Ce is in the green region, i.e., by the CsPbBr₃ nanocrystals.

The red-shift of the RL spectrum compared with that of PL, probably due to some self-absorption as seen in Fig. 4, was observed also on the thin film on the LYSO:Ce substrate (PL spectrum was not presented, and emission maximum was at 521 nm compared with that of 530 nm in the RL spectrum).

The timing performance analysis is summarized in Fig. 7. The subnanosecond component is present in both cases. The PL decay curve in the 100-ns window showed again the long tail of ~100-ns decay time (not presented) that is also present in the scintillation decay profile of the drop-casted film on LYSO:Ce. Nevertheless, the contribution of the fast decay (τ_{d1}) is rather weak compared with that of τ_{d2} (which is possibly attributed to LYSO:Ce), in contrast to a much stronger CsPbBr₃ RL with respect to that of LYSO:Ce in Fig. 6. This is likely due to some reabsorption of LYSO:Ce emitted light by CsPbBr₃. However, as mentioned above, the dynamic range of the timing measurement [Fig. 7(b)] is rather poor and future investigation of better quality samples is required.

IV. CONCLUSION

We fabricated thin films of lead bromide perovskites on LYSO:Ce substrates and studied their characteristics with a perspective of their usage in fast timing applications. Thin films casted on glass substrates were also studied to provide

some qualitative comparison. The ultrafast subnanosecond decay component of the perovskites is preserved in both PL and RL decays of the thin films. Its contribution is rather weak; however, future improvement on the quality of thin films and scintillation yield is expected.

Preliminary results presented definitely show a potential of hybrid structures made of lead halide perovskite nanocrystals combined with classical heavy scintillators to build up a fast detection system. Compared with the currently used detectors, while LYSO:Ce provides the stopping power and energy resolution, the halide perovskite part would improve the timing characteristics. Such detection systems of a new generation are paving the way to achieve ultimately real-time imaging in PET.

REFERENCES

- [1] M. Nikl *et al.*, "Optical properties of the Pb²⁺-based aggregated phase in a CsCl host crystal: Quantum-confinement effects," *Phys. Rev. B, Condens. Matter*, vol. 51, no. 8, pp. 5192–5199, Feb. 1995.
- [2] M. Nikl *et al.*, "Luminescence of CsPbBr₃-like quantum dots in CsBr single crystals," *Phys. E: Low-Dimensional Syst. Nanostruct.*, vol. 4, no. 4, pp. 323–331, Oct. 1999.
- [3] V. Babin, P. Fabeni, M. Nikl, K. Nitsch, G. P. Pazzi, and S. Zazubovich, "Luminescent CsPbI₃ and Cs₄PbI₆ aggregates in annealed CsI:Pb crystals," *Phys. Status Solidi (B)*, vol. 226, no. 2, pp. 419–428, Aug. 2001.
- [4] L. Protesescu *et al.*, "Nanocrystals of cesium lead halide perovskites (CsPbX₃, X = Cl, Br, and I): Novel optoelectronic materials showing bright emission with wide color gamut," *Nano Lett.*, vol. 15, no. 6, pp. 3692–3696, Jun. 2015.
- [5] M. Kulbak, D. Cahen, and G. Hodes, "How important is the organic part of lead halide perovskite photovoltaic cells? Efficient CsPbBr₃ cells," *J. Phys. Chem. Lett.*, vol. 6, no. 13, pp. 2452–2456, Jun. 2015.
- [6] Y. Wang, T. Zhang, M. Kan, and Y. Zhao, "Bifunctional stabilization of all-inorganic α -CsPbI₃ perovskite for 17% efficiency photovoltaics," *J. Amer. Chem. Soc.*, vol. 140, no. 39, pp. 12345–12348, Sep. 2018.
- [7] J. Song, J. Li, X. Li, L. Xu, Y. Dong, and H. Zeng, "Quantum dot light-emitting diodes based on inorganic perovskite cesium lead halides (CsPbX₃)," *Adv. Mater.*, vol. 27, no. 44, pp. 7162–7167, Nov. 2015.
- [8] Y. Chen, M. Yu, S. Ye, J. Song, and J. Qu, "All-inorganic CsPbBr₃ perovskite quantum dots embedded in dual-mesoporous silica with moisture resistance for two-photon-pumped plasmonic nanolasers," *Nanoscale*, vol. 10, no. 14, pp. 6704–6711, 2018.

- [9] Q. Chen *et al.*, "All-inorganic perovskite nanocrystal scintillators," *Nature*, vol. 561, no. 7721, pp. 88–93, Sep. 2018.
- [10] K. Tomanová *et al.*, "On the structure, synthesis, and characterization of ultrafast blue-emitting CsPbBr₃ nanoplatelets," *APL Mater.*, vol. 7, no. 1, Jan. 2019, Art. no. 011104.
- [11] C. Dujardin *et al.*, "Needs, trends, and advances in inorganic scintillators," *IEEE Trans. Nucl. Sci.*, vol. 65, no. 8, pp. 1977–1997, Aug. 2018.
- [12] P. Lecoq, "Pushing the limits in time-of-flight PET imaging," *IEEE Trans. Radiat. Plasma Med. Sci.*, vol. 1, no. 6, pp. 473–485, Nov. 2017.
- [13] R. M. Turtos, S. Gundacker, E. Auffray, and P. Lecoq, "Towards a metamaterial approach for fast timing in PET: Experimental proof-of-concept," *Phys. Med. Biol.*, vol. 64, no. 18, 2019, Art. no. 185018.
- [14] R. M. Turtos *et al.*, "On the use of CdSe scintillating nanoplatelets as time taggers for high-energy gamma detection," *npj 2D Mater. Appl.*, vol. 3, p. 37, Oct. 2019.
- [15] S. Surti, A. Kuhn, M. E. Werner, A. E. Perkins, J. Kolthammer, and J. S. Karp, "Performance of philips gemini TF PET/CT scanner with special consideration for its time-of-flight imaging capabilities," *J. Nucl. Med.*, vol. 48, no. 3, pp. 471–480, Mar. 2007.
- [16] X. Li *et al.*, "CsPbX₃ quantum dots for lighting and displays: Room-temperature synthesis, photoluminescence superiorities, underlying origins and white light-emitting diodes," *Adv. Funct. Mater.*, vol. 26, no. 15, pp. 2435–2445, Feb. 2016.
- [17] R. M. Turtos, S. Gundacker, S. Omelkov, E. Auffray, and P. Lecoq, "Light yield of scintillating nanocrystals under X-ray and electron excitation," *J. Lumin.*, vol. 215, Nov. 2019, Art. no. 116613.
- [18] J. L. Lábár, "Consistent indexing of a (set of) single crystal SAED pattern(s) with the processdiffraction program," *Ultramicroscopy*, vol. 103, no. 3, pp. 237–249, Jun. 2005.
- [19] L. N. Quan *et al.*, "Highly emissive green perovskite nanocrystals in a solid state crystalline matrix," *Adv. Mater.*, vol. 29, no. 21, Jun. 2017, Art. no. 1605945.
- [20] S. Kondo, K. Amaya, and T. Saito, "Localized optical absorption in Cs₄PbBr₆," *J. Phys., Condens. Matter*, vol. 14, no. 8, pp. 2093–2099, Mar. 2002.
- [21] J. Xu *et al.*, "Imbedded nanocrystals of CsPbBr₃ in Cs₄PbBr₆: Kinetics, enhanced oscillator strength, and application in light-emitting diodes," *Adv. Mater.*, vol. 29, no. 43, Nov. 2017, Art. no. 1703703.
- [22] M. Nikl *et al.*, "Photoluminescence of Cs₄PbBr₆ crystals and thin films," *Chem. Phys. Lett.*, vol. 306, nos. 5–6, pp. 280–284, Jun. 1999.
- [23] C. C. Stoumpos *et al.*, "Crystal growth of the perovskite semiconductor CsPbBr₃: A new material for high-energy radiation detection," *Cryst. Growth Des.*, vol. 13, no. 7, pp. 2722–2727, Jul. 2013.
- [24] W. Zhang, D. Dai, X. Chen, X. Guo, and J. Fan, "Red shift in the photoluminescence of colloidal carbon quantum dots induced by photon reabsorption," *Appl. Phys. Lett.*, vol. 104, no. 9, Mar. 2014, Art. no. 091902.

Article

On the Role of Cs₄PbBr₆ Phase in the Luminescence Performance of Bright CsPbBr₃ Nanocrystals

Kateřina Děcká ^{1,2,*}, Adéla Suchá ¹, Jan Král ¹, Ivo Jakubec ³, Martin Nikl ², Vítězslav Jarý ², Vladimír Babin ², Eva Mihóková ² and Václav Čuba ¹

¹ Department of Nuclear Chemistry, Faculty of Nuclear Sciences and Physical Engineering, Czech Technical University in Prague, Břehová 7, 115 19 Prague, Czech Republic; suchaade@jfifi.cvut.cz (A.S.); kralja13@jfifi.cvut.cz (J.K.); vaclav.cuba@jfifi.cvut.cz (V.Č.)

² Institute of Physics, Czech Academy of Sciences, Cukrovarnická 10, 162 00 Prague, Czech Republic; nikl@fzu.cz (M.N.); jary@fzu.cz (V.J.); babinv@fzu.cz (V.B.); mihokova@fzu.cz (E.M.)

³ Institute of Inorganic Chemistry, Czech Academy of Sciences, Husinec-Řež č.p. 1001, 250 68 Řež, Czech Republic; jakubec@iic.cas.cz

* Correspondence: Katerina.Decka@jfifi.cvut.cz

Abstract: CsPbBr₃ nanocrystals have been identified as a highly promising material for various optoelectronic applications. However, they tend to coexist with Cs₄PbBr₆ phase when the reaction conditions are not controlled carefully. It is therefore imperative to understand how the presence of this phase affects the luminescence performance of CsPbBr₃ nanocrystals. We synthesized a mixed CsPbBr₃-Cs₄PbBr₆ sample, and compared its photo- and radioluminescence properties, including timing characteristics, to the performance of pure CsPbBr₃ nanocrystals. The possibility of energy transfer between the two phases was also explored. We demonstrated that the presence of Cs₄PbBr₆ causes significant drop in radioluminescence intensity of CsPbBr₃ nanocrystals, which can limit possible future applications of Cs₄PbBr₆-CsPbBr₃ mixtures or composites as scintillation detectors.

Keywords: nanocrystals; lead halide perovskites; luminescence; scintillation detectors



Citation: Děcká, K.; Suchá, A.; Král, J.; Jakubec, I.; Nikl, M.; Jarý, V.; Babin, V.; Mihóková, E.; Čuba, V. On the Role of Cs₄PbBr₆ Phase in the Luminescence Performance of Bright CsPbBr₃ Nanocrystals. *Nanomaterials* **2021**, *11*, 1935. <https://doi.org/10.3390/nano11081935>

Academic Editor: Ashish Arora

Received: 2 July 2021

Accepted: 22 July 2021

Published: 27 July 2021

Publisher's Note: MDPI stays neutral with regard to jurisdictional claims in published maps and institutional affiliations.



Copyright: © 2021 by the authors. Licensee MDPI, Basel, Switzerland. This article is an open access article distributed under the terms and conditions of the Creative Commons Attribution (CC BY) license (<https://creativecommons.org/licenses/by/4.0/>).

1. Introduction

Cesium lead halide perovskite quantum dots of the CsPbX₃ (X = Cl, Br, I) formula have been first identified by Nikl et al. group as nano-inclusions in CsX host doped by Pb²⁺ ions [1–3]. However, they have not been studied extensively since the introduction of their colloidal synthesis in 2015 [4]. They were immediately identified as highly promising materials for various applications, mostly for solar cells [5], LEDs [6], or displays [7]. Their excellent luminescent properties, such as high quantum efficiency, narrow emission lines, and fast decay times, are also highly desirable for scintillator manufacture. Recently, a body of studies on the lead halide perovskites has also been focused on their application in X-ray detection [8–14].

Nevertheless, this material also has some drawbacks; in particular its poor chemical stability on air [15,16]. An obvious solution would be provided by encapsulation of CsPbX₃ in various inert matrices such as SiO₂ [17–19], TiO₂ [20], or organic polymers [8,21,22]. Many studies also proposed an interesting composite material CsPbBr₃@Cs₄PbBr₆ which, besides enhanced stability, also passivates CsPbBr₃ nanocrystals, i.e., suppresses non-radiative recombinations on surface defects [23–25]. Various CsPbBr₃-Cs₄PbBr₆ mixtures in the form of two different nanocrystal population were also prepared [26,27].

Cs₄PbBr₆ is a material often referred to as a “zero-dimensional perovskite”, while CsPbBr₃ is called a “three-dimensional perovskite”. CsPbBr₃ consists of corner sharing PbBr₆⁴⁻ octahedra, whereas in Cs₄PbBr₆ those octahedra are isolated (see Figure S1 in Supplementary Information). Cs₄PbBr₆ continues to be somewhat controversial material; there is still an ongoing debate on whether or not it is a source of bright green luminescence

and, if so, what the origin of that luminescence is [28]. There is also a question how the presence of Cs_4PbBr_6 affects the luminescent properties of CsPbBr_3 and vice versa.

The debate was initiated by some early reports on pure Cs_4PbBr_6 crystals with superior green luminescence without any profound considerations about the origin of such luminescence [29,30]. The origin of the green luminescence was questioned, and two major opinions appeared in research community; one strong opinion is that CsPbBr_3 nanoinclusions are, in fact, present in Cs_4PbBr_6 crystals [25,31–33], as the bright green emission is associated with CsPbBr_3 nanocrystals. It has already been stated in 1999 by Nikl et al. that it is difficult to suppress the presence of CsPbBr_3 in Cs_4PbBr_6 completely [34]. This point of view is further supported by many studies on non-luminescent Cs_4PbBr_6 that can be easily transformed into bright CsPbBr_3 [35–39].

The other strong opinion proposes that the green luminescence is due to point defects in Cs_4PbBr_6 structure. Some possible defects that may cause green luminescence were identified, for example the Br vacancy [40–42]. For more details, please refer to review papers published on this subject, for example the most recent, [28], which supports the opinion based on the presence of nanoinclusions, and provides persuasive arguments rebutting the Br vacancy concept.

Understanding of the role of CsPbBr_3 and Cs_4PbBr_6 phases in the luminescence of cesium lead bromides is particularly important when considering applications and future needs to scale-up the production for manufacturing. CsPbBr_3 nanocrystals have been recently identified as highly prospective scintillators for applications requiring fast response, for example a new generation of time-of-flight positron emission tomographs (TOF-PET), or new detectors for high energy physics [43,44]. However, these considerations are important regardless the target application. It is clear that CsPbBr_3 and Cs_4PbBr_6 phases tend to coexist. Therefore, it is evident that this tendency may become a serious issue in a scale-up of the synthesis for industrial production. In order to manufacture a material of the best performance, it is imperative to know how detrimental a contamination of CsPbBr_3 nanocrystals by Cs_4PbBr_6 phase can be, if at all. There have already been some arguments raised in the recent literature against the possible applicability of $\text{CsPbBr}_3@ \text{Cs}_4\text{PbBr}_6$ composite as a scintillator [45].

The band gap energy of Cs_4PbBr_6 and CsPbBr_3 was calculated to be 3.9 eV and 2.3 eV, respectively [46]. This allows an energy transfer from Cs_4PbBr_6 to CsPbBr_3 . This transfer can be both radiative and/or non-radiative. Excitation in Cs_4PbBr_6 phase results in formation of self-trapped excitons that radiatively recombine while emitting UV photons. This emission can radiatively excite CsPbBr_3 . The band alignment in the core-shell structure $\text{CsPbBr}_3@ \text{Cs}_4\text{PbBr}_6$ is of the type I, which means that the valence band maximum and the conduction band minimum are fully within the Cs_4PbBr_6 band gap. This also allows a non-radiative energy transfer from Cs_4PbBr_6 to CsPbBr_3 by hopping [46].

However, when the energy transfer does not occur, the presence of Cs_4PbBr_6 may hinder the luminescence from CsPbBr_3 . In a theoretical model of 80 nm slab of CsPbBr_3 below 10 μm of $\text{CsPbBr}_3@ \text{Cs}_4\text{PbBr}_6$ composite, the escaping emission spectrum was calculated to be $100\times$ attenuated compared to the launched spectrum from the CsPbBr_3 slab [38]. The attenuation coefficient of Cs_4PbBr_6 is higher than that of CsPbBr_3 [47], therefore the incident energy will be preferably deposited in the Cs_4PbBr_6 phase.

This study intends to contribute to an intense and important debate about the CsPbBr_3 vs. Cs_4PbBr_6 issue, and also to shed some light on the (radio)luminescence properties of CsPbBr_3 and Cs_4PbBr_6 mixtures, which should help to better understand the dynamics of the abovementioned $\text{CsPbBr}_3@ \text{Cs}_4\text{PbBr}_6$ composite and its applicability in the field of scintillation detectors. In particular, analysis of radioluminescence decays of our materials might provide a valuable set of data on the light and/or energy transfer between the two phases. We reiterate that, unlike rather extended literature on PL properties of materials in question, data on scintillation properties, especially scintillation decays, are scarce.

We synthesized CsPbBr_3 nanocrystals using the hot injection method (HI) [4] and their mixture with Cs_4PbBr_6 crystals using the room-temperature precipitation method

(RTP) [48]. The RTP method is, by its nature (simple mixing of two solutions without any heating), the best candidate for potential scaling up. The HI is the most widely used method, which proves its robustness and reproducibility. We found out that the HI method usually leads to high quality pure CsPbBr₃ nanocrystals, while RTP protocol resulted in various CsPbBr₃-Cs₄PbBr₆ mixtures. We studied and compared luminescent properties of all samples in detail (both photoluminescence and radioluminescence, including decay kinetics) with respect to their composition, structure, and morphology. We found out that the presence of Cs₄PbBr₆ phase significantly deteriorates CsPbBr₃ scintillation light output, which can limit the application potential of CsPbBr₃-Cs₄PbBr₆ mixtures as scintillation detectors.

2. Materials and Methods

2.1. Chemicals

This study utilizes the following chemicals: CsBr (99.999%, Merck, Darmstadt, Germany), PbBr₂ (99.999%, Merck, Darmstadt, Germany), Cs₂CO₃ (99.9%, Merck, Darmstadt, Germany), oleylamine (OAm, 70%, Merck, Darmstadt, Germany), oleic acid (OA, 90%, Merck, Darmstadt, Germany), 1-octadecene (90%, Merck, Darmstadt, Germany), n-hexane (anhydrous, 98%, Merck, Darmstadt, Germany), toluene (99.8%, Merck, Darmstadt, Germany), and *N,N*-dimethylformamide (DMF, anhydrous, 99.8%, Merck, Darmstadt, Germany). All chemicals were used as received, without further purification, unless stated otherwise.

2.2. Hot Injection (HI) Synthesis of Pure CsPbBr₃

The procedure introduced by Protesescu et al. was used [4]. In short, 0.752 mmol of PbBr₂, 20 mL of 1-octadecene (ODE), 2 mL of oleylamine (OAm), and 1.78 mL of oleic acid (OA), were mixed in 100 mL 3-necked flask and degassed at 110 °C under vacuum for 1 h. After that, 0.5 mL of dried pre-synthesized cesium oleate solution (0.4 M) was injected at 170 °C under argon atmosphere. Solid product was separated from ODE solution by centrifugation and redispersed in hexane. For narrowing the size distribution and enhancing colloidal stability, one more centrifugation step was performed, and the supernatant was collected.

The synthesis of cesium oleate was modified according to the study by Lu [49], which provides a complete conversion of cesium salt to cesium oleate, resulting in better reproducibility of synthesis, and in complete solubility of cesium oleate at room temperature by reacting 5 molar equivalents of oleic acid with respect to Cs. The amount of OA added during the CsPbBr₃ synthesis was adjusted to match the molar ratios from [4].

For more details on both syntheses, please refer to Supplementary Information.

2.3. Room-Temperature Precipitation (RTP) Synthesis of CsPbBr₃-Cs₄PbBr₆ Mixture

The procedure introduced by Li et al. [48] as supersaturation recrystallization (currently called room-temperature precipitation) was used with slight modifications for better reproducibility. In short, 0.4 mmol of PbBr₂ and 0.4 mmol of CsBr were dissolved in 10 mL of dimethylformamide (DMF) and 1 mL of OA and 0.5 mL of OAm were added. Then, 1 mL of the solution was quickly added to 10 mL of toluene. Solid product was collected by centrifugation, both the supernatant and the precipitate were characterized. For more details, please refer to Supplementary Information.

2.4. Characterization

X-ray powder diffraction (XRPD) was measured using a Rigaku Miniflex 600 diffractometer equipped with the Cu X-ray tube (average wavelength $K_{\alpha 1,2}$ 0.15418 nm, voltage 40 kV, current 15 mA). Data were collected with a speed of 2°/min and compared with the ICDD PDF-2 database, version 2013. The transmission electron microscopy (TEM) was obtained using an EM201 microscope (Philips, Amsterdam, Netherlands). Absorption spectra were collected using a Cary 100 spectrophotometer (Varian, Palo Alto, CA, USA).

Photoluminescence (PL) excitation and emission spectra were collected using a FluoroMax spectrofluorometer (Horiba Jobin Yvon, Kyoto, Japan). Radioluminescence (RL) spectra were collected using a 5000 M spectrofluorometer (Horiba Jobin Yvon, Kyoto, Japan) with a monochromator and TBX-04 (IBH Scotland, Glasgow, Scotland) photodetector, the excitation source was a Seifert X-ray tube (40 kV, 15 mA). Spectrofluorometer 5000 M (Horiba Jobin Yvon, Kyoto, Japan) was used for measuring PL decay curves using the pulsed nanoLED sources (IBH Scotland, Glasgow, Scotland, excitation wavelengths 310 nm and 389 nm, 80 kHz repetition rate) as the excitation sources. The detection part of the setup involved a single-grating monochromator and a photon counting detector TBX-04 (IBH Scotland, Glasgow, Scotland). RL decay curves were collected using hybrid picosecond photon detector HPPD-860 and Fluorohub unit (Horiba Scientific, Kyoto, Japan). Decays were recorded in both the long and short time windows, as the short time window is relevant for the fast timing applications. Samples were excited by picosecond (ps) X-ray tube N5084 from Hamamatsu, operating at 40 kV. The X-ray tube was driven by the ps light pulser (Hamamatsu, Hamamatsu City, Japan) equipped with a laser diode operating at 405 nm. The instrumental response function FWHM of the setup is about 76 ps. Convolution procedure was applied to all decay curves to determine true decay times (SpectraSolve software package, Ames Photonics, Hurst, TX, USA). The contribution of a component expressed as a percentage (often referred to as a light sum, LS) was calculated as:

$$LS_n = \frac{A_n \tau_n}{\sum A_i \tau_i}$$

where A_n and τ_n denotes amplitude and decay time of the nth component.

XRPD, RL spectra, and RL/PL decays were measured on solid samples, i.e., precipitates after the first centrifugation step. In case of supernatant of sample prepared by RTP, XRPD was measured on drop-casted film. Samples for TEM characterization were obtained by drop-casting the final toluene/hexane solutions on TEM grid. Absorption and PL excitation/emission spectra were also collected on final toluene/hexane solutions.

3. Results and Discussion

XRPD patterns of all samples are presented in Figure 1 and compared to ICDD PDF-2 database records for orthorhombic CsPbBr₃ (#01-072-7929) and rhombohedral Cs₄PbBr₆ (#01-077-8224) phases. The sample prepared by the hot injection (HI) method (red line) was identified as pure CsPbBr₃ sample. The diffraction lines are significantly broadened, suggesting that this phase consists of very small crystallites. Halder–Wagner method of determining linear size of crystallites (using Scherrer constant value 0.94) revealed their mean size as (13 ± 1) nm. A slightly elevated background under 40°, suggesting the presence of an amorphous phase, can be attributed to a small excess of organic ligands (oleic acid and oleylamine) present in the measured sample.

Two diffractograms were recorded for the sample prepared by the room-temperature precipitation method (RTP); precipitated solid sample (green line in Figure 1) and supernatant from centrifugation (blue line). The pattern of the precipitate shows only the presence of Cs₄PbBr₆ phase and elevated background under 40° (i.e., an amorphous phase is present). A higher amount of an amorphous phase suggests a large excess of free organic ligands in this sample. Narrow peaks indicate that this phase has much larger crystallites than those of CsPbBr₃ phase identified in the pure (HI) sample.

To prove the expected presence of CsPbBr₃ nanocrystals in this sample (which was strongly indicated by blue/green luminescence of the sample, see below and also [3,25,31,47]), we also measured a drop-casted film of this sample's supernatant (blue line in Figure 1). Narrow peaks of much lower intensity than in centrifuged sample remain present in this diffractogram. In addition, two broad peaks are present at around 15° and 30° (indicated by red stars). Detailed analysis revealed that the first peak can be attributed to two CsPbBr₃ diffractions from (002) and (110) lattice planes, and the second peak can be attributed to CsPbBr₃ diffractions from (004) and (220) lattice planes. This clearly indicates prefer-

ential orientation of nanocrystalline phase in this direction, suggesting the presence of nanoplatelets. As we have demonstrated, this type of synthesis is indeed capable of producing CsPbBr₃ nanoplatelets in the supernatant [50]. Nevertheless, Figure 1 still provides only a partial evidence of the CsPbBr₃ nanocrystals present in the centrifuged sample, as there are many CsPbBr₃ diffraction lines missing in the pattern.

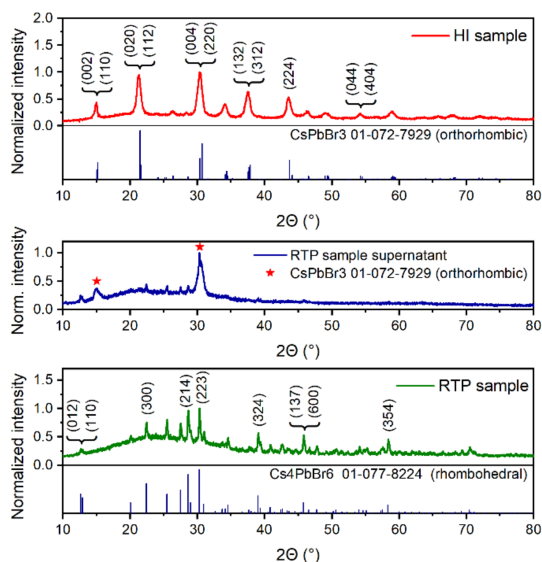


Figure 1. (From top to bottom) XRPD pattern of a precipitate of the sample prepared by the hot injection method (HI, red line) compared to the ICDD PDF-2 database record for CsPbBr₃; XRPD pattern of a supernatant of the sample prepared by the room-temperature precipitation method (RTP, blue line), red stars denote positions of the most intense CsPbBr₃ diffraction double lines; and XRPD pattern of a precipitate of the sample prepared by the RTP method (green line) compared to the ICDD PDF-2 database record for Cs₄PbBr₆.

To provide a stronger evidence of the CsPbBr₃ presence, we performed TEM and analyzed selected area electron diffraction (SAED) patterns of the corresponding micrographs (see Figure 2). TEM in Figure 2a shows that the sample prepared by the HI method (identified by XRPD in Figure 1 as a pure orthorhombic CsPbBr₃ sample with nano-sized crystallites), indeed consists of nanocrystals of cubic shape with the mean size of (19.1 ± 0.2) nm. This value is in good agreement with the calculated mean crystallite size from XRPD pattern in Figure 1. The small discrepancy may be caused by an inaccuracy of determining the FWHM (full width at half maxima) of CsPbBr₃ orthorhombic double peaks and the fact that diffractions at larger angles are partially hidden in the background. TEM in Figure 2b shows that the sample prepared by the RTP method (identified as rhombohedral Cs₄PbBr₆ by XRPD in Figure 1), is clearly a mixture of larger hexagonal crystals (crystal size around 110 nm), and small nanocrystals of roughly cubic shape with the mean size of (9.8 ± 0.2) nm. SAED analysis in Figure 2e–g shows that, in both cases, the cubic nanocrystals can be attributed to the CsPbBr₃ phase, while the hexagonal phase was confirmed as that of Cs₄PbBr₆. We conclude that the sample prepared by RTP method is, in fact, a mixed sample containing both the CsPbBr₃ nanocrystals and the larger Cs₄PbBr₆ crystals.

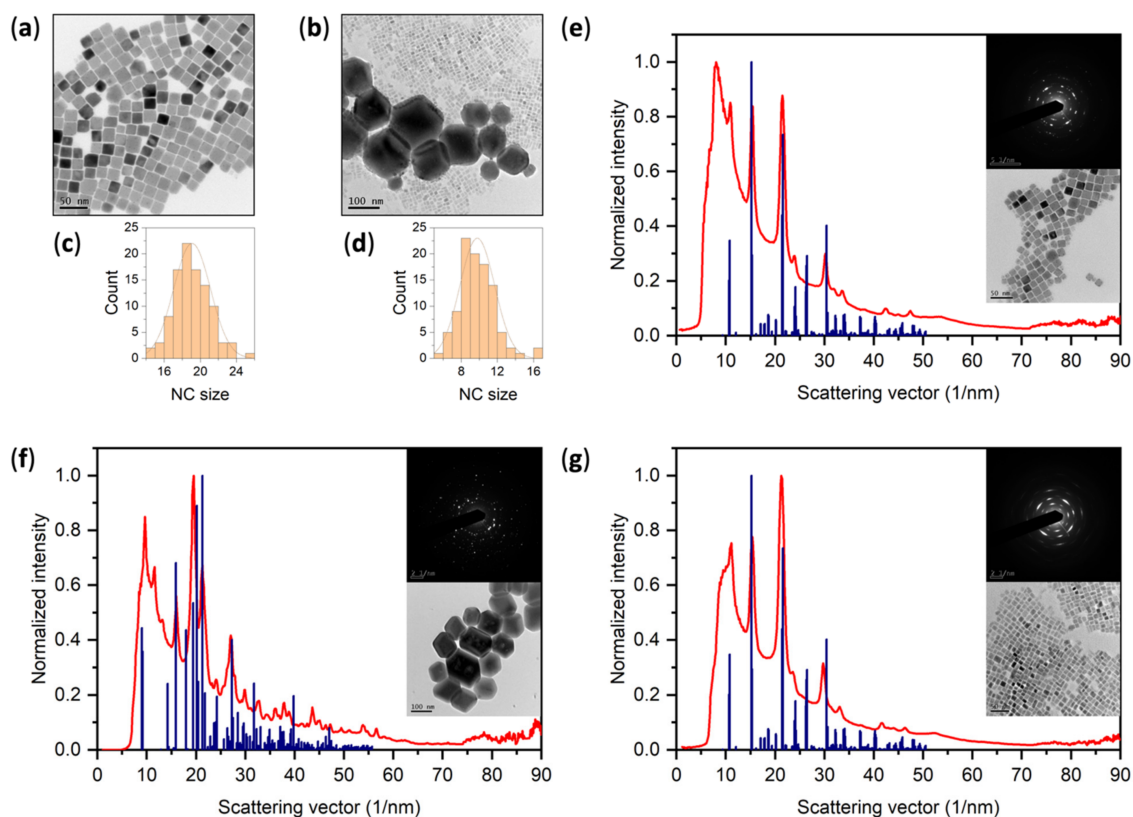


Figure 2. (a) TEM micrograph of the pure sample; (b) TEM micrograph of the mixed sample; (c) size distribution of 100 crystals presented in (a), the mean size is (19.1 ± 0.2) nm; (d) size distribution of 100 crystals presented in (b), the mean size is (9.8 ± 0.2) nm; (e) integrated radial intensity profile from a SAED pattern (in the inset) of the pure sample (corresponding micrograph in the inset) compared to the ICDD PDF-2 record for CsPbBr₃ #01-072-7929; (f) integrated radial intensity profile from a SAED pattern (in the inset) of large hexagonal crystals present in the mixed sample (corresponding micrograph in the inset) compared to the ICDD PDF-2 record for Cs₄PbBr₆ #01-077-8224; and (g) integrated radial intensity profile from a SAED pattern (in the inset) of small cubic crystals present in the mixed sample (corresponding micrograph in the inset) compared to the ICDD PDF-2 record for CsPbBr₃ #01-072-7929. Sizes of nanocrystals were measured using an ImageJ software [51] and SAED patterns were integrated using the ProcessDiffraction software [52].

The reason we cannot see the CsPbBr₃ phase on XRPD clearly (only partially in the supernatant sample) is that Cs₄PbBr₆ crystals are one order of magnitude larger than CsPbBr₃ nanocrystals. In this case, XRPD is not capable of distinguishing the CsPbBr₃ phase present in minority, especially when consisting of smaller particles. We estimate that the amount of CsPbBr₃ phase in this sample was less than 5%. Any reflections from CsPbBr₃ nanocrystals are in this case destined to be lost in the background. CsPbBr₃ reflections were observable only on the supernatant sample, as the majority of large Cs₄PbBr₆ crystals were separated by centrifugation. However, due to the preferential orientation, which resulted from the drop-casting process, this XRPD analysis was not conclusive enough. When in any doubt, it is crucial to exploit more sensitive methods, such as SAED, which was performed in this work, or for example using the synchrotron radiation for XRPD analysis, to avoid any misleading preliminary conclusions.

Based on the XRPD analysis, we denote the HI-prepared sample as “the pure sample” and the RTP-prepared sample as “the mixed sample”.

Absorption spectra of all samples are presented in Figure 3a. Spectrum of pure CsPbBr₃ sample (green line) features typical CsPbBr₃ absorption edge at 515 nm. Absorp-

tion band peaking at 261 nm can be attributed to an excess of surfactants (this peak tends to diminish with lower concentration of nanocrystals, see the Supplementary Information Figure S2 for detailed explanation and additional spectra).

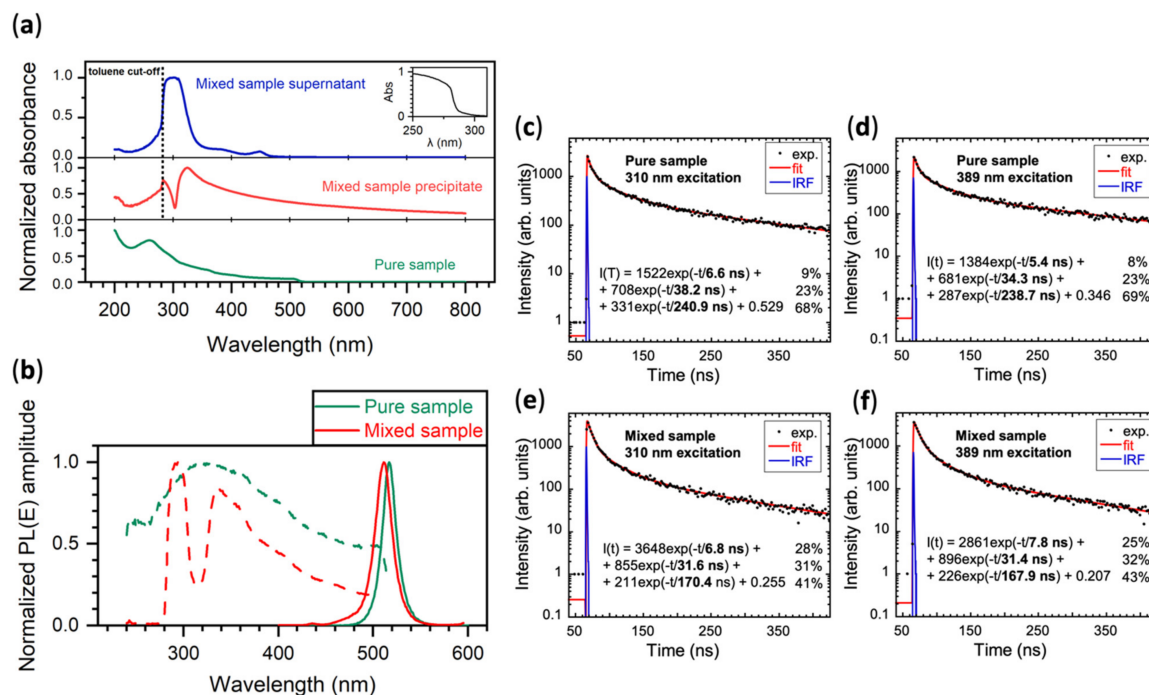


Figure 3. (a) Absorption spectra of both the supernatant (blue line) and precipitate (red line) of the mixed sample (in toluene) and that of the pure sample (green line, in hexane), in the inset: absorption spectrum of toluene; (b) PL characteristics of the pure sample (green lines) and the mixed sample (red lines), excitation spectra, collected at the emission maxima, are in dashed lines, emission spectra in solid lines, excitation wavelength was 300 nm in both cases; and (c–f) PL decay curves of both the pure (c,d) and mixed (e,f) samples, excited at 310 nm (c,e) and 389 nm (d,f). Black dots represent the experimental data, red line is the best fit (3-exponential function), and blue line is the instrumental response function (IRF).

Absorption spectrum of the mixed sample (red line) has a very high background caused by the light scattering at large Cs_4PbBr_6 crystals. We can identify broader absorption band peaking between 305–330 nm, which may be attributed to the bulk absorption of Cs_4PbBr_6 crystals [10,34,53]. Any possible CsPbBr_3 -related absorption edge is hidden in the background. The spectrum rapidly drops down below 283 nm; this is caused by the toluene cut-off (see the toluene absorption spectrum in the inset). The same artefact can be observed in the absorption spectrum of the supernatant of the mixed sample, but not in the spectrum of the pure sample, which is dispersed in hexane.

Absorption spectrum of the supernatant of the mixed sample is presented as a blue line in Figure 3a. This spectrum features two CsPbBr_3 -related absorption maxima at 449 nm and 385 nm, both significantly blue-shifted compared to the absorption of the pure sample. As discussed above (XRPD characterization), CsPbBr_3 nanocrystals present in this sample are probably in the form of nanoplatelets. Strong blue shift of absorption spectrum indicates that at least one dimension is below the exciton Bohr diameter (~4–7 nm) [4,50], which further supports the nanoplatelets hypothesis. Based on this consideration, we may attribute the 385 nm and 449 nm absorption features to the light hole-electron and heavy hole-electron transitions, respectively. Another feature in this spectrum is an absorption at 310 nm, which can be attributed to absorption of Cs_4PbBr_6 crystals [34,54].

Figure 3b shows photoluminescence (PL) emission and excitation spectra of both samples. Spectra of the mixed sample's supernatant are presented in Supplementary

Information Figures S3–S5. Emission maximum of the mixed sample is blue shifted from the maximum of the pure sample by 6 nm, which is caused by the size difference of CsPbBr₃ nanocrystals. Excitation spectrum of the pure sample follows its absorption spectrum up to its maximum at 329 nm. However, excitation spectrum of the mixed sample features a significant drop in its intensity at 314 nm, which matches the Cs₄PbBr₆ absorption (similarly as in [55]).

Cs₄PbBr₆ has larger band gap than CsPbBr₃, therefore an energy transfer is theoretically possible. The drop in the mixed sample excitation spectra does not go all the way to zero intensity, so it does not rule out this possibility as well. We tested the following hypothesis (see Figure 4): Is it possible that the incident radiation excites the Cs₄PbBr₆ phase, and then the energy is either radiatively or non-radiatively transferred to the CsPbBr₃ phase? TEM shows that both phases are in a very close proximity, so both mechanisms are, in principle, possible, even if the radiative transfer has in this case generally much higher probability.

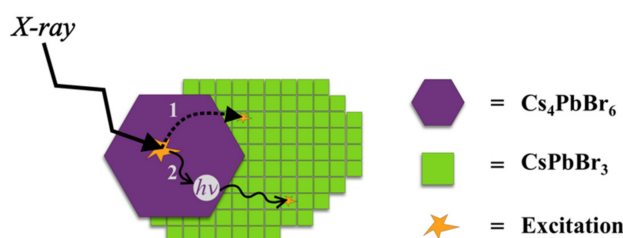


Figure 4. Schematic illustration of the energy-transfer hypothesis; **path 1:** non-radiative energy transfer from Cs₄PbBr₆ excited state to the excited state of neighboring CsPbBr₃ nanocrystal; **path 2:** radiative energy transfer, ultraviolet photon emitted by scintillation process in Cs₄PbBr₆ is absorbed by CsPbBr₃ nanocrystal.

In order to investigate the possible energy transfer between these two phases, we recorded PL decays at two excitation wavelengths for both the pure and the mixed sample. One wavelength (310 nm) was selected to excite mostly the Cs₄PbBr₆ phase, and the second (389 nm) to excite the CsPbBr₃ phase exclusively.

Decay curves of the pure sample are shown in Figure 3c,d. They are almost identical, featuring 6 ns fast decay component. Panels (e) and (f) show decay curves of the mixed sample. Again, they are almost identical, therefore no energy transfer from Cs₄PbBr₆ to CsPbBr₃ was confirmed. Moreover, compared to the pure sample, the fast components are roughly similar, only the slowest component seems to be faster in the mixed sample. Additionally, the contribution of the fastest component is significantly higher in the mixed sample.

This acceleration of the decay time in the mixed sample is probably caused by the presence of smaller CsPbBr₃ nanocrystals. One factor may be the quantum confinement effect, but it can also be caused by the luminescence quenching on various defects. It is well known that, in smaller nanocrystals with higher surface to volume ratio, more surface defects are present, which can be responsible for significant quenching. Nevertheless, the presence of Cs₄PbBr₆ phase seems to have no effect on PL temporal characteristics of the CsPbBr₃ nanocrystals, which might also be due to severe thermal quenching of the emission of the former at room temperature [34].

Due to the nature of the samples, it is challenging to guarantee the same concentration of the solid phase in both mixed and pure samples to reliably assess the quantitative effect of the Cs₄PbBr₆ presence on the CsPbBr₃ PL intensity. This is also the reason we present only normalized (to a maximum) PL spectra in Figure 3b. However, we can ensure the same thickness of the centrifuged solid samples for radioluminescence (RL) characterization, and thus provide the quantitative comparison in this set of data (cf. Figure 5). Moreover, as the

target application of our investigation is the high energy radiation detection, quantitative changes in scintillation (unlike PL) parameters are those of real interest.

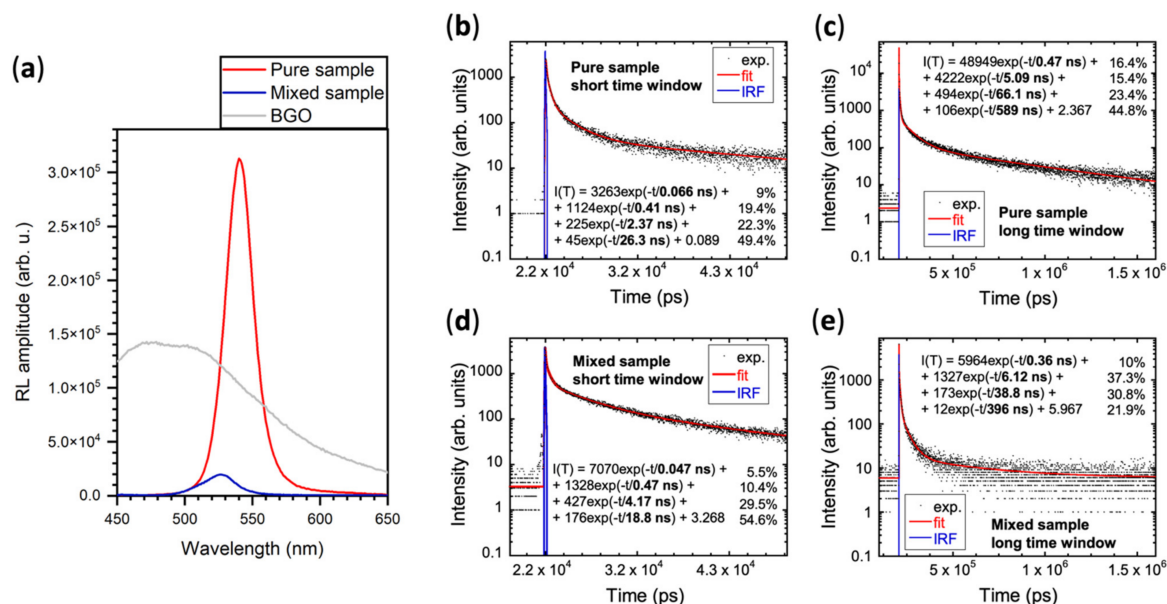


Figure 5. (a) Radioluminescence (RL) spectra of the pure sample (red line) and of the mixed sample (blue line) compared to the RL spectrum of $\text{Bi}_4\text{Ge}_3\text{O}_{12}$ (BGO) powder (grey line); (b–e) scintillation decay curves for both the pure (b,c) and mixed (d,e) samples, recorded in both the short (b,d) and long (c,e) time windows. Black dots represent the experimental data, red line is the best fit (4-exponential function), and blue line is the instrumental response function (IRF).

Figure 5 summarizes RL characterization of both samples with powder $\text{Bi}_3\text{Ge}_4\text{O}_{12}$ (BGO) standard scintillator used for a comparison. Steady state RL spectrum in panel (a) shows that intensity of the pure sample is one order of magnitude larger than that of the mixed sample. One factor contributing to such difference may be the abovementioned higher concentration of surface defects resulting from the smaller CsPbBr_3 nanocrystals present in the mixed sample. However, this alone would not cause such a strong effect. Furthermore, it can be expected that CsPbBr_3 nanocrystals prepared at room temperature by rapid precipitation process would have poorer crystallinity, more crystallographic defects, and, subsequently, lower PLQY, compared to nanocrystals precipitated at elevated temperatures during the hot injection process. However, we have never encountered any evidence in the literature about CsPbBr_3 nanocrystals prepared by the precipitation method and compared to CsPbBr_3 nanocrystals prepared by the hot injection in the same lab to have such poor photoluminescence properties that could result in one order of magnitude difference in scintillation light output.

On the other hand, the presence of Cs_4PbBr_6 crystals in the sample is capable of significantly deteriorating the bright luminescence of CsPbBr_3 nanocrystals due to the emission dumping effect at Cs_4PbBr_6 caused by its strong quenching [34]. Figure 3b shows a significant drop in the excitation spectrum of CsPbBr_3 emission resulting from the Cs_4PbBr_6 absorption. Neither PL decay measurements in Figure 3, nor scintillation decay measurements in Figure 5, indicate any form of energy transfer from Cs_4PbBr_6 to the CsPbBr_3 phase (due to thermal quenching of its emission). Therefore, all the energy that is deposited in Cs_4PbBr_6 crystals is lost to the scintillation process in CsPbBr_3 . Moreover, Cs_4PbBr_6 crystals are one order of magnitude larger than CsPbBr_3 nanocrystals in the mixed sample, therefore they are more capable of efficient stopping the incident X-ray radiation. In addition, they are diluting the CsPbBr_3 concentration in this sample, which

further reduces the probability of effective deposition of incident radiation energy in the CsPbBr₃ phase.

Furthermore, incident radiation generates excitons, or self-trapped electrons and holes, in the Cs₄PbBr₆ lattice. When localized charge carriers diffusing through Cs₄PbBr₆ encounter large and fairly even offset at the conduction and valence band edges (Cs₄PbBr₆ vs. CsPbBr₃), they will likely dissociate, and it may serve to concentrate carriers in CsPbBr₃ [46]. Smaller Cs₄PbBr₆ particles would trigger shorter diffusion length and consequently higher probability of dissociation and charge transfer to CsPbBr₃, again resulting in better efficiency and yield of green emission.

The larger the Cs₄PbBr₆ crystals, the more prominent the above-described effects reducing the overall RL intensity.

Therefore, we conclude that the presence of Cs₄PbBr₆ crystals alongside CsPbBr₃ nanocrystals significantly reduces their scintillation light output.

This conclusion supports theoretical prediction published in the recent Perspective [45]. They considered a CsPbBr₃@Cs₄PbBr₆ quantum-dot-in-host-like composite, and calculated a PL spectrum escaping from 10 μm depth within the sample. They found that, compared to the launched PL spectrum, the escaping one is 100× attenuated and red-shifted by 20 nm. Our experiments qualitatively confirm this weakening of CsPbBr₃ light output in the presence of Cs₄PbBr₆ phase. Our systems were not identical, but in both cases, it was the CsPbBr₃ nanocrystalline phase surrounded by a larger amount of Cs₄PbBr₆ phase in some form, therefore we believe that this comparison is justified. We also confirm a significant red shift (15 nm) between the PL spectrum of colloidal sample (i.e., “launched” spectrum) and RL spectrum of precipitated powder (i.e., “escaping” spectrum from within the sample). This red shift also occurs in the pure sample, where it is even larger (23 nm) due to the higher concentration of absorbing CsPbBr₃ nanocrystals (Cs₄PbBr₆ phase does not absorb the 517 nm light).

Scintillation decay curves of both samples are similar within the uncertainty given by the 4-exponential approximation. They all feature two sub-nanosecond components (50 ps and 400 ps), which is a crucial property for the intended fast timing applications.

The presence of Cs₄PbBr₆ phase does not affect luminescence properties of the sample, other than the scintillation light output. Therefore, for most optoelectronic applications, its presence does not hinder successful implementation. It can even prove beneficial in protecting CsPbBr₃ nanocrystals from a deteriorative effect of air oxygen and humidity, as in [23–25]. However, for applications such as scintillation detectors for fast timing, the drop in the CsPbBr₃ radioluminescence intensity can become detrimental.

4. Conclusions

We synthesized and characterized CsPbBr₃ nanocrystals prepared by the hot injection method (HI) and their mixture with Cs₄PbBr₆ crystals using the room temperature precipitation method (RTP), which we compared and evaluated with respect to possible future optoelectronic applications. Our RTP protocol yields high amount of Cs₄PbBr₆ phase, which allowed us to study its possible effect on the CsPbBr₃ luminescence properties.

We demonstrated that the Cs₄PbBr₆ crystals have significant negative impact on the CsPbBr₃ scintillation light output, most probably due to strong thermal quenching of their luminescence, but do not affect timing properties in any way. This conclusion supports theoretical predictions in [45] even if our system was not identical. We believe that this is another step towards better understanding of such materials regarding their scintillation characteristics. Moreover, our study did not provide any sufficient evidence of an energy transfer between those two phases.

We conclude that the presence of Cs₄PbBr₆ phase should be a concern for any optoelectronic application requiring high scintillation light output, such as scintillation detectors for fast timing applications. In this case, much attention needs to be paid to characterization of the material prepared by the RTP process to rule out the possible presence of Cs₄PbBr₆

phase, especially when thinking of upscaling for large batches for possible future industrial production.

Supplementary Materials: The following are available online at <https://www.mdpi.com/article/10.3390/nano11081935/s1>, Figure S1: Structure of CsPbBr₃ and Cs₄PbBr₆ drawn with VESTA software [S1], details on syntheses, Figure S2: Absorption spectra of the pure sample dispersed in hexane in three different concentrations; absorption spectra of the surfactants in the inset, Figure S3: Emission spectrum (excited at 300 nm) of the mixed sample and corresponding excitation spectra for each emission band, Figure S4: Gaussian decomposition of the mixed sample emission spectrum, and Figure S5: Comparison of PL of both samples excited by the 365 nm UV light. Reference [56] is cited in the supplementary materials.

Author Contributions: Conceptualization, M.N. and V.Č.; Formal analysis, K.D., A.S., J.K., I.J., V.J. and V.B.; Funding acquisition, E.M. and V.Č.; Investigation, K.D., A.S., J.K., I.J., V.J. and V.B.; Supervision, M.N., E.M. and V.Č.; Visualization, K.D.; Writing—original draft, K.D.; Writing—review and editing, K.D., A.S., J.K., M.N., V.J., V.B., E.M. and V.Č. All authors have read and agreed to the published version of the manuscript.

Funding: This research was funded by the Czech Science Foundation, grant number GA20-06374S, the Ministry of Education Youth and Sports, project “Center for advanced applied science”, grant number CZ.02.1.01/0.0/0.0/16_019/0000778 and by the Grant Agency of the Czech Technical University in Prague, grant number SGS20/185/OHK4/3T/14.

Institutional Review Board Statement: Not applicable.

Informed Consent Statement: Not applicable.

Data Availability Statement: The data presented in this study are available on request from the corresponding author.

Acknowledgments: This work was carried out in the frame of Crystal Clear Collaboration. The authors at CTU would like to express thanks to Benoit Mahler from UCB Lyon 1 for his invaluable advice regarding the hot injection methods.

Conflicts of Interest: The authors declare no conflict of interest.

References



1. Nikl, M.; Nitsch, K.; Polák, K.; Pazzi, G.P.; Fabeni, P.; Citrin, D.S.; Gurioli, M. Optical properties of the Pb²⁺-based aggregated phase in a CsCl host crystal: Quantum-confinement effects. *Phys. Rev. B* **1995**, *51*, 5192–5199. [[CrossRef](#)]
2. Babin, V.; Fabeni, P.; Nikl, M.; Nitsch, K.; Pazzi, G.P.; Zazubovich, S. Luminescent CsPbI₃ and Cs₄PbI₆ aggregates in annealed CsI:Pb crystals. *Phys. Status Solidi* **2001**, *226*, 419–428. [[CrossRef](#)]
3. Nikl, M.; Nitsch, K.; Mihóková, E.; Polák, K.; Fabeni, P.; Pazzi, G.P.; Gurioli, M.; Santucci, S.; Phani, R.; Scacco, A.; et al. Luminescence of CsPbBr₃-like quantum dots in CsBr single crystals. *Phys. E Low Dimens. Syst. Nanostruct.* **1999**, *4*, 323–331. [[CrossRef](#)]
4. Protesescu, L.; Yakunin, S.; Bodnarchuk, M.I.; Krieg, F.; Caputo, R.; Hendon, C.H.; Yang, R.X.; Walsh, A.; Kovalenko, M.V. Nanocrystals of cesium lead halide perovskites (CsPbX₃, X = Cl, Br, and I): Novel optoelectronic materials showing bright emission with wide color gamut. *Nano Lett.* **2015**, *15*, 3692–3696. [[CrossRef](#)] [[PubMed](#)]
5. Kulbak, M.; Gupta, S.; Kedem, N.; Levine, I.; Bendikov, T.; Hodes, G.; Cahen, D. Cesium enhances long-term stability of lead bromide perovskite-based solar cells. *J. Phys. Chem. Lett.* **2016**, *7*, 167–172. [[CrossRef](#)]
6. Song, Y.H.; Yoo, J.S.; Kang, B.K.; Choi, S.H.; Ji, E.K.; Jung, H.S.; Yoon, D.H. Long-term stable stacked CsPbBr₃ quantum dot films for highly efficient white light generation in LEDs. *Nanoscale* **2016**, *8*, 19523–19526. [[CrossRef](#)]
7. Swarnkar, A.; Chulliyil, R.; Ravi, V.K.; Irfanullah, M.; Chowdhury, A.; Nag, A. Colloidal CsPbBr₃ perovskite nanocrystals: Luminescence beyond traditional quantum dots. *Angew. Chem. Int. Ed.* **2015**, *54*, 15424–15428. [[CrossRef](#)]
8. Gandini, M.; Villa, I.; Beretta, M.; Gotti, C.; Imran, M.; Carulli, F.; Fantuzzi, E.; Sassi, M.; Zaffalon, M.; Brofferio, C.; et al. Efficient, fast and reabsorption-free perovskite nanocrystal-based sensitized plastic scintillators. *Nat. Nanotechnol.* **2020**, *15*, 462–468. [[CrossRef](#)]
9. Zhang, Y.; Sun, R.; Ou, X.; Fu, K.; Chen, Q.; Ding, Y.; Xu, L.-J.; Liu, L.; Han, Y.; Malko, A.V.; et al. Metal halide perovskite nanosheet for X-ray high-resolution scintillation imaging screens. *ACS Nano* **2019**, *13*, 2520–2525. [[CrossRef](#)]
10. Chen, Q.; Wu, J.; Ou, X.; Huang, B.; Almutlaq, J.; Zhumekenov, A.A.; Guan, X.; Han, S.; Liang, L.; Yi, Z.; et al. All-inorganic perovskite nanocrystal scintillators. *Nature* **2018**, *561*, 88–93. [[CrossRef](#)]

11. Mykhaylyk, V.B.; Kraus, H.; Kapustianyk, V.; Kim, H.J.; Mercere, P.; Rudko, M.; Da Silva, P.; Antonyak, O.; Dendebera, M. Bright and fast scintillations of an inorganic halide perovskite CsPbBr₃ crystal at cryogenic temperatures. *Sci. Rep.* **2020**, *10*, 1–11. [[CrossRef](#)]
12. Li, Y.; Shao, W.; Chen, L.; Wang, J.; Nie, J.; Zhang, H.; Zhang, S.; Gao, R.; Ouyang, X.; Ouyang, X.; et al. Lead-halide Cs₄PbBr₆ single crystals for high-sensitivity radiation detection. *NPG Asia Mater.* **2021**, *13*, 40. [[CrossRef](#)]
13. Moseley, O.D.I.; Doherty, T.A.S.; Parmee, R.; Anaya, M.; Stranks, S.D. Halide perovskites scintillators: Unique promise and current limitations. *J. Mater. Chem. C* **2021**. [[CrossRef](#)]
14. Yang, H.; Li, H.; Yuan, R.; Chen, J.; Zhao, J.; Wang, S.; Liu, Y.; Li, Q.; Zhang, Z. A novel scintillation screen for achieving high-energy ray detection with fast and full-color emission. *J. Mater. Chem. C* **2021**, 7905–7909. [[CrossRef](#)]
15. Luo, B.; Naghadeh, S.B.; Zhang, J.Z. Lead halide perovskite nanocrystals: Stability, surface passivation, and structural control. *ChemNanoMat* **2017**, *3*, 456–465. [[CrossRef](#)]
16. Leijtens, T.; Hoke, E.T.; Grancini, G.; Slotcavage, D.J.; Eperon, G.E.; Ball, J.M.; De Bastiani, M.; Bowring, A.R.; Martino, N.; Wojciechowski, K.; et al. Mapping electric field-induced switchable poling and structural degradation in hybrid lead halide perovskite thin films. *Adv. Energy Mater.* **2015**, *5*, 1–11. [[CrossRef](#)]
17. Guan, H.; Zhao, S.; Wang, H.; Yan, D.; Wang, M.; Zang, Z. Room temperature synthesis of stable single silica-coated CsPbBr₃ quantum dots combining tunable red emission of Ag–In–Zn–S for High-CRI white light-emitting diodes. *Nano Energy* **2020**, *67*, 104279. [[CrossRef](#)]
18. Shao, H.; Bai, X.; Pan, G.; Cui, H.; Zhu, J.; Zhai, Y.; Liu, J.; Dong, B.; Xu, L.; Song, H. Highly efficient and stable blue-emitting CsPbBr₃@SiO₂ nanospheres through low temperature synthesis for nanoprinting and WLED. *Nanotechnology* **2018**, *29*, 285706. [[CrossRef](#)]
19. Zhong, Q.; Cao, M.; Hu, H.; Yang, D.; Chen, M.; Li, P.; Wu, L.; Zhang, Q. One-pot synthesis of highly stable CsPbBr₃@SiO₂ core-shell nanoparticles. *ACS Nano* **2018**, *12*, 8579–8587. [[CrossRef](#)] [[PubMed](#)]
20. Li, Z.J.; Hofman, E.; Li, J.; Davis, A.H.; Tung, C.H.; Wu, L.Z.; Zheng, W. Photoelectrochemically active and environmentally stable CsPbBr₃/TiO₂ core/shell nanocrystals. *Adv. Funct. Mater.* **2018**, *28*, 1–7. [[CrossRef](#)]
21. Yang, W.; Gao, F.; Qiu, Y.; Liu, W.; Xu, H.; Yang, L.; Liu, Y. CsPbBr₃-quantum-dots/Polystyrene@Silica hybrid microsphere structures with significantly improved stability for white LEDs. *Adv. Opt. Mater.* **2019**, *7*, 1–12. [[CrossRef](#)]
22. Cai, Y.; Wang, L.; Zhou, T.; Zheng, P.; Li, Y.; Xie, R.J. Improved stability of CsPbBr₃ perovskite quantum dots achieved by suppressing interligand proton transfer and applying a polystyrene coating. *Nanoscale* **2018**, *10*, 21441–21450. [[CrossRef](#)]
23. He, M.; Wang, C.; Li, J.; Wu, J.; Zhang, S.; Kuo, H.C.; Shao, L.; Zhao, S.; Zhang, J.; Kang, F.; et al. CsPbBr₃-Cs₄PbBr₆ composite nanocrystals for highly efficient pure green light emission. *Nanoscale* **2019**, *11*, 22899–22906. [[CrossRef](#)]
24. Chen, Y.M.; Zhou, Y.; Zhao, Q.; Zhang, J.Y.; Ma, J.P.; Xuan, T.T.; Guo, S.Q.; Yong, Z.J.; Wang, J.; Kuroiwa, Y.; et al. Cs₄PbBr₆/CsPbBr₃ Perovskite composites with near-unity luminescence quantum yield: Large-scale synthesis, luminescence and formation mechanism, and white light-emitting diode application. *ACS Appl. Mater. Interfaces* **2018**, *10*, 15905–15912. [[CrossRef](#)] [[PubMed](#)]
25. Xu, J.; Huang, W.; Li, P.; Onken, D.R.; Dun, C.; Guo, Y.; Ucer, K.B.; Lu, C.; Wang, H.; Geyer, S.M.; et al. Imbedded nanocrystals of CsPbBr₃ in Cs₄PbBr₆: Kinetics, enhanced oscillator strength, and application in light-emitting diodes. *Adv. Mater.* **2017**, *29*, 1–10. [[CrossRef](#)]
26. Grandhi, G.K.; Viswanath, N.S.M.; Cho, H.B.; Kim, S.M.; Im, W. Bin Highly stable hetero-structured green-emitting cesium lead bromide nanocrystals: Via ligand-mediated phase control. *Nanoscale* **2019**, *11*, 21137–21146. [[CrossRef](#)]
27. Jing, Q.; Xu, Y.; Su, Y.; Xing, X.; Lu, Z. A systematic study of the synthesis of cesium lead halide nanocrystals: Does Cs₄PbBr₆ or CsPbBr₃ form? *Nanoscale* **2019**, *11*, 1784–1789. [[CrossRef](#)]
28. Cao, F.; Yu, D.; Xu, X.; Han, Z.; Zeng, H. CsPbBr₃@Cs₄PbBr₆ Emitter-in-host composite: Fluorescence origin and interphase energy transfer. *J. Phys. Chem. C* **2021**, *125*, 3–19. [[CrossRef](#)]
29. Saidaminov, M.I.; Almutlaq, J.; Sarmah, S.; Dursun, I.; Zhumekenov, A.A.; Begum, R.; Pan, J.; Cho, N.; Mohammed, O.F.; Bakr, O.M. Pure Cs₄PbBr₆: Highly luminescent zero-dimensional perovskite solids. *ACS Energy Lett.* **2016**, *1*, 840–845. [[CrossRef](#)]
30. Zhang, Y.; Saidaminov, M.I.; Dursun, I.; Yang, H.; Murali, B.; Alarousu, E.; Yengel, E.; Alshankiti, B.A.; Bakr, O.M.; Mohammed, O.F. Zero-dimensional Cs₄PbBr₆ perovskite nanocrystals. *J. Phys. Chem. Lett.* **2017**, *8*, 961–965. [[CrossRef](#)]
31. Qin, Z.; Dai, S.; Hadjiev, V.G.; Wang, C.; Xie, L.; Ni, Y.; Wu, C.; Yang, G.; Chen, S.; Deng, L.; et al. Revealing the origin of luminescence center in 0D Cs₄PbBr₆ perovskite. *Chem. Mater.* **2019**, *31*, 9098–9104. [[CrossRef](#)]
32. Xu, Q.; Wang, J.; Shao, W.; Ouyang, X.; Wang, X.; Zhang, X.; Guo, Y.; Ouyang, X. A solution-processed zero-dimensional all-inorganic perovskite scintillator for high resolution gamma-ray spectroscopy detection. *Nanoscale* **2020**, *12*, 9727–9732. [[CrossRef](#)]
33. Kostopoulou, A.; Brintakis, K.; Serpetzoglou, E.; Stratakis, E. Laser-assisted fabrication for metal halide perovskite-2D nanoconjugates: Control on the nanocrystal density and morphology. *Nanomaterials* **2020**, *10*, 747. [[CrossRef](#)] [[PubMed](#)]
34. Nikl, M.; Mihóková, E.; Nitsch, K.; Somma, F.; Giampaolo, C.; Pazzi, G.; Fabeni, P.; Zazubovich, S. Photoluminescence of Cs₄PbBr₆ crystals and thin films. *Chem. Phys. Lett.* **1999**, *306*, 280–284. [[CrossRef](#)]
35. Yang, L.; Li, D.; Wang, C.; Yao, W.; Wang, H.; Huang, K. Room-temperature synthesis of pure perovskite-related Cs₄PbBr₆ nanocrystals and their ligand-mediated evolution into highly luminescent CsPbBr₃ nanosheets. *J. Nanopart. Res.* **2017**, *19*, 258. [[CrossRef](#)]

36. Rao, L.; Ding, X.; Du, X.; Liang, G.; Tang, Y.; Tang, K.; Zhang, J.Z. Ultrasonication-assisted synthesis of CsPbBr₃ and Cs₄PbBr₆ perovskite nanocrystals and their reversible transformation. *Beilstein J. Nanotechnol.* **2019**, *10*, 666–676. [[CrossRef](#)]
37. Palazon, F.; Urso, C.; De Trizio, L.; Akkerman, Q.; Marras, S.; Locardi, F.; Nelli, I.; Ferretti, M.; Prato, M.; Manna, L. Postsynthesis transformation of insulating Cs₄PbBr₆ nanocrystals into bright perovskite CsPbBr₃ through physical and chemical extraction of CsBr. *ACS Energy Lett.* **2017**, *2*, 2445–2448. [[CrossRef](#)]
38. Baranov, D.; Caputo, G.; Goldoni, L.; Dang, Z.; Scarfiello, R.; De Trizio, L.; Portone, A.; Fabbri, F.; Camposeo, A.; Pisignano, D.; et al. Transforming colloidal Cs₄PbBr₆ nanocrystals with poly(maleic anhydride-alt-1-octadecene) into stable CsPbBr₃ perovskite emitters through intermediate heterostructures. *Chem. Sci.* **2020**, *11*, 3986–3995. [[CrossRef](#)]
39. Akkerman, Q.A.; Park, S.; Radicchi, E.; Nunzi, F.; Mosconi, E.; De Angelis, F.; Brescia, R.; Rastogi, P.; Prato, M.; Manna, L. Nearly monodisperse insulator Cs₄PbX₆ (X = Cl, Br, I) nanocrystals, their mixed halide compositions, and their transformation into CsPbX₃ nanocrystals. *Nano Lett.* **2017**, *17*, 1924–1930. [[CrossRef](#)]
40. Yin, J.; Yang, H.; Song, K.; El-Zohry, A.M.; Han, Y.; Bakr, O.M.; Brédas, J.L.; Mohammed, O.F. Point defects and green emission in zero-dimensional perovskites. *J. Phys. Chem. Lett.* **2018**, *9*, 5490–5495. [[CrossRef](#)]
41. Cha, J.H.; Lee, H.J.; Kim, S.H.; Ko, K.C.; Suh, B.J.; Han, O.H.; Jung, D.Y. Superparamagnetism of green emissive Cs₄PbBr₆ zero-dimensional perovskite crystals. *ACS Energy Lett.* **2020**, *5*, 2208–2216. [[CrossRef](#)]
42. Yang, L.; Wang, T.; Yang, X.; Zhang, M.; Pi, C.; Yu, J.; Zhou, D.; Yu, X.; Qiu, J.; Xu, X. Extrinsic photoluminescence properties of individual micro-particle of Cs₄PbBr₆ perovskite with “defect” structure. *Opt. Express* **2019**, *27*, 31207. [[CrossRef](#)]
43. Lecoq, P.; Morel, C.; Prior, J.O.; Visvikis, D.; Gundacker, S.; Auffray, E.; Križan, P.; Turtos, R.M.; Thers, D.; Charbon, E.; et al. Roadmap toward the 10 ps time-of-flight PET challenge. *Phys. Med. Biol.* **2020**, *65*, 21RM01. [[CrossRef](#)]
44. Tomanová, K.; Suchá, A.; Mihóková, E.; Procházková, L.; Jakubec, I.; Turtos, R.M.; Gundacker, S.; Auffray, E.; Čuba, V. CsPbBr₃ thin films on LYSO:Ce substrates. *IEEE Trans. Nucl. Sci.* **2020**, *67*, 933–938. [[CrossRef](#)]
45. Williams, R.T.; Wolszczak, W.W.; Yan, X.; Carroll, D.L. Perovskite quantum-dot-in-host for detection of ionizing radiation. *ACS Nano* **2020**, *14*, 5161–5169. [[CrossRef](#)] [[PubMed](#)]
46. Kang, B.; Biswas, K. Exploring polaronic, excitonic structures and luminescence in Cs₄PbBr₆/CsPbBr₃. *J. Phys. Chem. Lett.* **2018**, *9*, 830–836. [[CrossRef](#)]
47. Cao, F.; Yu, D.; Ma, W.; Xu, X.; Cai, B.; Yang, Y.M.; Liu, S.; He, L.; Ke, Y.; Lan, S.; et al. shining emitter in a stable host: Design of halide perovskite scintillators for X-ray imaging from commercial concept. *ACS Nano* **2020**, *14*, 5183–5193. [[CrossRef](#)]
48. Li, X.; Wu, Y.; Zhang, S.; Cai, B.; Gu, Y.; Song, J.; Zeng, H. CsPbX₃ quantum dots for lighting and displays: Room-temperature synthesis, photoluminescence superiorities, underlying origins and white light-emitting diodes. *Adv. Funct. Mater.* **2016**, *26*, 2435–2445. [[CrossRef](#)]
49. Lu, C.; Wright, M.W.; Ma, X.; Li, H.; Itanze, D.S.; Carter, J.A.; Hewitt, C.A.; Donati, G.L.; Carroll, D.L.; Lundin, P.M.; et al. Cesium oleate precursor preparation for lead halide perovskite nanocrystal synthesis: The influence of excess oleic acid on achieving solubility, conversion, and reproducibility. *Chem. Mater.* **2019**, *31*, 62–67. [[CrossRef](#)]
50. Tomanová, K.; Čuba, V.; Brik, M.G.; Mihóková, E.; Martínez Turtos, R.; Lecoq, P.; Auffray, E.; Nikl, M. On the structure, synthesis, and characterization of ultrafast blue-emitting CsPbBr₃ nanoplatelets. *APL Mater.* **2019**, *7*, 011104. [[CrossRef](#)]
51. Abramoff, M.D.; Magalhães, P.J.; Ram, S.J. Image processing with imageJ. *Biophotonics Int.* **2004**, *11*, 36–41. [[CrossRef](#)]
52. Lábár, J.L. “ProcessDiffraction”: A computer program to process electron diffraction patterns from polycrystalline or amorphous samples. *Proc. Eurem* **2000**, *3*, I379–I380.
53. Zhang, Z.; Zhu, Y.; Wang, W.; Zheng, W.; Lin, R.; Li, X.; Zhang, H.; Zhong, D.; Huang, F. Aqueous solution growth of millimeter-sized nongreen-luminescent wide bandgap Cs₄PbBr₆ bulk crystal. *Cryst. Growth Des.* **2018**, *18*, 6393–6398. [[CrossRef](#)]
54. Kondo, S.; Amaya, K.; Saito, T. Localized optical absorption in Cs₄PbBr₆. *J. Phys. Condens. Matter* **2002**, *14*, 2093–2099. [[CrossRef](#)]
55. Quan, L.N.; Quintero-Bermudez, R.; Voznyy, O.; Walters, G.; Jain, A.; Fan, J.Z.; Zheng, X.; Yang, Z.; Sargent, E.H. Highly emissive green perovskite nanocrystals in a solid state crystalline matrix. *Adv. Mater.* **2017**, *29*, 1–6. [[CrossRef](#)]
56. Momma, K.; Izumi, F. VESTA3 for three-dimensional visualization of crystal, volumetric and morphology data. *J. Appl. Crystallogr.* **2011**, *44*, 1272–1276. [[CrossRef](#)]

Article

Scintillation Response Enhancement in Nanocrystalline Lead Halide Perovskite Thin Films on Scintillating Wafers

 Kateřina Děcká ^{1,2,*} , Jan Král ¹ , František Hájek ^{2,3}, Petr Průša ^{2,4}, Vladimír Babin ², Eva Mihóková ^{2,3} and Václav Čuba ¹

- ¹ Department of Nuclear Chemistry, Faculty of Nuclear Sciences and Physical Engineering, Czech Technical University in Prague, Břehová 7, 115 19 Prague, Czech Republic; kralja13@fjfi.cvut.cz (J.K.); vaclav.cuba@fjfi.cvut.cz (V.Č.)
- ² Institute of Physics of the Czech Academy of Sciences, Cukrovarnická 10, 162 00 Prague, Czech Republic; hajek@fzu.cz (F.H.); petr.prusa@fjfi.cvut.cz (P.P.); babinv@fzu.cz (V.B.); mihokova@fzu.cz (E.M.)
- ³ Department of Solid State Engineering, Faculty of Nuclear Sciences and Physical Engineering, Czech Technical University in Prague, Břehová 7, 115 19 Prague, Czech Republic
- ⁴ Department of Dosimetry and Application of Ionizing Radiation, Faculty of Nuclear Sciences and Physical Engineering, Czech Technical University in Prague, Břehová 7, 115 19 Prague, Czech Republic
- * Correspondence: Katerina.Decka@fjfi.cvut.cz

Abstract: Lead halide perovskite nanocrystals of the formula CsPbBr₃ have recently been identified as potential time taggers in scintillating heterostructures for time-of-flight positron emission tomography (TOF-PET) imaging thanks to their ultrafast decay kinetics. This study investigates the potential of this material experimentally. We fabricated CsPbBr₃ thin films on scintillating GGAG:Ce (Gd_{2.985}Ce_{0.015}Ga_{2.7}Al_{2.3}O₁₂) wafer as a model structure for the future sampling detector geometry. We focused this study on the radioluminescence (RL) response of this composite material. We compare the results of two spin-coating methods, namely the static and the dynamic process, for the thin film preparation. We demonstrated enhanced RL intensity of both CsPbBr₃ and GGAG:Ce scintillating constituents of a composite material. This synergic effect arises in both the RL spectra and decays, including decays in the short time window (50 ns). Consequently, this study confirms the applicability of CsPbBr₃ nanocrystals as efficient time taggers for ultrafast timing applications, such as TOF-PET.

Keywords: lead halide perovskites; nanocrystals; thin films; heterostructure; scintillator; fast timing; TOF-PET



Citation: Děcká, K.; Král, J.; Hájek, F.; Průša, P.; Babin, V.; Mihóková, E.; Čuba, V. Scintillation Response Enhancement in Nanocrystalline Lead Halide Perovskite Thin Films on Scintillating Wafers. *Nanomaterials* **2022**, *12*, 14. <https://doi.org/10.3390/nano12010014>

Academic Editors: Marcela Socol and Nicoleta Preda

Received: 18 November 2021

Accepted: 17 December 2021

Published: 21 December 2021

Publisher's Note: MDPI stays neutral with regard to jurisdictional claims in published maps and institutional affiliations.



Copyright: © 2021 by the authors. Licensee MDPI, Basel, Switzerland. This article is an open access article distributed under the terms and conditions of the Creative Commons Attribution (CC BY) license (<https://creativecommons.org/licenses/by/4.0/>).

1. Introduction

Lead halide perovskite nanocrystals of the formula CsPbX₃ (X = Cl, Br, I) were first reported more than 20 years ago [1–3], but have only been studied thoroughly since 2015, when their colloidal synthesis was introduced [4]. There are a large body of papers published on this topic, but the majority of work focuses on their luminescent properties and applications such as LEDs, displays, photovoltaics, or lasers [5–7].

However, their properties such as fast decay times, narrow emission bands, and high light yield are also desirable for scintillation detectors. Some papers have been published on this topic [8–14], but not nearly as many.

Moreover, in contrast with, e.g., CsPbBr₃ single crystals [11], CsPbBr₃ nanocrystals show negative thermal quenching (increase of radioluminescence intensity with increasing temperature) leading to scintillation light yield of $24,000 \pm 2100 \text{ MeV}^{-1}$ at 300 K under 662 keV excitation, which is one order of magnitude higher than other nanocrystals in this family, namely FAPbBr₃ and CsPbI₃ [15].

The application of any nanocrystals as prospective scintillators has some common issues, among which the most serious is their poor stopping power. Simple calculation shows

that the half-value layer of CsPbBr₃ for Cu K_α line is ~7.5 μm and for Bremsstrahlung generated in X-ray tube operating at 40 kV the half-value layer is ~100 μm (see Supplementary Information for details and used values). This means that nanocrystals must be in the form of a sufficiently thick film to stop at least some of the incident radiation. Moreover, these values represent only the lower limit of a rough estimate, because they do not take into consideration the reduction of density due to the presence of surface ligands and the lower density of nanomaterials compared to their bulk counterparts. Therefore, real half-values will be even larger.

To fabricate high quality thin films of such thicknesses is not an easy task by itself. Moreover, in such thick films one can expect serious issues with self-absorption, because semiconductor nanocrystals have generally small Stokes shifts and CsPbX₃ nanocrystals are no exception. Small Stokes shift can be overcome by introducing a wavelength shifter to the mixture [16], but it will inevitably lead to longer rise and decay times, which is undesirable for some applications requiring fast response, such as time-of-flight positron emission tomography (TOF-PET) or high energy physics.

It has been proposed and explored before, that a sandwich-like structure combining the bulk scintillator with high stopping power and semiconductor nanocrystals with ultrafast decay times is highly promising for TOF-PET detectors [17,18]. The bulk scintillator serves as a stopping medium and provides the energy resolution and nanocrystals serve as time taggers.

In this work we fabricate similar, but much simpler composite materials; CsPbBr₃ thin films on GGAG:Ce (Gd₃(Al,Ga)₅O₁₂:Ce) scintillating wafer. GGAG:Ce is a modern scintillator that possesses high stopping power (effective atomic number $Z_{\text{eff}} = 54$) and high light yield, slightly under 60,000 MeV⁻¹ when optimized [19,20]. We use lower energy X-rays to characterize this nanocomposite as the first step towards future study of CsPbBr₃ on GGAG:Ce sandwich pixel under 511 keV gamma-rays excitation. We show an enhancement effect between these two materials that leads to improved radioluminescence intensities (higher than a simple sum of individual emissions), while preserving the sub-nanosecond decay components of CsPbBr₃ nanocrystals both in photo- and radioluminescence decays.

2. Materials and Methods

2.1. Chemicals

Cs₂CO₃ (99.9%, Sigma-Aldrich, Saint Louis, MO, USA), PbBr₂ (99.999%, Sigma-Aldrich), oleylamine (OAm, 70%, Sigma-Aldrich), oleic acid (OA, 90%, Sigma-Aldrich), 1-octadecene (90%, Sigma-Aldrich), toluene (99.8%, Sigma-Aldrich), didodecyldimethylammonium bromide (DDAB, 98%, Sigma-Aldrich), and ethylacetate (p. a., PENTA, Prague, Czech Republic). All chemicals were used as received without further purification, unless stated otherwise.

2.2. Wafers for Thin Films

We used two types of wafers for thin films deposition: a commercially available glass slide as a non-scintillating wafer (square, 18 mm × 18 mm × 0.17 mm, Hirschmann, Eberstadt, Germany) and GGAG:Ce as a scintillating wafer (circle, ~15 mm in diameter and 0.2 mm thick). The GGAG:Ce (Gd_{2.985}Ce_{0.015}Ga_{2.7}Al_{2.3}O₁₂) was grown at the Czech Academy of Sciences.

2.3. CsPbBr₃ Synthesis

To synthesize CsPbBr₃ nanocrystals, the standard hot-injection (HI) procedure introduced by Protesescu et al. was used [4]. The preparation of cesium oleate was modified to increase Cs:OA ratio in the reaction to 1:5 according to the study by Lu et al. [21]. In short, 0.752 mmol of PbBr₂, 20 mL of 1-octadecene (ODE), 2 mL of oleylamine (OAm), and 1.78 mL of oleic acid (OA), were mixed in 100 mL 3-neck flask and degassed at 110 °C under vacuum for 1 h. After that, 0.5 mL of dried pre-synthesized cesium oleate solution (0.4 M)

was injected at 170 °C under argon atmosphere. More details on the CsPbBr₃ synthesis can be found in our previous publication [22].

Ligand exchange reaction was performed following the procedure presented by Imran et al. [23], and all exchange reactions were performed at room temperature in air. The crude reaction mixture from HI synthesis was mixed with 55 mM DDAB toluene solution (volume ratio 3:2) and vigorously stirred for 2 min. Thereafter, NCs were precipitated by addition of ethyl acetate (15 mL per 3 mL of crude reaction mixture) and isolated by centrifugation for 10 min at 4800 × g. Final CsPbBr₃ solution was obtained by redispersion in toluene.

For preparation of CsPbBr₃ thin films, the solution concentration was adjusted to 45–50 mg·mL⁻¹. The NC concentration was determined from the solution absorbance at 400 nm according to Maes et al. [24].

2.4. Thin Film Fabrication

CsPbBr₃ thin films were fabricated using the spin-coating technique, two different processes of repeated spin-coating were developed to prepare thicker films.

In the static process the solution was repeatedly deposited on stationary wafer followed by rotation at 2000 rpm for 1 min. Films on the glass wafer were prepared by depositing 40 μL of solution 40× (to compare with the dynamic process) or 50× (for the rest of experiments), the film on scintillating wafer was fabricated by deposition of 20 μL repeated 50×. Smaller amount of solution (20 μL) was used because GGAG:Ce wafer is smaller than the glass wafer.

In the dynamic process the solution was deposited dropwise on constantly rotating substrate. Spacing between individual drops was 45 s, rotation rate was 2000 rpm. To fabricate the CsPbBr₃ film on the glass slide, 600 μL of the solution was used; the thin film on scintillating wafer was prepared using 500 μL of the solution.

2.5. Characterization

X-ray powder diffraction (XRPD) was measured using a Rigaku Miniflex 600 diffractometer equipped with the Cu X-ray tube (average wavelength $K_{\alpha 1,2}$ 0.15418 nm, voltage 40 kV, current 15 mA). Data were collected with a speed of 2°/min and compared with the ICDD PDF-2 database, version 2013. The Halder–Wagner method with Scherrer constant value 0.94 was used for the determination of the linear crystallite size. The scanning electron microscopy (SEM) was obtained using an FEI XL30 ESEM microscope with home-build cathodoluminescence setup for measurement spectrally and spatially resolved cathodoluminescence. It consists of optical system for light collection, single-grating monochromator, and photomultiplier tube Hamamatsu H7711-13. Width of slits enable better than 20 nm spectral resolution. Absorption spectra were collected using a Cary 100 spectrophotometer (Varian, Palo Alto, CA, USA). Photoluminescence (PL) excitation and emission spectra were collected using a FluoroMax spectrofluorometer (Horiba Jobin Yvon, Kyoto, Japan). Radioluminescence (RL) spectra were collected using a 5000M spectrofluorometer (Horiba Jobin Yvon) with a monochromator and TBX-04 (IBH, Glasgow, Scotland) photodetector, the excitation source was a Seifert X-ray tube (40 kV, 15 mA). RL decay curves were collected using the hybrid picosecond photon detector HPPD-860 and Fluorohub unit (Horiba Scientific, Kyoto, Japan). Samples were excited by the picosecond (ps) X-ray tube N5084 from Hamamatsu, operating at 40 kV. The X-ray tube was driven by the ps light pulser (Hamamatsu, Hamamatsu City, Japan) equipped with a laser diode operating at 405 nm. The instrumental response function FWHM of the setup is about 76 ps. Convolution procedure was applied to all decay curves to determine true decay times (SpectraSolve 3.01 PRO software package, Ames Photonics, Fort Worth, TX, USA). The contribution of a component expressed as a percentage (often referred to as a light sum, LS) was calculated as:

$$LS_n = \frac{A_n \tau_n}{\sum A_i \tau_i}$$

where A_n and τ_n denote the amplitude and decay time of the n th component. All luminescence measurements were performed using similar configuration, the emission was detected from the same surface where excited.

3. Results and Discussion

CsPbBr₃ samples used for the thin film fabrication were analyzed using the X-ray powder diffraction (XRPD), photoluminescence emission (PL), and excitation (PLE) spectra, as well as absorption spectra (see Figure 1).

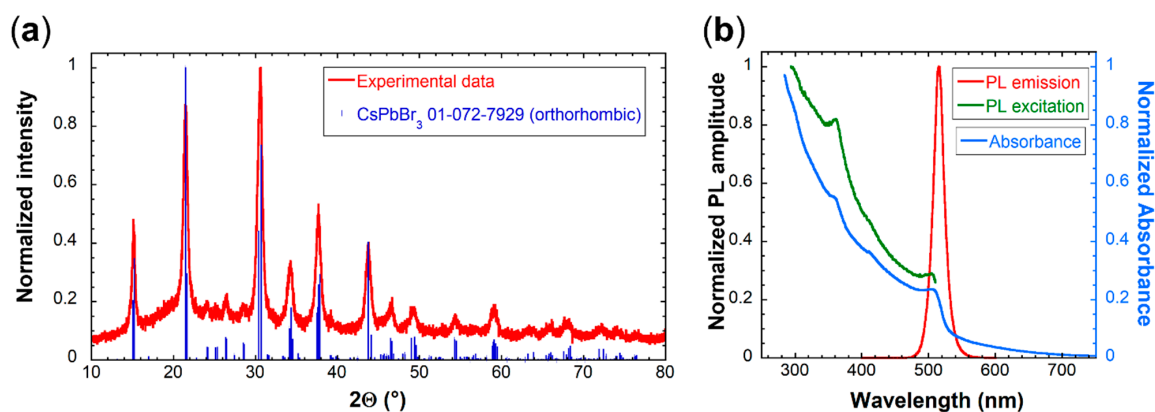


Figure 1. (a) XRPD pattern (red line) of synthesized material used for spin-coating. Identified phase according to ICDD PDF-2 database was orthorhombic CsPbBr₃ no. 01-072-7929 (blue lines). (b) PL emission (red line), excitation (green line), and absorption (blue line) spectra of synthesized solution used for spin-coating.

XRPD analysis in Figure 1 shows that synthesized nanocrystals were pure orthorhombic CsPbBr₃ phase with the mean crystallite size of (13.8 ± 0.6) nm, which is consistent with the value obtained by XRPD and TEM analysis in our previous paper [22]. The phase purity is further confirmed by the PLE spectrum in Figure 1b lacking the dip at 310 nm, and absorption spectrum lacking the peak at the same wavelength, which are both characteristic of the Cs₄PbBr₆ impurity [22,25,26]. The PL spectrum shows a single excitonic peak at 515 nm. More detailed characterization of the same type of samples prepared before can be found in our recently published work [22].

CsPbBr₃ for the thin film fabrication had to be surface modified using a ligand exchange procedure of oleic acid and oleylamine for dioleyldimethylammonium bromide (DDAB) [23]. Without the ligand exchange, thicker films with higher radioluminescence (RL) intensity could not be prepared, see Figure S1 in Supplementary Information. DDAB capping allowed repeated spin-coating process in order to increase the film thickness, see Figures S2–S4 in Supplementary Information. Figure 2 shows two optimized processes for fabrication of thin films with sufficient thickness.

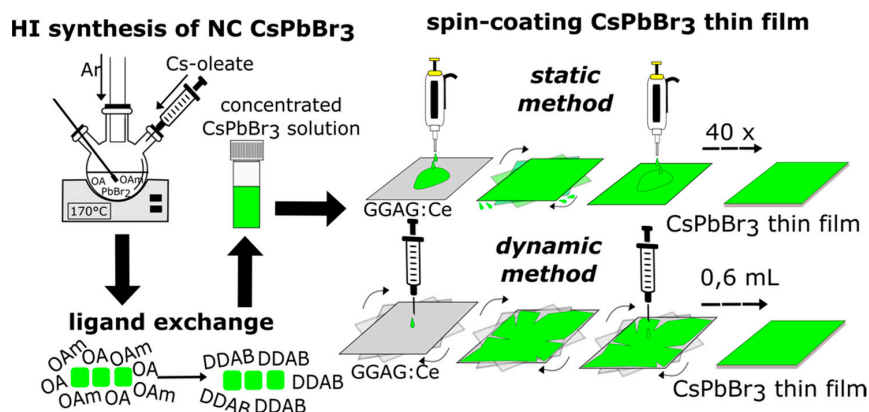


Figure 2. Schematic representation of the synthesis and spin-coating processes; hot injection (HI) synthesis, ligand exchange of oleic acid (OA) and oleylamine (OAm) for dioleoyldimethylammonium bromide (DDAB) and static and dynamic spin-coating processes.

Figure 3 displays RL spectra of CsPbBr₃ films prepared by both methods. It is clear that the dynamic process yields the film with higher RL intensity. Even better, this film was prepared with significantly lower amount of material (0.6 mL for the dynamic process vs. 1.6 mL for 40 layers of the static process), which significantly reduces its cost. On the other hand, the static process yields the film of much higher homogeneity even to the naked eye as evidenced by the photographs in the inset of Figure 3.

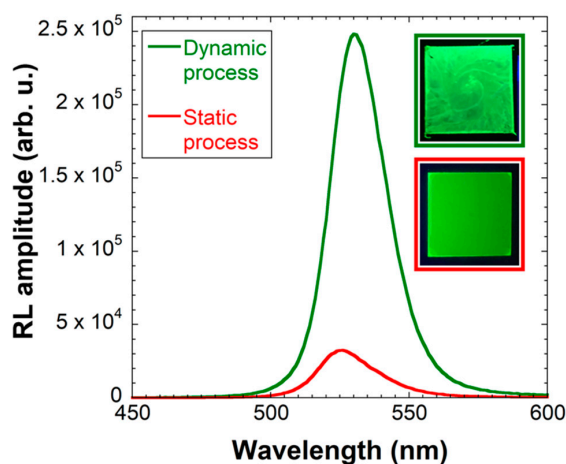


Figure 3. RL spectra of CsPbBr₃ thin films on glass prepared by using 0.6 mL of CsPbBr₃ solution in the dynamic process (green line) and by stacking 40 layers in the static process (red line). Inset: Photographs under UV illumination of the film prepared by the dynamic process (top) and static process (bottom).

Please note that the RL spectra of thin films are red-shifted compared to the PL spectrum of CsPbBr₃ nanocrystals in Figure 1b. This shift is probably caused by different excitation process under X-rays, and also by reabsorption inevitably occurring in the CsPbBr₃ layer due to its small Stokes shift, as discussed in the Introduction section.

A question to be answered is whether a good homogeneity of the thin film is that important for the intended application in TOF-PET, where crucial requirements are the high light output and fast response (i.e., fast rise and decay times) [18]. To find the answer, both processes were used to prepare films on scintillating GGAG:Ce wafer and both RL spectra and decays were measured.

The mean measured thickness of the film prepared by the static process was $\sim 3 \mu\text{m}$ (5 spots, $2.4 \mu\text{m}$ – $3.7 \mu\text{m}$) and for the dynamic process it was also $\sim 3 \mu\text{m}$, but with much wider distribution (12 spots, $1.08 \mu\text{m}$ – $5.58 \mu\text{m}$) (see Figures S4 and S5 in Supplementary Information for relevant SEM images).

Figure 4 shows RL spectra of CsPbBr₃ films prepared by both processes compared to a pure GGAG:Ce plate and pure CsPbBr₃ film on glass prepared by the static process. CsPbBr₃ films on GGAG:Ce prepared by both methods show significantly larger RL intensity than both pure GGAG:Ce and pure CsPbBr₃ on glass, even if part of the GGAG:Ce emission (below $\sim 530 \text{ nm}$) is absorbed by the CsPbBr₃ layer (cf. absorption spectrum in Figure 1). Please note that the quantitative comparison to the film on glass is not entirely appropriate because of the size difference in the wafers. The glass wafer is larger, therefore its luminescence intensity is actually overvalued, which further illustrates the relatively low RL intensity of the pure CsPbBr₃ film on glass wafer.

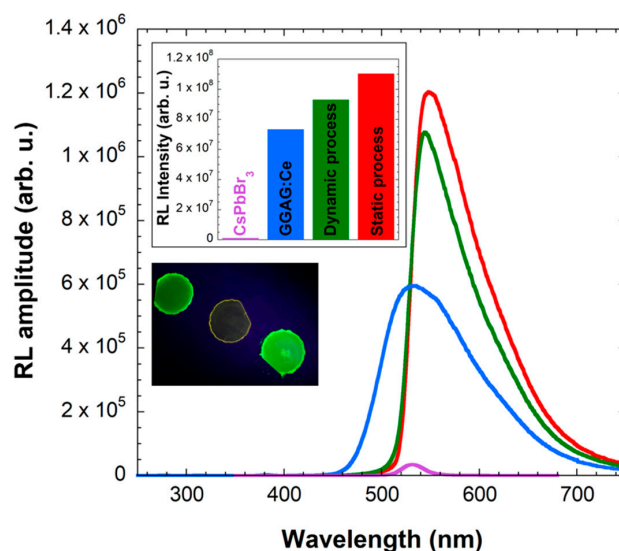


Figure 4. RL spectra of prepared CsPbBr₃ films on glass by the static process (purple line) and on GGAG:Ce by the static process (red line) and the dynamic process (green line), compared to the pure GGAG:Ce wafer (blue line). Graph in the inset: Integrated RL intensities of presented spectra. Photograph in the inset, from left to right: CsPbBr₃ film on GGAG:Ce prepared by the static process, pure GGAG:Ce wafer, CsPbBr₃ film on GGAG:Ce prepared by the dynamic process. Note that UV illumination intensity is not homogeneous among the samples.

The overall intensity of the nanocomposite is in both cases (the static and the dynamic processes) higher than a simple sum of the two individual emissions. The shape of the RL spectra indicate that both CsPbBr₃ and GGAG:Ce emissions are enhanced. The CsPbBr₃ emission is probably enhanced by the absorption and subsequent reemission of the GGAG:Ce emission. However, the enhancement of GGAG:Ce emission cannot be explained easily.

Interestingly, in contrast to previous results in Figure 3, there is not much difference in RL spectra of CsPbBr₃ films prepared by different methods on GGAG:Ce wafer. At this point, it seems that the answer to our question is that the homogeneity of the fabricated film does not play a significant role in the overall RL intensity of the final nanocomposite.

The enhancement of the GGAG:Ce emission can be explained by analyzing SEM pictures and cathodoluminescence data, see Figure 5. Micrographs at very low magnification ($78\times$, Figure 5a,b) confirm that the thin film prepared using the dynamic process has poor homogeneity and very large cracks. SEM image in Figure 5c shows the static thin film at higher magnification ($625\times$), which reveals that this film also has cracks, but much thinner.

Figure 5d (cathodoluminescence image) shows that the 560 nm light, which is emitted solely by GGAG:Ce, is shining with high intensity through the cracks. This phenomenon can explain the enhancement of the wafer's RL response in Figure 4; the cracks probably serve as a light guide for its emission. Similar effect has been observed before [27] and is even investigated as a way for deliberate increase of light extraction [28].

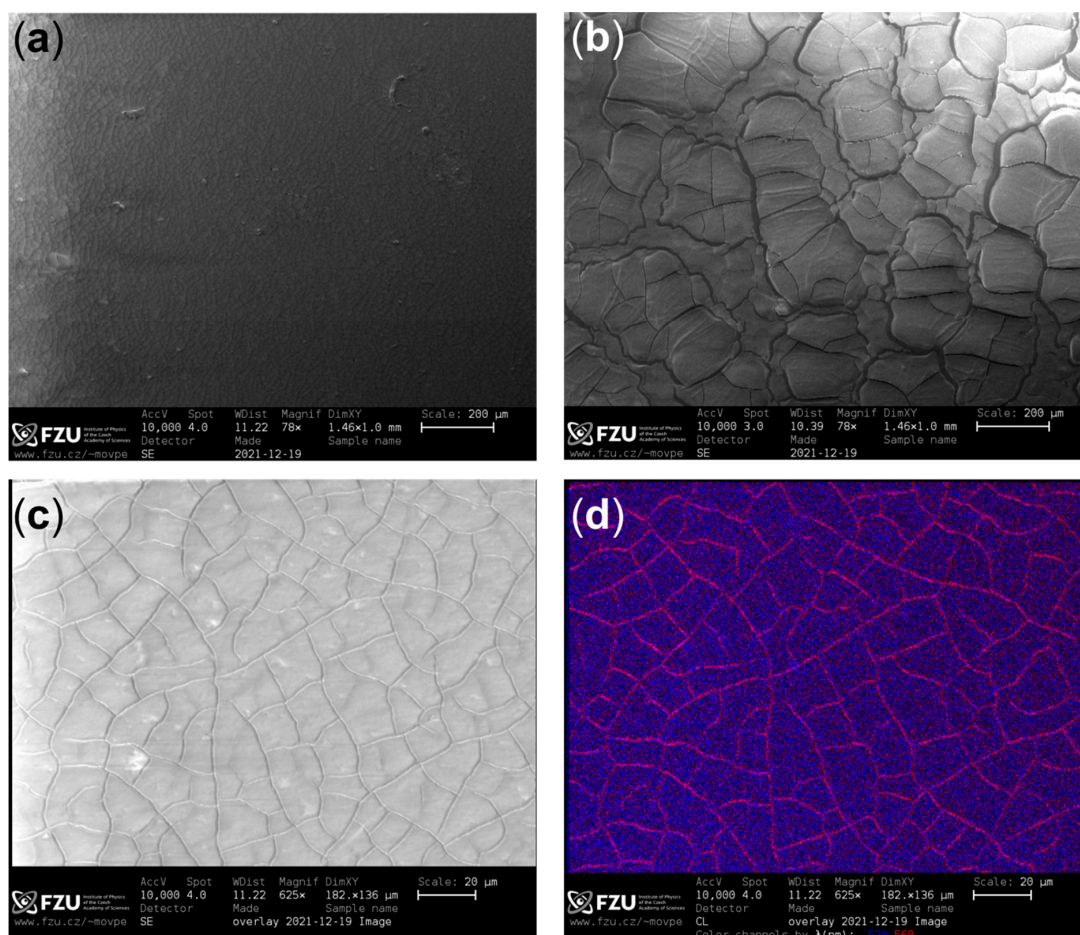


Figure 5. SEM images of the CsPbBr₃ film on GGAG:Ce prepared by the static (a) and dynamic (b) methods at very low magnification (78×). SEM image (c) and cathodoluminescence (CL) image (d) of the film prepared by the static method at larger magnification (625×). Red color in the CL image represents the 560 nm light (which is emitted from GGAG:Ce) and blue color the 520 nm light (which is emitted mostly by CsPbBr₃).

Figure 6 shows scintillation decay times of CsPbBr₃ films prepared by both methods on GGAG:Ce wafers with comparison to the film prepared by the static method on glass and the pure GGAG:Ce wafer. All the decays were recorded in both short (50 ns, Figure 6a,b) and long (2 μs, Figure 6c) time windows. Decays in the short time window are of great importance for the target application in TOF-PET, because even the fastest sub-nanosecond decay components are well resolved.

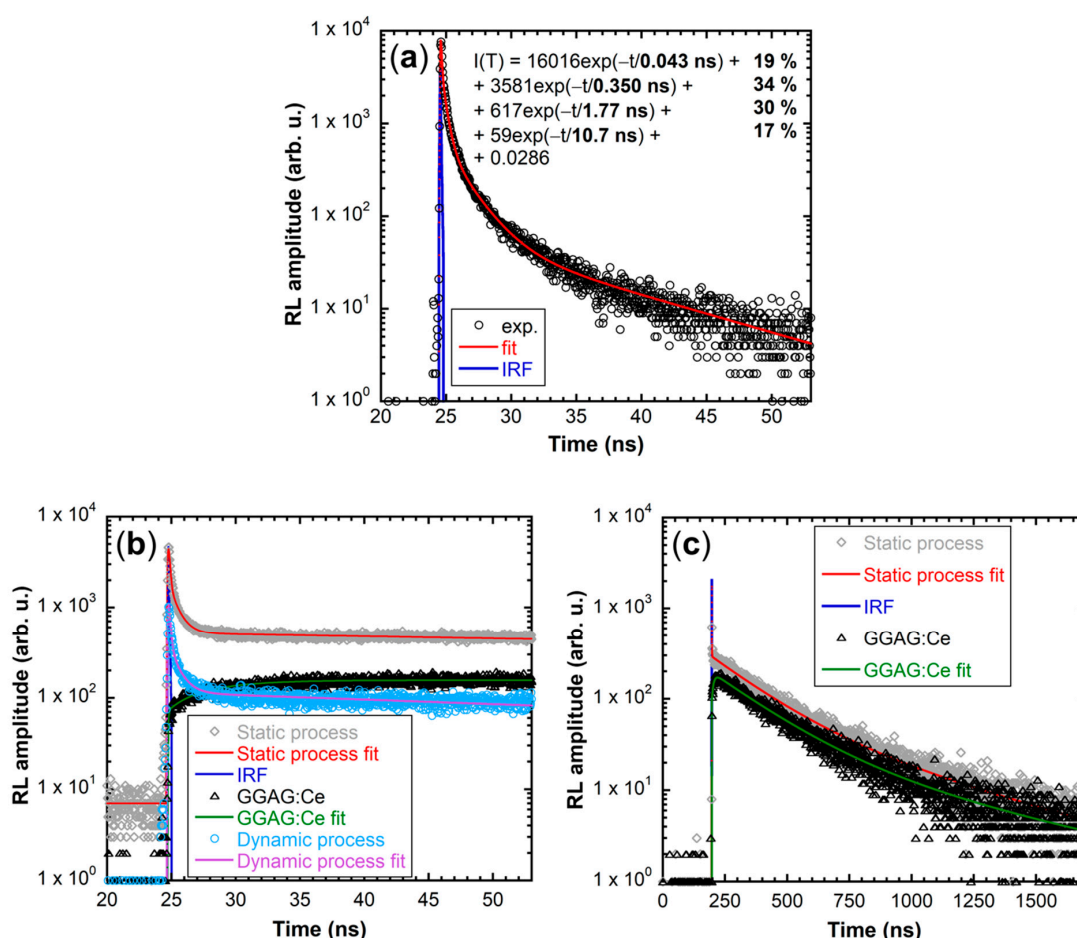


Figure 6. (a) Scintillation decay of the pure CsPbBr₃ film prepared by the static process (50 layers) on glass. (b) Scintillation decays in the short time window of CsPbBr₃ films on GGAG:Ce prepared by the static process (grey diamonds, red line) and the dynamic process (light blue circles, purple line) compared to the scintillation decay of pure GGAG:Ce wafer (black triangles, green line). (c) Scintillation decays in the long time window of the CsPbBr₃ film on GGAG:Ce prepared by the static method (grey diamonds, red line) compared to the scintillation decay of the pure GGAG:Ce (black triangles, green line). Blue line represents the instrumental response function (IRF) in all graphs.

Scintillation decay in the panel (a) in Figure 6 was measured for a qualitative comparison of the pure CsPbBr₃ film on glass to films on GGAG:Ce. It demonstrates the applicability of CsPbBr₃ films as ultrafast scintillators, because more than 50% of the scintillation light is emitted within the sub-nanosecond time gate. Scintillation decays in the panel (b) demonstrate that the ultrafast CsPbBr₃ emission is preserved even if the film is fabricated on the scintillation wafer, as well as the slow emission on GGAG:Ce (this component is resolved only in the long time window in Figure 6c).

The comparison of static and dynamic processes confirms the trend already observable in RL spectra (Figure 4), namely, that the static process results in the film with higher overall RL intensity when combined with the GGAG:Ce scintillator. Similarly as in RL spectra in Figure 4, we also observed significant enhancement of GGAG:Ce emission on the sample prepared by the static process caused by the light-guiding effect on cracks, as discussed above and demonstrated in Figure 5. Interestingly, this enhancement is no longer observable in the sample prepared by the dynamic process. This phenomenon requires more thorough study in the future, but our preliminary conclusion and the answer to our

question is that some level of film homogeneity, which ultimately was not achieved by the dynamic process, is probably needed for the light-guiding effect.

Figure 6c shows the scintillation decay of pure GGAG:Ce compared to the sample prepared by the static process. It displays the long GGAG:Ce decay component and further confirms the enhancement of the GGAG:Ce emission thanks to the CsPbBr₃ film prepared by the static process. Decay of the sample prepared by the dynamic process is not presented because it completely overlaps with both presented decays but can be found in Figure S6 in the Supplementary Information along with the fit parameters of both CsPbBr₃ films on GGAG:Ce.

Summary of the fit rise and decay times can be found in Table 1. Fit parameters of the pure CsPbBr₃ film on glass can be found in Figure 6a.

Table 1. Summary of fit rise times and decay times of pure GGAG:Ce measured in the long time window and CsPbBr₃ films on GGAG:Ce prepared by both static and dynamic processes in the short time window. Long components of GGAG:Ce could not be resolved in the short time window.

Sample	Rise Time	Decay Time	Light Sum
GGAG:Ce	8 ns	200 ns	63%
		660 ns	37%
Static process	50 ps	80 ps	1%
		700 ps	1%
		long	98%
		120 ps	3%
Dynamic process	30 ps	770 ps	2%
		long	95%

4. Conclusions

We prepared CsPbBr₃ films on both the glass and GGAG:Ce scintillating wafers with the target application in TOF-PET. We compared two methods for the film preparation, the static and the dynamic processes. While the dynamic process is more effective in terms of material waste, the static process yields much more homogeneous films. This was found important for the intended application because the sample on GGAG:Ce exhibited higher intensity in RL spectra and especially in scintillation decays.

Moreover, we demonstrated a synergic effect by combining CsPbBr₃ nanoscintillator and GGAG:Ce bulk scintillator. The resulting composite exhibited enhanced RL intensity while preserving the ultrafast CsPbBr₃ decay. Consequently, the thin nanocomposite layer is able to perform as an efficient time tagger in a sampling detector geometry. We can conclude, that presented material combination is indeed a potential candidate in the sandwich detector for ultrafast timing applications, such as TOF-PET.

Supplementary Materials: The following are available online at <https://www.mdpi.com/article/10.3390/nano12010014/s1>, Calculation of the half-value layers, Figure S1: RL spectra of CsPbBr₃ thin films capped with oleic acid and oleylamine on the glass wafer with increasing number of depositions (1–40 layers), Figure S2: RL spectra of CsPbBr₃ thin films capped with didodecyldimethylammonium bromide on the glass wafer with increasing number of depositions (1–40 layers), Figure S3: Linear dependence of the RL intensity in Figure S2 on the number of layers deposited by the static spin-coating process, Figure S4: SEM images of the CsPbBr₃ thin film edge. Sample was prepared on the GGAG:Ce wafer, 50 layers deposited by the static process, Figure S5: SEM images of the CsPbBr₃ thin film edge. Sample was prepared on the GGAG:Ce wafer, 0.6 mL deposited by the dynamic process, Figure S6: Scintillation decays in the long time window of CsPbBr₃ thin films on GGAG:Ce prepared by the static process (left) and the dynamic process (right). Black circles represent experimental data, red line represents the fit and blue line is the instrumental response function (IRF). Reference [29] is cited in the Supplementary Material.

Author Contributions: Conceptualization, V.Č.; Formal analysis, K.D., J.K., F.H., P.P. and V.B.; Funding acquisition, E.M. and V.Č.; Investigation, K.D., J.K., F.H., P.P. and V.B.; Supervision, E.M.

and V.Č.; Visualization, K.D. and J.K.; Writing—original draft, K.D.; Writing—review and editing, K.D., J.K., F.H., P.P., V.B., E.M. and V.Č. All authors have read and agreed to the published version of the manuscript.

Funding: This research was funded by the Czech Science Foundation, grant number GA20-06374S, the Ministry of Education Youth and Sports, project “Center for advanced applied science,” grant number CZ.02.1.01/0.0/0.0/16_019/0000778 and by the Grant Agency of the Czech Technical University in Prague, grant number SGS20/185/OHK4/3T/14.

Institutional Review Board Statement: Not applicable.

Informed Consent Statement: Not applicable.

Data Availability Statement: Data presented in this study are available on request from the corresponding author.

Acknowledgments: We thank Martin Nikl and Pavel Boháček from the Czech Academy of Sciences for providing us GGAG:Ce wafers. This work was carried out in the frame of Crystal Clear Collaboration.

Conflicts of Interest: The authors declare no conflict of interest.

References

- Nikl, M.; Nitsch, K.; Polak, K.; Pazzi, G.P.; Fabeni, P.; Citrin, D.S.; Gurioli, M. Optical properties of the Pb²⁺-based aggregated phase in a CsCl host crystal: Quantum-confinement effects. *Phys. Rev. B* **1995**, *51*, 5192–5199. [[CrossRef](#)]
- Nikl, M.; Nitsch, K.; Mihóková, E.; Polák, K.; Fabeni, P.; Pazzi, G.P.; Gurioli, M.; Santucci, S.; Phani, R.; Scacco, A.; et al. Luminescence of CsPbBr₃-like quantum dots in CsBr single crystals. *Phys. E Low-Dimens. Syst. Nanostruct.* **1999**, *4*, 323–331. [[CrossRef](#)]
- Babin, V.; Fabeni, P.; Nikl, M.; Nitsch, K.; Pazzi, G.P.; Zazubovich, S. Luminescent CsPbI₃ and Cs₄PbI₆ Aggregates in Annealed CsI:Pb Crystals. *Phys. Status Solidi* **2001**, *226*, 419–428. [[CrossRef](#)]
- Protesescu, L.; Yakunin, S.; Bodnarchuk, M.I.; Krieg, F.; Caputo, R.; Hendon, C.H.; Yang, R.X.; Walsh, A.; Kovalenko, M.V. Nanocrystals of Cesium Lead Halide Perovskites (CsPbX₃, X = Cl, Br, and I): Novel Optoelectronic Materials Showing Bright Emission with Wide Color Gamut. *Nano Lett.* **2015**, *15*, 3692–3696. [[CrossRef](#)]
- Song, J.; Li, J.; Li, X.; Xu, L.; Dong, Y.; Zeng, H. Quantum Dot Light-Emitting Diodes Based on Inorganic Perovskite Cesium Lead Halides (CsPbX₃). *Adv. Mater.* **2015**, *27*, 7162–7167. [[CrossRef](#)] [[PubMed](#)]
- Wang, Y.; Zhang, T.; Kan, M.; Zhao, Y. Bifunctional Stabilization of All-Inorganic α -CsPbI₃ Perovskite for 17% Efficiency Photovoltaics. *J. Am. Chem. Soc.* **2018**, *140*, 12345–12348. [[CrossRef](#)]
- Swarnkar, A.; Chulliyil, R.; Ravi, V.K.; Irfanullah, M.; Chowdhury, A.; Nag, A. Colloidal CsPbBr₃ Perovskite Nanocrystals: Luminescence beyond Traditional Quantum Dots. *Angew. Chem. Int. Ed.* **2015**, *54*, 15424–15428. [[CrossRef](#)]
- Gandini, M.; Villa, I.; Beretta, M.; Gotti, C.; Imran, M.; Carulli, F.; Fantuzzi, E.; Sassi, M.; Zaffalon, M.; Brofferio, C.; et al. Efficient, fast and reabsorption-free perovskite nanocrystal-based sensitized plastic scintillators. *Nat. Nanotechnol.* **2020**, *15*, 462–468. [[CrossRef](#)]
- Zhang, Y.; Sun, R.; Ou, X.; Fu, K.; Chen, Q.; Ding, Y.; Xu, L.-J.; Liu, L.; Han, Y.; Malko, A.V.; et al. Metal Halide Perovskite Nanosheet for X-ray High-Resolution Scintillation Imaging Screens. *ACS Nano* **2019**, *13*, 2520–2525. [[CrossRef](#)]
- Chen, Q.; Wu, J.; Ou, X.; Huang, B.; Almutlaq, J.; Zhumekenov, A.A.; Guan, X.; Han, S.; Liang, L.; Yi, Z.; et al. All-inorganic perovskite nanocrystal scintillators. *Nature* **2018**, *561*, 88–93. [[CrossRef](#)] [[PubMed](#)]
- Mykhaylyk, V.B.; Kraus, H.; Kapustianyk, V.; Kim, H.J.; Mercere, P.; Rudko, M.; Da Silva, P.; Antonyak, O.; Dendebera, M. Bright and fast scintillations of an inorganic halide perovskite CsPbBr₃ crystal at cryogenic temperatures. *Sci. Rep.* **2020**, *10*, 8601. [[CrossRef](#)]
- Li, Y.; Shao, W.; Chen, L.; Wang, J.; Nie, J.; Zhang, H.; Zhang, S.; Gao, R.; Ouyang, X.; Ouyang, X.; et al. Lead-halide Cs₄PbBr₆ single crystals for high-sensitivity radiation detection. *NPG Asia Mater.* **2021**, *13*, 40. [[CrossRef](#)]
- Moseley, O.D.I.; Doherty, T.A.S.; Parmee, R.; Anaya, M.; Stranks, S.D. Halide perovskites scintillators: Unique promise and current limitations. *J. Mater. Chem. C* **2021**, *9*, 11588–11604. [[CrossRef](#)]
- Yang, H.; Li, H.; Yuan, R.; Chen, J.; Zhao, J.; Wang, S.; Liu, Y.; Li, Q.; Zhang, Z. A novel scintillation screen for achieving high-energy ray detection with fast and full-color emission. *J. Mater. Chem. C* **2021**, *9*, 7905–7909. [[CrossRef](#)]
- Maddalena, F.; Xie, A.; Chin, X.Y.; Begum, R.; Witkowski, M.E.; Makowski, M.; Mahler, B.; Drozdowski, W.; Springham, S.V.; Rawat, R.S.; et al. Deterministic Light Yield, Fast Scintillation, and Microcolumn Structures in Lead Halide Perovskite Nanocrystals. *J. Phys. Chem. C* **2021**, *125*, 14082–14088. [[CrossRef](#)]
- Liu, C.; Li, Z.; Hajagos, T.J.; Kishpaugh, D.; Chen, D.Y.; Pei, Q. Transparent Ultra-High-Loading Quantum Dot/Polymer Nanocomposite Monolith for Gamma Scintillation. *ACS Nano* **2017**, *11*, 6422–6430. [[CrossRef](#)] [[PubMed](#)]

17. Turtos, R.M.; Gundacker, S.; Omelkov, S.; Mahler, B.; Khan, A.H.; Saaring, J.; Meng, Z.; Vasil'ev, A.; Dujardin, C.; Kirm, M.; et al. On the use of CdSe scintillating nanoplatelets as time taggers for high-energy gamma detection. *Npj 2D Mater. Appl.* **2019**, *3*, 37. [[CrossRef](#)]
18. Lecoq, P.; Morel, C.; Prior, J.O.; Visvikis, D.; Gundacker, S.; Auffray, E.; Križan, P.; Turtos, R.M.; Thers, D.; Charbon, E.; et al. Roadmap toward the 10 ps time-of-flight PET challenge. *Phys. Med. Biol.* **2020**, *65*, 21RM01. [[CrossRef](#)]
19. Kamada, K.; Kurosawa, S.; Prusa, P.; Nikl, M.; Kochurikhin, V.V.; Endo, T.; Tsutsumi, K.; Sato, H.; Yokota, Y.; Sugiyama, K.; et al. Cz grown 2-in. size Ce:Gd₃(Al,Ga)₅O₁₂ single crystal; Relationship between Al, Ga site occupancy and scintillation properties. *Opt. Mater.* **2014**, *36*, 1942–1945. [[CrossRef](#)]
20. Yokota, Y.; Kudo, T.; Ohashi, Y.; Kurosawa, S.; Kamada, K.; Zeng, Z.; Kawazoe, Y.; Yoshikawa, A. Effects of dopant distribution improvement on optical and scintillation properties for Ce-doped garnet-type single crystals. *J. Mater. Sci. Mater. Electron.* **2017**, *28*, 7151–7156. [[CrossRef](#)]
21. Lu, C.; Wright, M.W.; Ma, X.; Li, H.; Itanze, D.S.; Carter, J.A.; Hewitt, C.A.; Donati, G.L.; Carroll, D.L.; Lundin, P.M.; et al. Cesium Oleate Precursor Preparation for Lead Halide Perovskite Nanocrystal Synthesis: The Influence of Excess Oleic Acid on Achieving Solubility, Conversion, and Reproducibility. *Chem. Mater.* **2019**, *31*, 62–67. [[CrossRef](#)]
22. Děcká, K.; Suchá, A.; Král, J.; Jakubec, I.; Nikl, M.; Jarý, V.; Babin, V.; Mihóková, E.; Čuba, V. On the role of Cs₄PbBr₆ phase in the luminescence performance of bright CsPbBr₃ nanocrystals. *Nanomaterials* **2021**, *11*, 1935. [[CrossRef](#)] [[PubMed](#)]
23. Imran, M.; Ijaz, P.; Goldoni, L.; Maggioni, D.; Petralanda, U.; Prato, M.; Almeida, G.; Infante, I.; Manna, L. Simultaneous cationic and anionic ligand exchange for colloiddally stable CsPbBr₃ nanocrystals. *ACS Energy Lett.* **2019**, *4*, 819–824. [[CrossRef](#)]
24. Maes, J.; Balcaen, L.; Drijvers, E.; Zhao, Q.; De Roo, J.; Vantomme, A.; Vanhaecke, F.; Geiregat, P.; Hens, Z. Light Absorption Coefficient of CsPbBr₃ Perovskite Nanocrystals. *J. Phys. Chem. Lett.* **2018**, *9*, 3093–3097. [[CrossRef](#)]
25. Jing, Q.; Xu, Y.; Su, Y.; Xing, X.; Lu, Z. A systematic study of the synthesis of cesium lead halide nanocrystals: Does Cs₄PbBr₆ or CsPbBr₃ form? *Nanoscale* **2019**, *11*, 1784–1789. [[CrossRef](#)]
26. Cao, F.; Yu, D.; Xu, X.; Han, Z.; Zeng, H. CsPbBr₃@Cs₄PbBr₆ Emitter-in-Host Composite: Fluorescence Origin and Interphase Energy Transfer. *J. Phys. Chem. C* **2021**, *125*, 3–19. [[CrossRef](#)]
27. Prusa, P.; Nikl, M.; Mares, J.A.; Kucera, M.; Nitsch, K.; Beitlerova, A. The α -particle excited scintillation response of YAG:Ce thin films grown by liquid phase epitaxy. *Phys. Status Solidi Appl. Mater. Sci.* **2009**, *206*, 1494–1500. [[CrossRef](#)]
28. Salomoni, M.; Pots, R.; Auffray, E.; Lecoq, P. Enhancing light extraction of inorganic scintillators using photonic crystals. *Crystals* **2018**, *8*, 78. [[CrossRef](#)]
29. Berger, M.J.; Hubbell, J.H.; Seltzer, S.M.; Chang, J.; Coursey, J.S.; Sukumar, R.; Zucker, D.S.; Olsen, K. *XCOM: Photon Cross Section Database (Version 1.5)*; National Institute of Standards and Technology: Gaithersburg, MD, USA, 2010. Available online: <http://physics.nist.gov/xcom> (accessed on 9 November 2021).

Cite this: DOI: 00.0000/xxxxxxxxxx

Timing performance of lead halide perovskite nanoscintillators embedded in polystyrene matrix[†]

Kateřina Děcká,^{a,b} Fiammetta Pagano,^{*c,d} Isabel Frank,^{c,e} Nicolaus Kratochwil,^c Eva Mihóková,^{a,b} Etienne Auffray^c and Václav Čuba^a

Received Date
Accepted Date

DOI: 00.0000/xxxxxxxxxx

Nanomaterials like CsPbBr₃, benefiting from quantum confinement effects to feature ultra-fast decay time and tunable emission, are paving the way for the next generation of fast timing detectors. However, an ongoing challenge is to exploit their favorable properties in a full detector, given their size and instability. Embedding halide perovskite nanocrystals in solid matrices like organic polymers can provide the required stability and, in the case of high nanoparticle filling factor with little aggregation, results in a flexible scintillator featuring sub-ns decay times.

In this work, we present the production, characterization, and - for the first time - time resolution measurements of CsPbBr₃ nanocrystals embedded in polystyrene, using two different surface ligands (OA+OAm, DDAB) and three different filling factors of up to 10 %.

The samples were characterized by spectroscopic methods, namely photo- and radio-luminescence as well as transmittance, while scintillation decay kinetics was measured in a time correlated single photon counting setup upon X-ray excitation. The characterization results suggest that, for both ligands, a 10 % filling factor with little to no aggregation can be manufactured.

In addition, the time resolution of these materials was measured with a novel setup coupled to analog Silicon Photomultipliers and low energy pulsed X-ray excitation. When comparing with the state of the art inorganic (LYSO:Ce) crystal, more than twofold time resolution improvement was obtained, despite the lower light transport and small energy deposition. These first promising results represent the starting point for the optimization of CsPbBr₃ nanocrystals embedded in polymer matrices and their application in fast timing detectors for TOF-CT, TOF-PET and high energy physics.

1 Introduction

Lead halide perovskite nanocrystalline phosphors with the formula CsPbX₃ (X = Cl, Br, I) have captured significant attention of the scientific community in the last few years, mostly due to their high light output, fast decay times, and narrow, tunable emission bands with wide application potential in optoelectronics^[1,4]. Recently, the attention shifted toward their implementation as scintillation detectors as well^[5,10], specifically for fast timing applications. Indeed, the capability of ultra-fast detection of X-rays, 511 keV gamma-rays, and high energy particles has triggered in-

terest in high energy physics^[11,12] and medical imaging applications, such as time-of-flight positron emission tomography (TOF-PET)^[13,14] and computed tomography (TOF-CT)^[15]. Among many concepts to boost the production of ultra-fast photons - such as Cherenkov emission^[16], hot intraband luminescence^[17], or cross-luminescence^[18] - quantum confinement effects in nanocrystals result in a unique combination of fast emission with relatively high light output^[10,19,20]. As a rough estimate, the timing capability of a material scales with the square root of the ratio of effective decay time and light output^[21], justifying the increasing interest in nanocrystalline materials as ultra-fast radiation detectors.

Despite their excellent fast emission, several drawbacks have to be addressed for halide perovskite nanocrystals to be effectively used as radiation detectors. Among them, limited stability against air moisture and oxygen^[22] and nanometer size, with consequent low energy deposition upon particle interaction, are the main ones. Both issues can be partially overcome by the immobilization of nanocrystals in solid matrices such as glass or organic polymers, or in other composites such as silica/alumina monolith^[23]. The first two techniques are already well established: glass

^a Faculty of Nuclear Sciences and Physical Engineering, Czech Technical University in Prague, Břehová 7, 115 19 Prague, Czech Republic

^b Institute of Physics of the Czech Academy of Sciences, Cukrovarnická 10, 162 53 Prague, Czech Republic

^c CERN, Esplanade des Particules 1, 1211 Meyrin, Switzerland

^d Università degli Studi Milano Bicocca, Piazza dell'Ateneo Nuovo, 1-20126 Milano, Italy

^e LMU Munich, Geschwister-Scholl-Platz 1, 80539 Munich, Germany

* Corresponding author, E-mail: fiammetta.pagano@cern.ch

[†] Electronic Supplementary Information (ESI) available: [Supplementary Material]. See DOI: 00.0000/00000000.

matrices guarantee better radiation hardness^[24,25], while polymer matrices are much more cost-effective. Further, the applicability of CsPbBr₃ embedded in polystyrene has already been demonstrated, with encouraging results about radiation hardness as well.^[6] The main drawback of polymer matrices for ionizing radiation detectors is the low stopping power, but the incorporation of dense nanocrystals, such as CsPbBr₃, will automatically enhance it. Moreover, concerning TOF-PET applications, encouraging results on heterostructured scintillators made of alternating layers of a dense inorganic material (e.g. BGO whose density is 7 g/cm³) and fast organic polymers (e.g. BC422 and EJ232 whose decay time is about 1.5 ns) have been published in the last years^[26,28]. Lead halide perovskites embedded in polystyrene constitute an alternative candidate as fast material for heterostructures with potentially better time resolution than BC422 or EJ232 as a result of faster scintillation decay kinetics and higher light yield (about 24 ph/keV^[29] instead of 8.4 ph/keV^[30]).

This study represents the first step toward the characterization and development of lead halide perovskites based scintillator suitable for radiation detectors. For the first time, we provide time resolution measurements of nanocrystal based samples upon pulsed X-ray irradiation. While the scintillation decay kinetics of these samples was already accessible using laser or X-ray irradiation, the time resolution measurements are investigating a different physical quantity; it encompasses not only the simple scintillation decay kinetics, but also the scintillation light yield^[21,31]. The coincidence time resolution (CTR) is already an established quantity usually measured using higher energy sources, like ²²Na emitting 511 keV γ -rays. Due to low detection efficiency, the standard characterization procedure is not possible for these samples, therefore we used a novel experimental setup^[32,33] allowing to measure the time resolution of scintillators upon low energy (about 10 keV) X-ray irradiation.

In this study, we explore CsPbBr₃ nanocrystals capped with different surface ligands embedded in a polystyrene matrix with various weight filling factors (up to 10%). The chosen ligands were the standard combination of oleic acid and oleylamine (OA+OAm) and DDAB (didodecyldimethylammonium bromide), which was reported to exhibit better surface passivation capability compared to OA+OAm, resulting in higher light yields of CsPbBr₃ nanocrystals^[34,35]. We characterize them focusing on their potential for fast timing applications. Therefore, we provide time resolution measurements upon X-ray excitation and discuss integration aspects for the applicability as radiation detectors.

2 Experimental section

2.1 CsPbBr₃@PS composite fabrication

CsPbBr₃ nanocrystals were synthesized using the standard hot injection procedure^[4]. DDAB capped nanocrystals were prepared by a ligand exchange method. The size of nanocrystals used for the nanocomposite fabrication was determined to be 10 ± 1 nm. For more information, please refer to the Electronic Supplementary Information (ESI) †.

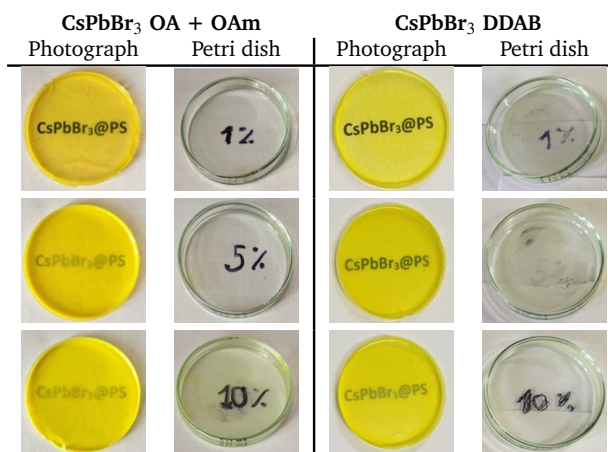
For the polystyrene (PS) nanocomposite samples, about 210 mg of PS pellets were dissolved in toluene in a Petri dish of 5 cm

diameter. Then, the calculated amount of CsPbBr₃ solution was pipetted to achieve the desired final concentration in PS, namely 1%, 5%, and 10%. For example, for 1% filling factor, 40 μ L of 52.5 mg/mL CsPbBr₃ solution was pipetted. The viscous solution was thoroughly mixed until homogenized completely. Finally, the toluene was left to evaporate in air at room temperature. After one week, the already solid samples were taken out of the Petri dishes and the residual toluene was left to evaporate in air at room temperature for another week.

Before characterization, all samples were cleaned with cellulose swab soaked in hexane, finally resulting in 5 cm diameter discs with a thickness of 100 μ m, as measured by a caliper with 20 μ m resolution.

Ultimately, two sets of samples were obtained, each with three different filling factors - 1%, 5%, and 10% - giving a total of six samples. In the first set CsPbBr₃ nanocrystals were capped with oleic acid and oleylamine (OA+OAm), while in the second one the nanoparticles were capped with DDAB. All samples are summarized and shown in Table 1. Note that the transparency is good even for 10% filling.

Table 1 Photographs of the samples and their respective Petri dishes after removing the sample.



2.2 Characterization

Before embedding CsPbBr₃ nanocrystals in the polystyrene matrix, X-ray powder diffraction, PL, and RL spectra were measured. After the embedding, RL, and transmission spectra, as well as scintillation decay kinetics and time resolution under X-ray excitation were measured for all samples.

X-ray powder diffraction (XRPD) was measured using a Rigaku Miniflex 600 diffractometer equipped with a Cu X-ray tube ($K_{\alpha 1,2}$ average wavelength 0.15418 nm, voltage 40 kV, current 15 mA). Data were collected with a speed of 2°/min and compared with the ICDD PDF-2 database, version 2013. The Halder-Wagner method with the Scherrer constant value of 0.94 was used to determine the linear crystallite size.

Transmission spectra, PL excitation, and emission spectra were collected using a FluoroMax spectrofluorometer (Horiba Jobin

Yvon). RL spectra were collected using a 5000M spectrofluorometer (Horiba Jobin Yvon) with a monochromator, a TBX-04 (IBH Scotland) photodetector, and a Seifert X-ray tube (40 kV, 15 mA) as an excitation source.

The decay time was measured in time correlated single photon counting (TCSPC) mode³⁶. The samples were excited with a Hamamatsu pulsed X-ray tube and the emission light was collected by a Hybrid Photomultiplier Tube (HPMT). The overall instrumental response function (IRF), which takes into account the HPMT together with the laser used to excite the X-ray tube and the tube itself, was estimated to be 160 ps full-width-at-half-maximum (FWHM). To select only the perovskite emission, a bandpass filter centered at 530 nm with 40 nm FWHM was used.

The scintillation decays were fitted with the convolution of the system IRF and the intrinsic scintillation decay function. Since a (semi-)prompt component was observed for all samples, we decided to model the intrinsic scintillation function as the sum of three exponential functions and a Dirac-delta function, in analogy to what was done in³⁷ to model Cherenkov photons. Before opting for this model, others were tested using only exponential components (between two and five). However, these did not properly account for the ultra-fast decay component, which is the one of utmost importance for fast timing radiation detectors. We finally chose the model that allowed us to fit all the samples well enough, particularly in the fastest part of the decay, while maintaining the lowest number of components. In the fit procedure, the rise-time was fixed at 0 ps since it was well below the time resolution of the system. This allowed better stability of the fit for the decay part.

The detector time resolution (DTR) - also known as single time resolution (STR), as opposed to coincidence time resolution (CTR) which takes into account a pair of detectors - was measured with a novel experimental setup using low energy X-ray irradiation developed purposely for the characterization of low-stopping power scintillators^{32,33}. The setup includes a Hamamatsu pulsed X-ray tube, excited by a picosecond diode laser whose external trigger is used as the start signal for the DTR measurement. The stop signal instead is given by the output of the SiPM, used for collecting the scintillation light emitted by the sample following the X-ray excitation. The DTR was evaluated as the FWHM of the time delay (time difference between start and stop) peak.

For these measurements, $3 \times 3 \text{ mm}^2$ plates were cut from the 5 cm discs to match the active area of the SiPM ($3 \times 3 \text{ mm}^2$, S13360-3050CS from Hamamatsu), operated about 10 V above the breakdown voltage. The optical coupling was done with Meltmount glue (refractive index $n = 1.58$) and no reflective material was used to wrap the samples to avoid X-ray absorption from this material.

3 Results

3.1 Transmission

CsPbBr₃ samples capped with DDAB have generally better transparency, as visible in the photographs in Table 1 and then confirmed by transmission spectra shown in Figure 1 (OA+OAm (a) DDAB (c)). CsPbBr₃@PS (1%) capped with OA and OAm have

50% transmittance at 800 nm, while CsPbBr₃@PS (1%) capped with DDAB have 56% transmittance. The difference is even more pronounced for higher filling factors, as it can be observed in Figure 1(a,c).

From Figure 1(a,c), it is also clear that samples with 1% filling factor have good transparency even at lower wavelengths than the absorption edge of CsPbBr₃ (around 510–530 nm), unlike those with higher filling factors.

3.2 Radioluminescence

Figure 1(b,d) shows the RL spectra of the two sets of samples. The RL intensity - calculated by integrating the spectrum between 470–630 nm - of the OA+OAm 10% sample is $2\times$ higher compared to the OA+OAm 5% sample, while the intensity of the DDAB 10% sample is $2.5\times$ higher compared to the corresponding 5% sample.

The positions of RL emission bands were obtained by fitting the curve around its maximum with a quadratic function to reduce the effect of noise. The errors were estimated by taking into account both the precision of the chosen fitting procedure and the systematic error of the setup. For more details and examples of such curves, see Figure S3 in ESI †.

The positions of RL emission bands of samples with higher filling factors are increasingly red-shifted from $528 \pm 1 \text{ nm}$ for 1% filling factor up to $533 \pm 0.5 \text{ nm}$ for the 10% filling factor using OA+OAm ligands and from $526 \pm 1 \text{ nm}$ (1% filling factor) to $531 \pm 0.5 \text{ nm}$ (10% filling factor) using the DDAB ligand. This red-shift is even more pronounced in the PL emission, as shown in Figure S4 in ESI †.

All samples have very weak emission centered at 325 nm which originates from the polystyrene itself, as shown by the $\times 100$ magnification in Figure 1(b,d).

The samples were stored at ambient conditions and the RL spectra were measured three times over the course of one month. No significant changes in the RL intensity were observed (see Figure S5 in ESI †).

3.3 Decay time under X-ray excitation

Figure 2 shows an example of a measured scintillation decay together with its fit. The fitted scintillation decays of all six samples can be found in the ESI † (see Figure S6 and Figure S7). The results are summarized in Table 2. For all samples, we observe an ultra-fast decay time component (modeled with a Dirac-delta function) of about 20% weight and another sub-ns decay time component, also with around 20% contribution. Those ultra-fast decay time components are of utmost importance to boost the timing capability of the material. For samples belonging to the OA+OAm set, it can be observed that the slowest decay component (τ_{d3}) and its corresponding weight (R_3) progressively increase together with the filling factor, at the expense of the fastest exponential decay component (τ_{d1}). On the contrary, for the DDAB samples, no clear trend is observable.

The effective decay time ($\tau_{d,eff}$), defined as the weighted harmonic mean of the exponential components, was chosen as figure of merit to summarize the three exponential decay components

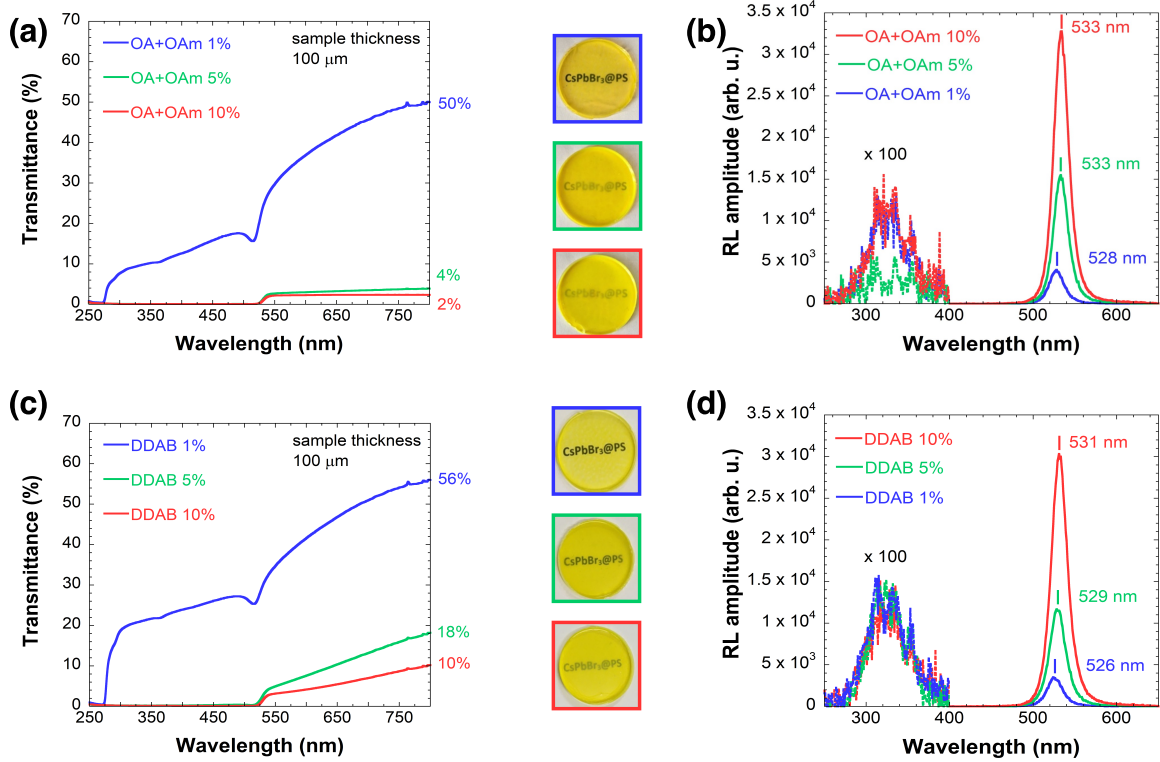


Fig. 1 (a) Transmission spectra and (b) RL spectra of samples from the OA+OAm set, (c) transmission spectra and (d) RL spectra of samples from the DDAB set, with various filling factors. Blue, green and red lines represent 1%, 5% and 10% filling factors, respectively. The RL spectra were multiplied by the factor of 100 in the interval 250 nm – 400 nm to reveal the weak polystyrene emission.

Table 2 Fit results of all scintillation decays. G is the weight of the delta function used to model the ultra-fast component, τ_{d1} , τ_{d2} and τ_{d3} are the exponential decay components with the respective weights (R_1 , R_2 and R_3), and $\tau_{d,eff}$ is the effective decay time.

Sample		τ_{d1} [ns]	R_1 [%]	τ_{d2} [ns]	R_2 [%]	τ_{d3} [ns]	R_3 [%]	G [%]	$\tau_{d,eff}^1$ [ns]
O A + O A m	1%	0.76 ± 0.02	24 ± 4	3.0 ± 0.3	27 ± 3	11 ± 1	31 ± 7	18 ± 2	1.9 ± 0.2
	5%	0.68 ± 0.02	18 ± 3	3.4 ± 0.3	30 ± 4	18 ± 2	28 ± 5	24 ± 3	2.0 ± 0.2
	10%	0.69 ± 0.02	14 ± 2	4.1 ± 0.4	28 ± 4	26 ± 3	42 ± 7	16 ± 2	2.9 ± 0.3
D D A B	1%	0.92 ± 0.03	18 ± 3	3.9 ± 0.4	29 ± 4	21 ± 3	37 ± 7	16 ± 2	2.9 ± 0.3
	5%	0.79 ± 0.02	17 ± 3	3.5 ± 0.3	35 ± 4	18 ± 2	28 ± 5	20 ± 2	2.4 ± 0.2
	10%	0.79 ± 0.02	17 ± 3	3.9 ± 0.4	27 ± 3	15 ± 2	36 ± 6	20 ± 2	2.6 ± 0.2

¹ The fit function was normalized so that the weights of the four components add up to one ($\sum_{i=1}^3 R_i + G = 1$), but the effective decay time was calculated with re-normalized ratio: $R_{n,i} = \frac{R_i}{\sum_i R_i}$ and $\frac{1}{\tau_{d,eff}} = \sum_i \frac{\tau_{d,i}}{R_{n,i}}$.

in only one parameter, simplifying the comparison between the samples²¹. The obtained values are reported in the last column of Table² and confirm what was previously observed. For this calculation, a re-normalization was applied to omit the almost prompt contribution for better comparison. For a final evaluation, both parameters $\tau_{d,eff}$ and G, the weight of prompt component, need to be considered simultaneously.

3.4 Time resolution under X-ray excitation

Time resolution results are presented in Table³. One can observe that overall, the samples capped with DDAB showed slightly bet-

ter timing capability. The time delay distribution of all samples can be consulted in the ESI[†] (see Figure^{S8}).

To give a better idea about the timing performance of this material, a comparison with two well-known scintillators - LYSO:Ce and EJ232 plastic scintillator - with similar geometry ($3 \times 3 \times 0.2 \text{ mm}^3$) is shown as well in Table³. LYSO:Ce was chosen as the state-of-the-art inorganic scintillator for TOF-PET: it has high density and high effective atomic number (7.1 g/cm^3 and 66, respectively), hence good stopping power and photofraction, intrinsic light yield of about 40 ph/keV, and effective decay time of about 40 ns²¹. On the other hand, EJ232 was chosen as an ultra-fast plastic scintillator: it shows similar properties to BC422

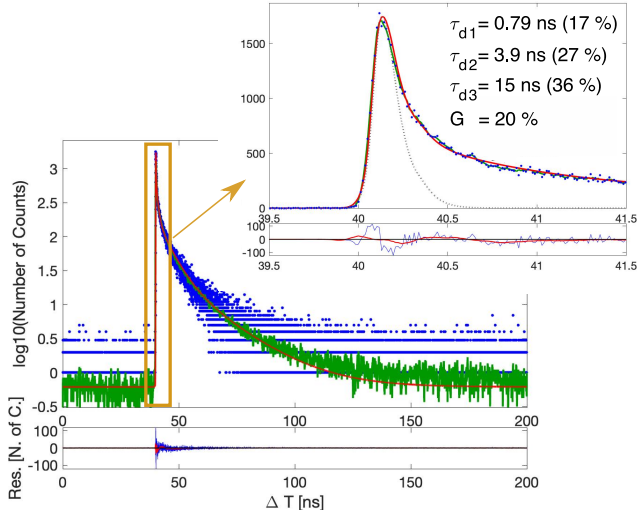


Fig. 2 Scintillation decay of CsPbBr₃ 10% sample capped with DDAB. The scintillation decay is shown in semi-logarithmic scale over the whole range (≈ 150 ns). The blue dots are the measured data points, the green line is their average, and the red curve is the fit function. Inset: detail of the ultra-fast component in linear scale. The dotted gray line represents the system IRF.

Table 3 Measured DTR values of all six samples, compared to those of EJ232 and LYSO:Ce.

Filling Factor	DTR (FWHM) [ps]	
	OA + OAm	DDAB
1 %	305 \pm 9	308 \pm 9
5 %	330 \pm 10	309 \pm 9
10 %	319 \pm 9	295 \pm 8
LYSO:Ce	695 \pm 21	
EJ232	332 \pm 10	

plastic scintillator (effective decay-time of ≈ 1.7 ns, rise time of ≈ 35 ps, intrinsic light yield of about 10 ph/keV^[21]) but it can be produced in very thin layers with better surface state. For the aforementioned reasons, EJ232 is one of the favorite materials in preliminary studies^[27,28] about heterostructures.

The respective time delay distribution is shown in Figure 3 in comparison to the best performing CsPbBr₃ sample (10% filling factor, DDAB set). All CsPbBr₃ samples perform twofold better than LYSO:Ce and similarly or slightly better than EJ232. This is explained by the scintillation decay kinetics of the considered samples (1.5 ns effective decay time for CsPbBr₃ samples and EJ232 instead of 40 ns for LYSO) and by the low irradiation energy.

4 Discussion

Two sets of CsPbBr₃@PS samples with various nanocrystal filling factors were prepared. One set using CsPbBr₃ nanocrystals capped with OA+OAm (OA+OAm set), the second set using CsPbBr₃ capped with DDAB after the ligand exchange procedure (DDAB set). First, free nanocrystals were characterized (XRPD,

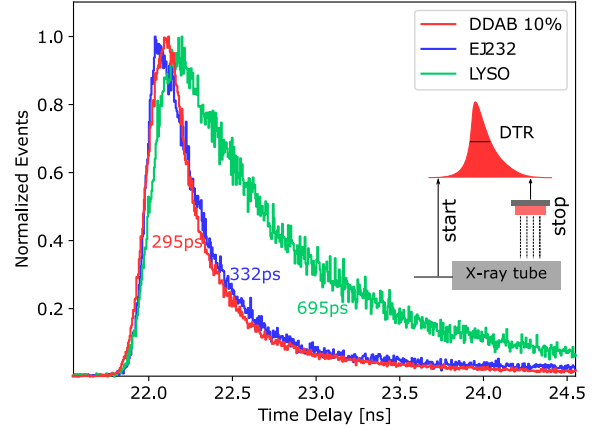


Fig. 3 Comparison of the time delay distribution for the CsPbBr₃ 10% sample capped with DDAB (red) and standard scintillators EJ232 (blue) and LYSO (green). Inset: sketch of the measurement condition of pulsed X-ray tube exciting the tested sample and the evaluation of the DTR from the time difference of start and stop signal.

PL and RL spectra) then transparency, RL emission spectra, decay times, and time resolution of fabricated nanocomposites of CsPbBr₃ in polystyrene of both sets were determined.

4.1 Basic optical characterization

Generally, samples from the DDAB set exhibited superior transparency compared to those from the OA+OAm set. Together with the fact that 10% filling factor was achieved only in this set (c. f. the CsPbBr₃ residue in the 10% OA+OAm sample Petri dish in Table 1), we conclude that also for the embedding, the DDAB ligand is a better choice than the standard OA+OAm combination. Since already 10% filling factor could not be achieved completely in the OA+OAm set, we did not explore higher filling factors in this study.

The better transparency of the DDAB set is probably a result of its better surface passivation capability. By careful analysis of the scintillation decay components in Table 2 we concluded that it effectively suppresses aggregation, because no trend of gradually slower decay times was observed in this set. On the contrary, in the OA+OAm set we observed this trend in the third exponential decay component τ_{d3} . We reason that when larger crystals are formed by aggregation, the scintillation response is slowed down due to the quantum confinement effect.

However, since the transparency of the samples from the DDAB set still decreases slightly with increasing filling factor, we expect that clustering occurs to some extent in this set. We distinguish the simple *clustering* - i.e. nanocrystals forming larger clusters but preserving their shape and size - from the real *aggregation* - i.e. nanocrystals forming bigger particles with their neighbors. Naturally, the aggregation can be understood as an extreme case of simple clustering (first, nanocrystals undergo the clustering process and then the aggregation may occur). As a result of this phenomenon, we observe a gradual speed-up of scintillation response in the first exponential decay component τ_{d1} . This is probably

caused by increased self-absorption and subsequent luminescence quenching within those clusters (a similar trend is also observed in the OA+OAm set).

Both phenomena could have caused the observed red-shifts in the RL spectra; both the formation of larger nanocrystals by aggregation and the increased self-absorption within the clusters can result in this shift. Since this article is mainly focused on the timing capability of the produced samples, a more in-depth discussion of all the above-mentioned phenomena and observed red-shifts in the RL spectra can be found in the ESI[†] (Section S3).

4.2 Timing performance

Timing performance of the prepared nanocomposite samples is the crucial characteristic for the target application. TCSPC measurements revealed the ultra-fast scintillation decay kinetics of these samples: in all of them we observed a (semi-)prompt component which has been modeled with a Dirac-delta function, and a second sub-nanosecond component (between 700 and 900 ps). Summing up the contributions, almost 50% of light is emitted within the first nanosecond. This contributes to the increasing in the initial photon time density, which, taking into account both scintillation decay kinetics and intrinsic light yield, is the main contribution to time resolution²¹. The presence of the ultrafast components can be explained by luminescence quenching or the formation of biexcitons^{38,40}.

The ultra-fast decay kinetics of these samples explains the two-fold better time resolution of CsPbBr₃@PS compared to LYSO at 10 keV. This is a significant result since LYSO is the currently used scintillator in commercial TOF-PET scanners. Our nanocomposite is therefore a viable candidate for fast timing applications.

Since LYSO is a high density crystal, we also compared the timing performances of CsPbBr₃@PS to EJ232 plastic scintillator, being one of the favorite options as fast material for heterostructured scintillators which we aim to substitute with CsPbBr₃@PS. CsPbBr₃@PS proved to have even faster decay kinetics than EJ232 (similar effective decay time but with a more significant contribution from the prompt component, see Table 2), nevertheless, at this moment, the time resolution improvement with respect to EJ232 is not significant. This is probably due to less efficient energy conversion as a result of still too low filling factor. Despite the similar density and atomic number of the two samples, the polymer matrix of CsPbBr₃@PS does not contribute to the overall scintillation intensity significantly. Therefore, scintillating photons are produced almost exclusively when X-rays interact directly with nanocrystals, and with filling factors between 1 and 10% the probability for this happening is quite low. Such a not-optimized energy conversion further results in a lower number of produced photons and typically the timing capability scales with the inverse square root of the light yield.

Comparing the time resolution of all synthesized samples, no significant difference was observed with increasing filling factor, for either of the two sets. These results can give some insight into the effective light output of these samples with increasing filling factor. From the optical measurements, we saw that samples with higher filling factor show higher PL and RL, but also significantly

lower transmittance. The absence of a clear trend in DTR with the filling factor suggests that these two effects balance each other. This also suggests that an optimum could exist, and it will be investigated in future studies with a denser scan of filling factors. Moreover, future experiments will be also dedicated to achieving higher filling factors while maintaining as good transparency of the nanocomposites as possible.

Comparing the time resolution of the two sets, samples from the DDAB one resulted to perform slightly better, in agreement with previously discussed results on the optical properties of these samples.

4.3 Applications and Outlook

From an application point of view, even a time resolution in the order of 300 ps will reduce the amount of scattered photons for TOF-CT. While in this study a pulsed X-ray tube with a mean energy of 10 keV was used, for X-ray and CT examinations typically higher energies are used (20-120 keV). To put the measured time resolution into perspective, already at 90 keV sub-100 ps ($295 \text{ ps} \cdot \sqrt{\frac{10 \text{ keV}}{90 \text{ keV}}}$) time resolution can be expected. Such a value allows to remove most of the scattered photons for TOF-CT and thus results in better image quality³² or a lower required dose for the same examination.

A corresponding calculation can be done for TOF-PET working with 511 keV gamma-rays. Selecting at the 340 keV Compton edge, a coincidence time resolution of 35 ps FWHM is reported with a bulk plastic scintillator which is similar to the used EJ232⁴¹. Such simple approximations highlight the promising R&D avenue of lead halide perovskite nanocrystals, in line with the ongoing 10 ps challenge for TOF-PET¹⁴.

All arguments above must be considered in light of the fact that in this manuscript we have only presented preliminary measurements for TOF-CT and TOF-PET with certainly not optimized samples. There are several paths to improve the performance and applicability. For instance, by a careful choice of the surface ligands and the embedding procedure, 60% filling factor for Cd(Zn)S/ZnS core-shell nanocrystals was reported while keeping the nanocomposite monolith transparent⁴². Moreover, the introduction of a wavelength-shifter to the matrix can be used to suppress the self-absorption, as successfully shown in the just mentioned study. Increasing the filling factor while enhancing the transparency automatically leads to a higher number of detected photons and thus an improvement in the timing capabilities. Another important question, in particular for TOF-PET and high energy physics detectors, is how to ensure high stopping power and sufficient energy deposition in the nanomaterials. One approach is to integrate it into a composite structure²⁷ with heavy inorganic scintillators like BGO⁴³ or GAGG:Ce,Mg^{41,44}.

5 Summary and Conclusion

In this work, we presented the fabrication and complete characterization of CsPbBr₃ nanocrystals with two different surface ligands (OA+OAm and DDAB) embedded in polystyrene with various particle filling factors, up to 10%. The characterization spanned from optical properties (transmission, PL, RL) to timing

properties under X-ray irradiation (scintillation decay kinetics and time resolution).

The optical characterization highlighted a drop in transmission with an increasing filling factor. These effects resulted less pronounced for CsPbBr₃ samples capped with DDAB which, compared to OA+OAm, is known to better passivate the surface of nanocrystals.

Decay time measurements in TCSPC revealed the presence of a (semi-)prompt component - modeled with a Dirac-delta function - contributing by 20% and three exponential decay components. The scintillation decay kinetics of CsPbBr₃ samples capped with DDAB were not affected by increasing concentration of nanoparticles, while for samples capped with OA+OAm an increase in the value of the slowest component itself and its weight was observed, at the expense of the fastest exponential component. Consequently, we can conclude that the DDAB ligand better prevents nanocrystals from aggregating.

Presented time resolution measurements confirm the applicability of this material to be used in radiation detector systems where fast timing is required. Already with non-optimized CsPbBr₃@PS a more than twofold better timing capability with respect to LYSO:Ce was achieved at low X-ray energy.

This study represents a promising starting point for the optimization of CsPbBr₃ nanocrystals embedded in polymer matrices toward their use in time-based radiation detector systems.

Author Contribution

Kateřina Děcká: Conceptualization, Formal analysis, Investigation, Validation, Visualization, Methodology, Writing- original draft, Writing - review & editing. **Fiammetta Pagano:** Conceptualization, Formal analysis, Investigation, Validation, Visualization, Methodology, Software, Writing- original draft, Writing - review & editing. **Isabel Frank:** Formal analysis, Investigation, Validation, Visualization, Writing - review & editing. **Nicolaus Kratochwil:** Methodology, Supervision, Writing- original draft, Writing - review & editing. **Eva Mihóková:** Funding, Resources, Project administration, Methodology, Supervision, Writing - review & editing. **Etiennette Auffray:** Conceptualization, Funding, Resources, Project administration, Supervision, Writing - review & editing. **Václav Čuba:** Conceptualization, Funding, Resources, Project administration, Supervision, Writing - review & editing.

Conflicts of interest

There are no conflicts of interest to declare.

Acknowledgment

This work was carried out in the frame of Crystal Clear Collaboration. This research was funded by the Czech Science Foundation, grant number GA20-06374S, Operational Programme Research, Development and Education financed by European Structural and Investment Funds and the Czech Ministry of Education, Youth and Sports (Project No. SOLID21 CZ.02.1.01/0.0/0.0/16_019/0000760) and by the Grant Agency of the Czech Technical University in Prague, grant number SGS20/185/OHK4/3T/14. Further support was provided from the CERN Budget for Knowledge Transfer to Medical Applica-

tions and from the European Union's Horizon 2020 Research and Innovation programme under Grant Agreement No 101004761 (AIDAInnova).

The authors express their gratitude to Jan Král for introducing the ligand exchange procedure.

Notes and references

- 1 L. Protesescu, S. Yakunin, M. I. Bodnarchuk, F. Krieg, R. Caputo, C. H. Hendon, R. X. Yang, A. Walsh and M. V. Kovalenko, *Nano letters*, 2015, **15**, 3692–3696.
- 2 J. Song, J. Li, X. Li, L. Xu, Y. Dong and H. Zeng, *Advanced materials*, 2015, **27**, 7162–7167.
- 3 Y. Wang, T. Zhang, M. Kan and Y. Zhao, *Journal of the American Chemical Society*, 2018, **140**, 12345–12348.
- 4 A. Swarnkar, R. Chulliyil, V. K. Ravi, M. Irfanullah, A. Chowdhury and A. Nag, *Angewandte Chemie*, 2015, **127**, 15644–15648.
- 5 Y. Zhang, R. Sun, X. Ou, K. Fu, Q. Chen, Y. Ding, L.-J. Xu, L. Liu, Y. Han, A. V. Malko *et al.*, *ACS nano*, 2019, **13**, 2520–2525.
- 6 M. Gandini, I. Villa, M. Beretta, C. Gotti, M. Imran, F. Carulli, E. Fantuzzi, M. Sassi, M. Zaffalon, C. Brofferio *et al.*, *Nature Nanotechnology*, 2020, **15**, 462–468.
- 7 V. Mykhaylyk, H. Kraus, V. Kapustianyk, H. Kim, P. Mercere, M. Rudko, P. Da Silva, O. Antonyak and M. Dendebera, *Scientific Reports*, 2020, **10**, 1–11.
- 8 O. D. Moseley, T. A. Doherty, R. Parmee, M. Anaya and S. D. Stranks, *Journal of Materials Chemistry C*, 2021, **9**, 11588–11604.
- 9 H. Yang, H. Li, R. Yuan, J. Chen, J. Zhao, S. Wang, Y. Liu, Q. Li and Z. Zhang, *Journal of Materials Chemistry C*, 2021, **9**, 7905–7909.
- 10 K. Tomanová, V. Čuba, M. G. Brik, E. Mihóková, R. Martínez Turtos, P. Lecoq, E. Auffray and M. Nikl, *APL Materials*, 2019, **7**, 011104.
- 11 A. Benaglia, S. Gundacker, P. Lecoq, M. Lucchini, A. Para, K. Pauwels and E. Auffray, *Nuclear Instruments and Methods in Physics Research Section A: Accelerators, Spectrometers, Detectors and Associated Equipment*, 2016, **830**, 30–35.
- 12 M. T. Lucchini, W. Chung, S. C. Eno, Y. Lai, L. Lucchini, M. Nguyen and C. G. Tully, *Journal of Instrumentation*, 2020, **15**, P11005.
- 13 D. R. Schaart, G. Schramm, J. Nuyts and S. Surti, *IEEE transactions on radiation and plasma medical sciences*, 2021, **5**, 598–618.
- 14 P. Lecoq, C. Morel, J. O. Prior, D. Visvikis, S. Gundacker, E. Auffray, P. Križan, R. M. Turtos, D. Thers, E. Charbon *et al.*, *Physics in Medicine & Biology*, 2020, **65**, 21RM01.
- 15 J. Rossignol, R. M. Turtos, S. Gundacker, D. Gaudreault, E. Auffray, P. Lecoq, Y. Bérubé-Lauzière and R. Fontaine, *Physics in Medicine & Biology*, 2020, **65**, 085013.
- 16 N. Kratochwil, S. Gundacker and E. Auffray, *Physics in Medicine & Biology*, 2021, **66**, 195001.
- 17 S. I. Omelkov, V. Nagirnyi, S. Gundacker, D. A. Spassky, E. Auf-

- fray, P. Lecoq and M. Kirm, *Journal of Luminescence*, 2018, **198**, 260–271.
- 18 S. Gundacker, R. Pots, A. Nepomnyashchikh, E. Radzhabov, R. Shendrik, S. Omelkov, M. Kirm, F. Acerbi, M. Capasso, G. Paternoster *et al.*, *Physics in Medicine & Biology*, 2021, **66**, 114002.
- 19 K. Tomanová, A. Suchá, E. Mihóková, L. Procházková, I. Jakubec, R. M. Turtos, S. Gundacker, E. Auffray and V. Čuba, *IEEE Transactions on Nuclear Science*, 2020, **67**, 933–938.
- 20 R. Turtos, S. Gundacker, S. Omelkov, E. Auffray and P. Lecoq, *Journal of Luminescence*, 2019, **215**, 116613.
- 21 S. Gundacker, R. M. Turtos, N. Kratochwil, R. H. Pots, M. Paganoni, P. Lecoq and E. Auffray, *Physics in Medicine & Biology*, 2020, **65**, 025001.
- 22 Z. Zhu, Q. Sun, Z. Zhang, J. Dai, G. Xing, S. Li, X. Huang and W. Huang, *Journal of Materials Chemistry C*, 2018, **6**, 10121–10137.
- 23 Z. Li, L. Kong, S. Huang and L. Li, *Angewandte Chemie*, 2017, **129**, 8246–8250.
- 24 C. Wang, H. Lin, Z. Zhang, Z. Qiu, H. Yang, Y. Cheng, J. Xu, X. Xiang, L. Zhang and Y. Wang, *Journal of the European Ceramic Society*, 2020, **40**, 2234–2238.
- 25 Y. Tong, Q. Wang, H. Yang, X. Liu, E. Mei, X. Liang, Z. Zhang and W. Xiang, *Photonics Research*, 2021, **9**, 2369–2380.
- 26 R. M. Turtos, S. Gundacker, E. Auffray and P. Lecoq, *Physics in Medicine & Biology*, 2019, **64**, 185018.
- 27 F. Pagano, N. Kratochwil, M. Salomoni, M. Pizzichemi, M. Paganoni and A. E., *under review in Physics in Medicine & Biology*, 2022.
- 28 G. Konstantinou, P. Lecoq, J. M. Benlloch and A. J. Gonzalez, *IEEE Transactions on Radiation and Plasma Medical Sciences*, 2021.
- 29 F. Maddalena, A. Xie, X. Y. Chin, R. Begum, M. E. Witkowski, M. Makowski, B. Mahler, W. Drozdowski, S. V. Springham, R. S. Rawat *et al.*, *The Journal of Physical Chemistry C*, 2021, **125**, 14082–14088.
- 30 *Eljen technology EJ232 datasheet*, <https://eljentechnology.com/products/plastic-scintillators/ej-232-ej-232q>, 2021.
- 31 S. Vinogradov, *Nuclear Instruments and Methods in Physics Research Section A: Accelerators, Spectrometers, Detectors and Associated Equipment*, 2018, **912**, 149–153.
- 32 F. Pagano, N. Kratochwil, M. Salomoni, I. Frank, S. Gundacker, M. Pizzichemi, M. Paganoni and A. E., *IEEE Nuclear Science Symposium and Medical Imaging Conferences (20th October)*, Yokohama, Japan (remote), 2021.
- 33 F. Pagano, N. Kratochwil, M. Salomoni, I. Frank, S. Gundacker, M. Pizzichemi, M. Paganoni and A. E., *under review in Frontiers in Physics*, 2022.
- 34 L. Zhang, W. Liang, L. Xu, M. Zhu, X. Wang, J. Su, L. Li, N. Liu, Z. Zhang and Y. Gao, *Chemical Engineering Journal*, 2021, **417**, 129349.
- 35 M. Imran, P. Ijaz, L. Goldoni, D. Maggioni, U. Petralanda, M. Prato, G. Almeida, I. Infante and L. Manna, *ACS Energy Letters*, 2019, **4**, 819–824.
- 36 L. Bollinger and G. E. Thomas, *Review of Scientific Instruments*, 1961, **32**, 1044–1050.
- 37 S. Gundacker, R. Turtos, E. Auffray and P. Lecoq, *Nuclear Instruments and Methods in Physics Research Section A: Accelerators, Spectrometers, Detectors and Associated Equipment*, 2018, **891**, 42–52.
- 38 N. Yarita, H. Tahara, T. Ihara, T. Kawawaki, R. Sato, M. Saruyama, T. Teranishi and Y. Kanemitsu, *The journal of physical chemistry letters*, 2017, **8**, 1413–1418.
- 39 M. N. Ashner, K. E. Shulenberger, F. Krieg, E. R. Powers, M. V. Kovalenko, M. G. Bawendi and W. A. Tisdale, *ACS Energy Letters*, 2019, **4**, 2639–2645.
- 40 R. Turtos, S. Gundacker, S. Omelkov, B. Mahler, A. Khan, J. Saaring, Z. Meng, A. Vasil'ev, C. Dujardin, M. Kirm *et al.*, *npj 2D Materials and Applications*, 2019, **3**, 1–10.
- 41 K. Děcká, J. Král, F. Hájek, P. Průša, V. Babin, E. Mihóková and V. Čuba, *Nanomaterials*, 2021, **12**, 14.
- 42 C. Liu, Z. Li, T. J. Hajagos, D. Kishpaugh, D. Y. Chen and Q. Pei, *ACS nano*, 2017, **11**, 6422–6430.
- 43 N. Kratochwil, E. Auffray and S. Gundacker, *IEEE Transactions on Radiation and Plasma Medical Sciences*, 2020, **5**, 619–629.
- 44 L. Martinazzoli, N. Kratochwil, S. Gundacker and E. Auffray, *Nuclear Instruments and Methods in Physics Research Section A: Accelerators, Spectrometers, Detectors and Associated Equipment*, 2021, **1000**, 165231.